A Thesis Submitted for the Degree of PhD at the University of Warwick

Permanent WRAP URL:

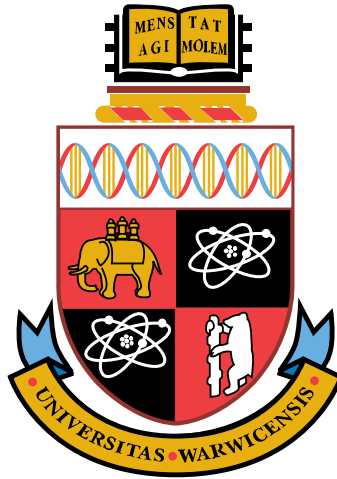http://wrap.warwick.ac.uk/160899

warwick.ac.uk/lib-publications

Atomic and Electronic Structure of Random and Ordered 2D Alloys

by

Xue Xia

Thesis

Submitted to the University of Warwick

for the degree of

Doctor of Philosophy

Department of Physics

September 2020

WARWICK

THE UNIVERSITY OF WARWICK

Table of Contents

List of Figures

Chapter 1

Chapter 2

Chapter 3

Chapter 4

Chapter 5

List of Tables

Chapter 2

Chapter 3

Chapter 4

Chapter 5

Acknowledgements

Lastly and most importantly, I want to thank my parents, my mother and father, for their endless encouragement and support. Without you, I could not get through all the darkness and setbacks that I was struggling with during my Ph.D. I love you all.

Declarations

I declare all data presented in this thesis is my own work except where stated. The research reported here has not been submitted and approved, either fully and in part, for the award of Doctor of Philosophy by this or any other institutions.

The XRD data in Chapter 3 and 4 was obtained with the assistance of Dr. David Walker. The XPS data in Chapter 4 was obtained with the assistance of Dr. Marc Walker. The Monte Carlo simulation and first principles calculations in Chapter 4 were performed by Miss Siow Mean Loh and Dr. Nicholas D. M. Hine. The μ-ARPES data in Chapter 4 and 5 was obtained and processed with the assistance of Miss Abi Graham, Prof. Neil Wilson, Dr. Viktor Kandyba and Dr. Alexei Barinov. The data of polarisation resolved PL spectra in Chapter 4 was obtained with the assistance Prof. David C. Smith. The LL-STEM-EELS data in Chapter 5 was obtained with assistance of Mr. Clive Downing and Prof. Ana Sanchez Fuentes. In these cases, the author was the dominant experimentalist. All the other data and interpretations have been carried out by the author.

Xue Xia

September 2020

Publications

2019

1. Hamer, M. J., Zultak, J., Tyurnina, A. V., Zólyomi, V., Terry, D., Barinov, A., Garner, A., Donoghue, J., Rooney, A. P., Kandyba, V., Giampietri, A., Graham, A., Teutsch, N., **Xia, X.**, Koperski, M., Haigh, S. J., Fal'ko, V. I., Gorbachev, R. V. & Wilson, N. R. Indirect to Direct Gap Crossover in Two-Dimensional InSe Revealed by Angle-Resolved Photoemission Spectroscopy. *ACS Nano* **13**, 2136–2142 (2019).

2. Nguyen, P. V., Teutsch, N. C., Wilson, N. P., Kahn, J., **Xia, X.**, Graham, A. J., Kandyba, V., Giampietri, A., Barinov, A., Constantinescu, G. C., Yeung, N., Hine, N. D. M., Xu, X. D., Cobden, D. H. & Wilson, N. R. Visualizing Electrostatic Gating Effects in Two-dimensional Heterostructures. *Nature* **572**, 220–223 (2019).

2020

3. Luo, Z. D., **Xia, X.**, Yang, M. M., Wilson, N. R., Gruverman, A. & Alexe, M. Artificial Optoelectronic Synapses Based on Ferroelectric Field-Effect Enabled 2D Transition Metal Dichalcogenide Memristive Transistors. *ACS Nano* **14**, 746–754 (2020).

4. Burdanova, M. G., Kashtiban, R. J., Zheng, Y., Xiang, R., Chiashi, S., Woolley, J. M., Woolley, J. M., Staniforth, M., Sakamoto-Rablah, E., **Xia, X.**, Broome, M., Sloan, J., Anisimov, A., Kauppinen, E. I., Maruyama, S. & Lloyd-Hughes, J. Ultrafast Optoelectronic Processes in 1d Radial van der Waals Heterostructures: Carbon, Boron Nitride, and MoS_2 Nanotubes with Coexisting Excitons and Highly Mobile Charges. *Nano Lett.* **20**, 3560–3567 (2020).

5. **Xia, X.**, Loh, S. M., Viner, J., Teutsch, N., Graham, A., Kandyba, V., Barinov, A., Sanchez, A., Smith, D., Hine, N. D. M. & Wilson, N. R. Atomic and Electronic Structure of Two-dimensional $Mo_{1-x}W_xS_2$ Alloys. *J. Phys. Mater.* (2021).

6. Loh, S. M., **Xia, X.**, Wilson, N. R. & Hine, N. D. M. Strong In-plane Anisotropy in the Electronic Properties of the Doped Transition Metal Dichalcogenide $W_{1-x}Nb_xS_2$. (2021). In preparation.

Abstract

Recently, transition metal dichalcogenides (TMDs) have attracted increasing research interest as promising two-dimensional materials for a range of electronic and optoelectronic applications and for the fundamental science that can be studied in them. This interest stretches beyond the properties of pure TMD materials, with an increasing number of reports on doped-TMD and TMD alloys to increase the functionality of these materials. For example, by substituting or alloying the metals or chalcogens of the TMDs, it is possible to tune their electronic structure.

In this thesis, single crystals of pure TMDs and of TMD alloys have been synthesised via chemical vapor transport (CVT). Techniques for the fabrication of van der Waals stacks with artificial sequences have been developed, specifically to allow the direct measurement of atomic and electronic structure in the alloys and to correlate these properties to optical spectroscopy measurements.

The atomic structure of $Mo_{1-x}W_xS_2$ alloys are visualised by annular dark field (ADF) scanning transmission electron microscopy (STEM). Statistical analysis of the images allows the atomic distributions to be compared to those from Monte Carlo simulations and first principles calculations. $Mo_{1-x}W_xS_2$ alloys show random distributions as expected from thermodynamic considerations. The evolution of the band structure of the $Mo_{1-x}W_xS_2$ alloys is determined by angle-resolved photoemission spectroscopy (ARPES) measurements and compared to first principles calculations. Combined, these results demonstrate that TMD alloying is a powerful approach for band structure engineering.

In contrast to the $Mo_{1-x}W_xS_2$ alloys, short-range ordering is found in $Nb_{0.1}W_{0.9}S_2$, with the Nb atoms forming atomic lines along one of the equivalent crystallographic directions. This ordering is confirmed by quantitative statistical analysis through the Warren-Cowley short-range order (SRO) parameters. Meanwhile, density function theory (DFT) calculations have been applied to explain this ordering, revealing this structure results from a combination of thermodynamic and kinetic considerations.

Abbreviations

2D – Two-Dimensional

ALD – Atomic Layer Deposition

ADF – Annular Dark Field

AFM – Atomic Force Microscopy

ARPES – Angle-Resolved Photoemission Spectroscopy

ARPRS – Angle-Resolved Polarised Raman Spectroscopy

BF – Bright Field

BTP – Back Focal Plane

BP – Black Phosphorous

BZ – Brillouin Zone

CB – Conduction Band

CBM – Conduction Band Minimum

CTEM – Conventional Transmission Electron Microscopy

CTF – Contrast Transfer Function

CVD – Chemical Vapor Deposition

CVT – Chemical Vapor Transport

DFT – Density Functional Theory

DI water – Deionised Water

EDX – Energy Dispersive X-ray Spectroscopy

EELS – Electron Energy Loss Spectroscopy

FE(T)T – Field-Effect (Tunneling) Transistor

hBN – Hexagonal Boron Nitride

HRTEM – High-Resolution TEM

IR – Infrared

IC – Integrated Circuit

IPA: Isopropyl Alcohol

KOH – Potassium Hydroxide

LL-EELS – Low-Loss Electron Energy Loss Spectrum

MIR – Mid-Infrared

NIR – Near Infrared

NGWFs – Non-Orthogonal Generalized Wannier Functions

PBE – Perdew, Burke and Ernzerhof

PL – Photoluminescence

PDMS – Polydimethylsiloxane

PMMA – Poly (Methyl Methacrylate)

PPC – Polypropylene Carbonate

PVA – Polyvinyl Alcohol

PVT – Physical Vapor Transport

PAW – Projector-Augmented Wave

STEM – Scanning Transmission Electron Microscopy

SAED – Selected Area Electron Diffraction

SRO – Short-Range Order

S/N – Signal-to-Noise

SiN – Silicon Nitride

SEM – Scanning Electron Microscopy

STS – Scanning Tunneling Spectroscopy

SOC – Spin-Orbit Coupling

THz – Terahertz

TMD(s) – Transition Metal Dichalcogenide(s)

TEM – Transmission Electron Microscopy

UHV – Ultrahigh Vacuum

UV – Ultraviolet

VB – Valence Band

VBM – Valence Band Maximum

VCA – Virtual Crystal Approximation

wt% – Weight Percentage

XPS – X-ray Photoelectron Spectroscopy

XRD – X-ray Diffraction

ZLP – Zero-Loss Peak

Chapter 1: Electronic Properties of TMDs and TMD Alloys

1.1 Two-dimensional (2D) materials and their heterostructures

The development of the semiconductor industry has followed Moore's Law: the number of transistors in a dense integrated circuit (IC) doubles roughly every two years[1]. As a result, the feature size of silicon transistors is approaching the quantum limit. This motivates the exploration and development of new alternative materials for electronics and optoelectronics[1,2]. The family of two-dimensional (2D) materials represents a promising candidate due to their physical scaling properties and their novel behaviours in the atomically thin regime[3–6].

The first report of the isolation and electrical characterisation of graphene was A. K. Geim and K. Novoselov in 2004 at University of Manchester[7]. Soon afterwards, they were awarded the Nobel prize in Physics in 2010 "for ground-breaking experiments regarding the 2D material graphene" [8]. Although it has been a decade since the discovery of graphene, this field is still young and in its early stages compared to traditional three-dimensional semiconductor electronics[9].

A typical 2D material is isolated from a 3D layered structure, where strong covalent bonds provide in-plane stability within each layer, while weak van der Waals force between adjacent layers keeps the layers together[5]. In principle, hundreds of materials fulfil these conditions. However, since the melting temperature decreases with reducing thickness of materials and most materials survive via forming naturally passivated surfaces under ambient condition[5,10], 2D materials with high thermal and chemical stability so that they can exist in atomically thin form are not so abundant.

In general, 2D materials cover three sub-groups within the 2D family: the graphene-like sub-group that includes graphene, hBN, BCN, fluorographene and graphene oxide *etc.*; the 2D chalcogenide-like sub-group such as MoS_2, WS_2, $MoSe_2$, WSe_2, ZrS_2, $NbSe_2$ and InSe *etc.*; and 2D oxides that involve micas, MoO_3, MnO_2, perovskite-type and

1

Graphene family	Graphene	hBN 'white graphene'		BCN	Fluorographene	Graphene oxide
2D chalcogenides	MoS_2, WS_2, $MoSe_2$, WSe_2	Semiconducting dichalcogenides: $MoTe_2$, WTe_2, ZrS_2, $ZrSe_2$ and so on		Metallic dichalcogenides: $NbSe_2$, NbS_2, TaS_2, TiS_2, $NiSe_2$ and so on		
				Layered semiconductors: GaSe, GaTe, InSe, Bi_2Se_3 and so on		
2D oxides	Micas, BSCCO	MoO_3, WO_3	Perovskite-type: $LaNb_2O_7$, $(Ca,Sr)_2Nb_3O_{10}$, $Bi_4Ti_3O_{12}$, $Ca_2Ta_2TiO_{10}$ and so on		Hydroxides: $Ni(OH)_2$, $Eu(OH)_2$ and so on	
	Layered Cu oxides	TiO_2, MnO_2, V_2O_5, TaO_3, RuO_2 and so on			Others	

Figure 1.1. The two-dimensional (2D) library. Monolayers proved to be stable under ambient conditions are in blue colour, those properly stable in air are in green, the materials in pink are unstable in air but properly stable in inert atmosphere, and the grey colour are material compounds that could be cleaved to monolayers. Adapted from Ref. 5.

hydroxides[5,11]. This includes a diverse range of electronic properties, from insulators such as hBN, semiconductors like MoS_2 and WS_2 *etc.*, semimetals including $MoTe_2$ and WTe_2 *etc.*, metals like VSe_2, and superconductors such as NbS_2 and $NbSe_2$ *etc.*[5,11]

These materials in their monolayer form have novel properties and show promise for electronic and optoelectronic applications. But this is over-shadowed by the potential for fabricating artificial stacks at the atomic scale by combining this extensive library of 2D materials to form heterostructures with selectable material properties, opening up the possibility to create novel hybrid structures that display new physics and enable unique functionality[5,6,12].

There are many reports using van der Waals stacks in devices to engineer improved optoelectronic performance. For example, field-effect tunnelling transistors (FETTs) with a tunnelling junction formed by graphene combined with semiconductor and insulator 2D crystals can achieve a high on-off ratio of 10^6 for WS_2[13] and 10^3 to 10^4 for MoS_2[14] as the semiconductors. Another example is simple and efficient phototransistors that are composed of a combination of graphene and transition metal dichalcogenides (TMDs) as a channel material. These TMDs are light-sensitive materials such that charge can be generated and controlled via illumination[5,6]. When the light sensitive materials are replaced by TMD heterostructures that stack different single layer TMDs (*e.g.* MoS_2/WSe_2) with different work functions, this can lead to photoexcited electron and

holes accumulating in different layers, so giving rise to indirect excitons[6,15]. Moreover, more complicated heterostructures composed of p- and n-doped TMDs can form an atomically sharp p-n junction, combining for example GaTe and MoS_2[6,16,17]. This kind of device is extremely efficient in carrier separation, demonstrating very high quantum efficiency[16]. All of these can be made by simply stacking 2D layers of different materials.

To fulfil this potential and to explore the possible combinations of 2D materials, there has been rapid development in the techniques required for the fabrication of van der Waals solids with artificial sequences[18]. The approaches can be divided into two broad categories: synthesis and transfer. Synthesis most commonly involves chemical vapor deposition (CVD)[11,19] or physical vapor deposition[11,19], while many techniques have been developed for transfer of the layers as will be discussed in detail in Chapter 3.

1.2 Transition metal dichalcogenides (TMDs)

Among all these 2D materials, the TMDs are one of the most significant sets of building blocks for artificial van der Waals stacks[11,12,20,21]. TMDs have unique layer-dependent properties, such as direct bandgaps in monolayer form that lead to strong photoluminescence (PL) emission and potential applications in optoelectronics such as photovoltaics and solar cells *etc.*[21] Therefore, the TMD family has attracted increasing

Figure 1.2. Layered transition metal dichalcogenides (TMDs) MX_2 indicated on a periodic table. The transition metals (M) are highlighted, while the chalcogen atoms (X) are in orange. The partially highlighted metals indicate those for which only some of the dichalcogenides from a layered structure. Adapted from Ref. 21.

attention and there is an explosive increase in the number of publications on these materials[20,21].

The TMDs are also a big family with up to 40 different categories, covering a wide range of electronic properties from insulating to semiconducting to superconducting[21,22]. Their chemical formula is MX_2, in which M is a transition metal atom and X a chalcogen atom[21]. As shown in Figure 1.2, the highlighted group 4-7 transition metals can combine with the orange-highlighted chalcogens to form MX_2, while for the metals with partial highlighting only some of them form MX_2[21]. Unlike single-atom-thick graphene, the MX_2 layers are composed of a layer of transition metal atoms sandwiched between two layers of chalcogen atoms, as shown in Figure 1.3[21–23].

The most extensively studied TMD materials, for their novel optical and electronic properties, are the MoWSeS group of MX_2 where M represents Mo and W, while X is S and Se.

1.2.1 Crystal structure of MoWSeS MX$_2$

In the bulk form, TMD layers are held together by weak van der Waals force that enable exfoliation[23]. The TMDs are usually found in three polytypes 1T (trigonal), 2H (hexagonal) and 3R (rhombohedral) as shown schematically in Figure 1.4[23]. For the most common 2H polytype/stacking, they have a unit cell of a bilayer with space group
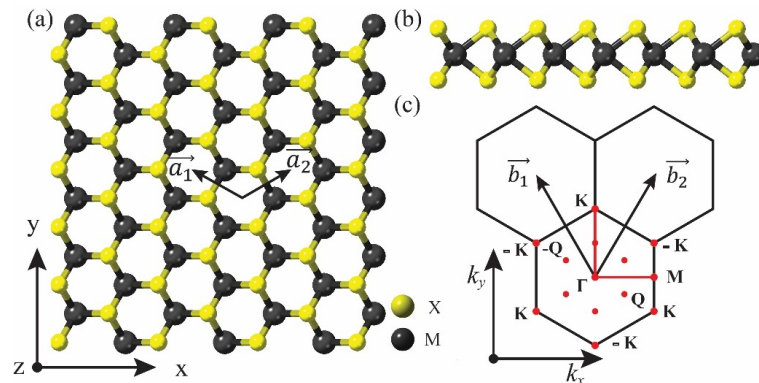
Figure 1.3. Crystal and reciprocal lattice of MX_2 monolayers. (a) Honeycomb lattice structure of MX_2 monolayer. (b) Side view of MX_2 monolayer. (c) The reciprocal lattice with Brillouin zones (BZ) and high-symmetry points marked, adapted from Ref. 26.

P6₃/mmc (in Figure 1.4b) and restored inversion symmetry[11,23]. The lattice parameters within the layers of the TMD are $a = b = 3.16$ Å, varying slightly for each of the MoWSeS group, and it is normally made of three stacked layers X-M-X as shown in Figure 1.3b[11]. For 3R polytype/stacking, they have a unit cell of a trilayer with space group *R3m* (in Figure 1.4b) and broken inversion symmetry[11]. These different stack sequences in bulk crystals can give different properties *e.g.* band structures and Raman shifts[11,24,25].

The monolayer structure can be described in 2D. The primitive lattice vectors, $\boldsymbol{a_1}$ and $\boldsymbol{a_2}$, of the real-space 2D MX₂ lattice are shown in Figure 1.3a[11] and given by[26]:

$$\boldsymbol{a_1} = \frac{a}{2}(\sqrt{3}\hat{\boldsymbol{x}} + \hat{\boldsymbol{y}}), \ \boldsymbol{a_2} = \frac{a}{2}(-\sqrt{3}\hat{\boldsymbol{x}} + \hat{\boldsymbol{y}}). \tag{1.1}$$

The reciprocal lattice vectors, $\boldsymbol{b_1}$ and $\boldsymbol{b_2}$ in Figure 1.3c, are given by[11,26],

$$\boldsymbol{b_1} = \frac{2\pi}{3a}(\frac{\sqrt{3}}{3}\widehat{\boldsymbol{k_x}} + \widehat{\boldsymbol{k_y}}), \ \boldsymbol{b_2} = \frac{2\pi}{3a}(-\frac{\sqrt{3}}{3}\widehat{\boldsymbol{k_x}} + \widehat{\boldsymbol{k_y}}). \tag{1.2}$$

The first Brillouin zone (BZ), defined as the Wigner-Seitz cell in reciprocal space, of a 2D layer of MX₂ is shown in Figure 1.3c[26,27] with high-symmetry points labelled. These groups of wave vectors are important since the invariance of the Hamiltonian under symmetry operations can lead to degeneracies at these high-symmetry points or directions in the BZ[11,26]. The **K** points are the corners of the hexagonal BZ, and they can be divided into **K** and **-K** due to lack of inversion symmetry in the real lattice of TMD crystals[11,22,26].
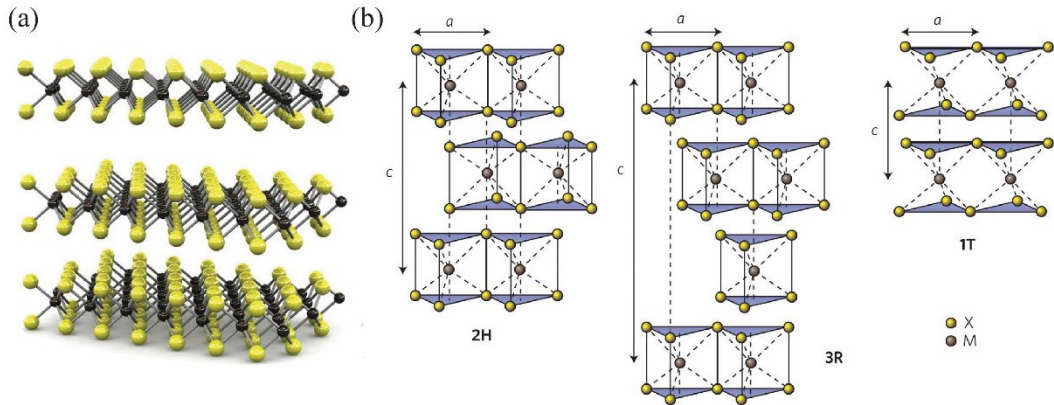
Figure 1.4. Atomic structure of TMD crystals. (a) Schematics of a few layer MX₂. (b) Schematics of 2H, 3R and 1T MX₂ polytypes. Adapted from Ref. 23.

Meanwhile the **M** point is at half of a reciprocal basis vector as shown in Figure 1.3c[11,22,26].

1.2.2 Electronic (band) structure of TMDs

1.2.2.1 Indirect-to-direct gap transitions

The weak interactions between layers are still significant enough to cause important changes in electronic structure with thickness. For the 2H polytypes of the MoWSeS group, the signature is a change from being indirect band gap semiconductors in bulk or multilayer materials, to being direct gap semiconductors in their monolayer form, fundamentally altering their optical response[23,28,29]. These changes are captured by first
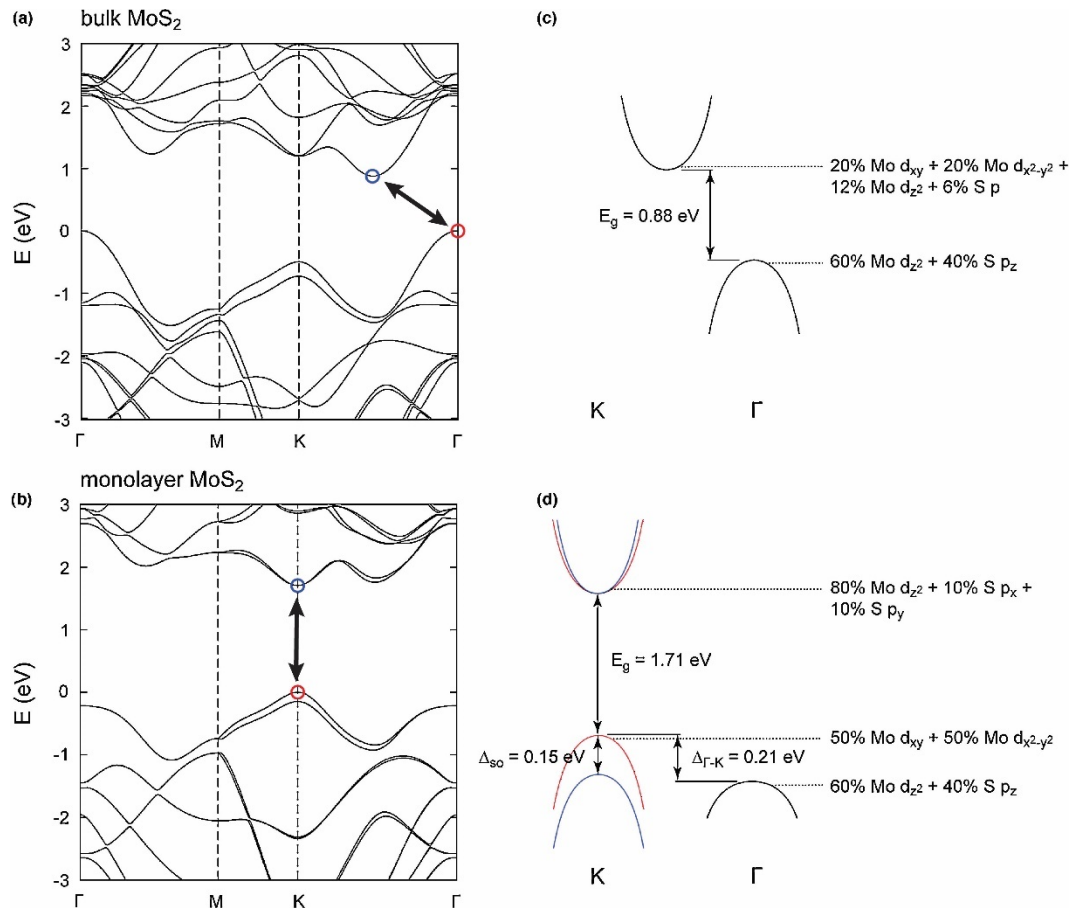
Figure 1.5. Band structure of bulk and monolayer MoS_2 via density function theory (DFT) calculations. (a) Band structure of bulk 2H-MoS_2. (b) Band structure of monolayer MoS_2. (c) and (d) Schematic drawings of low energy bands in bulk and monolayer MoS_2, respectively. Adapted from Ref. 28.

6

principles calculations, as shown in Figure 1.5. For bulk materials, the conduction band minimum (CBM) is located at a point **Q** along **Γ** to **K** and the valence band maximum (VBM) at **Γ** (see Figure 1.3c for the position of these high-symmetry points). For monolayers, both the CBM and VBM are located at high symmetry valley points $\pm$**K** (the corners of the first BZ).

The bandgap narrows from monolayer to bulk, showing that the change in band position is due to the interactions between layers that result in dispersion in k_z for some of the bands. For MoS$_2$, at the valence band (VB) edge at the **K** point the states are primarily composed of d_{xy} and $d_{x^2-y^2}$ orbitals of the metal hybridized with p_x and p_y orbitals of the chalcogen atoms[22,28]. These are all oriented within the plane of the layer, as a result they have almost no k_z dispersion and so do not change with thickness.
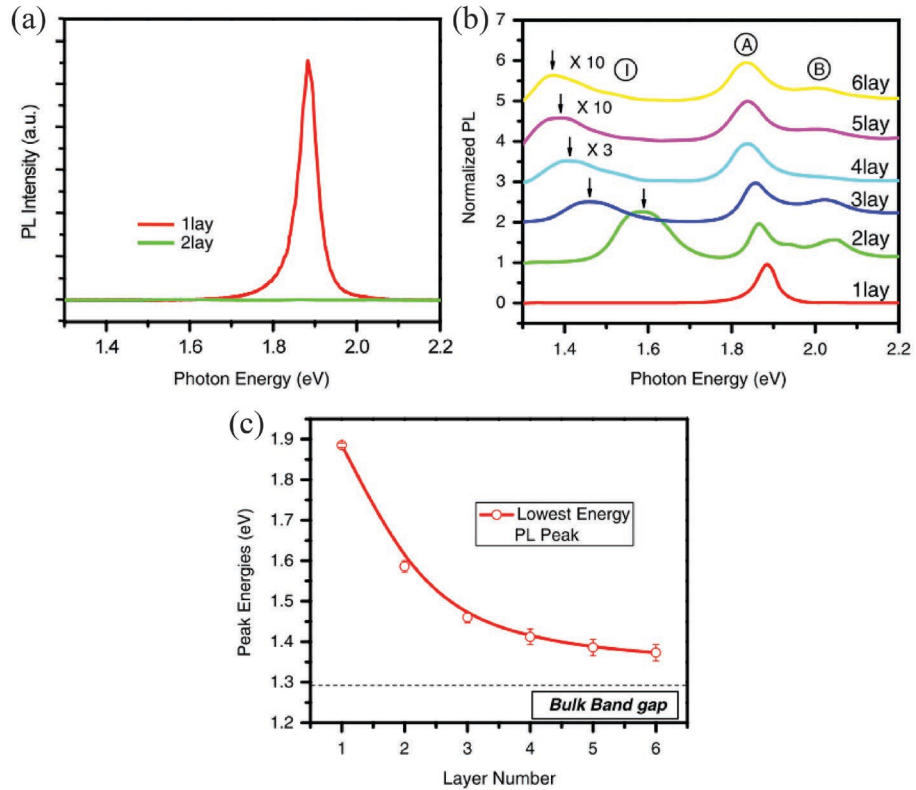
Figure 1.6. Photoluminescence (PL) spectra of MoS$_2$ samples with different thickness. (a) PL spectra for mono- and bilayer MoS$_2$ flakes. (b) PL spectra, normalised by the intensity of peak A, of thin layers of MoS$_2$ for layer number N = 1 to 6. (c) Optical gap energy as a function of layer number, the dashed line represents the band gap energy of bulk MoS$_2$. Adapted from Ref. 29.

7

Similarly, the main contribution to the conduction band (CB) edge at **K** is from the $d_{3z^2-r^2}$ orbital of the metal with minor contributions from p_x and p_y orbitals of the chalcogens[22,28]. Again, these orbitals are localised in the xy plane and are not affected by the distance between layers along the z axis[22,28]. By contrast, the states at the VB edge at the **Γ** point originate from a linear combination of p_z orbitals of S atoms and d_{z^2} orbitals of Mo atoms, they are rather delocalised and have an antibonding nature[22,28]. They are oriented perpendicular to the layers and when the interlayer distance increases the interaction between layers decreases, leading to a lowering in energy of these antibonding states[11,22,28]. Therefore, the strong k_z dispersion of the states at **Γ** result in a strong layer dependence to their VB edge, resulting in an increase in band gap as the thickness is decreased and eventually the indirect to direct band gap transition in the monolayer limit.

The first experimental evidence for the validity of these first principles calculations came from PL measurements[29,30]. PL emission from monolayer MoS_2 shows a strong peak at around 1.9 eV which corresponds to its optical gap[29], Figure 1.6. As the thickness of MoS_2 increases to 2 layers, the intensity of the PL peak drastically decreases by more than an order of magnitude as shown in Figure 1.6a which can be attributed to the indirect-to-direct band transition[29,30]. Moreover, the peak redshifts and broadens, approaching the indirect optical gap of 1.29 eV as the layer number increases, as shown in Figures 1.6b and 1.6c[29]. Qualitatively similar results are obtained from both the first principles calculations and PL measurements of the other materials $MoSe_2$, WS_2 and WSe_2[31,32].

1.2.2.2 Optical and electronic gap

The band gaps of $1H-MX_2$ monolayers can be measured by transport or optical methods, however, they give different results because of the excitonic effects in optical processes[11,22]. The electronic band gap is defined as the sum of the energy required to tunnel an electron and a hole into the system, separately[33,34]. The optical band gap is the energy to create an exciton: during the optical excitation process the absorption of a photon creates an electron in the CB and a hole in the VB which combine to form an exciton due to the Coulomb interaction[22,23]. The exciton binding energy decreases the optical gap relative to the electronic gap, and in monolayer TMD it can be large, up to several hundred meV.

The optical band gaps can be determined by PL measurements, as shown in Figure 1.6, while the electronic band gaps can be revealed by scanning tunneling spectroscopy (STS)[33,34] or angle-resolved photoemission spectroscopy (ARPES) as shown in Figure 2.17[35]. First-principles calculations are also widely applied to determine the band gaps and the excitonic effects in monolayers, as shown in Figure 1.5b. The exciton binding energy can be obtained from the difference between the electronic and optical band gaps[22].

1.2.2.3 Spin-orbit coupling (SOC) splitting

Spin-orbit coupling (SOC) arises from the interaction between the magnetic moments of the electron spin and the orbital momentum of the shell electrons of atoms[36,37]. The SOC is significant in TMD and plays an important role in determining the optoelectronic properties of these materials. Including SOC in density functional theory (DFT) calculations of MX_2 monolayers, a sizable spin splitting is found in their electronic band structures, as shown in Figure 1.7[38].

The spin splitting at the **K** valley of the VBM caused by SOC and inversion symmetry breaking can be fully determined by symmetry analysis[22]. The first restriction is mirror symmetry: under the mirror reflection operation about the metal plane, the in-plane spin vector is its opposite, while the out-of-plane spin vector remains the same. Therefore the spin splitting has to be along the z direction (out-of-plane)[22]. Due to time reversal symmetry, the spin splitting at an arbitrary pair of momentum space points **K** and **–K** must have identical magnitude but opposite sign[22]. Inversion symmetry conflicts with the time reversal symmetry such that inversion symmetry breaking is a necessary condition for band splitting[22].

The two excitonic absorption peaks observed in Figure 1.6b, labelled as A and B, originate from the SOC splitting of the direct gap transition at the **K** point, as indicated by the arrows in Figure 1.7c. The energy difference between the A and B peaks is related to the strength of the SOC: it is stronger in WX_2 (around 400 meV)[32,39] than MoX_2 (around 160 meV)[39,40]. This is also consistent with first principles calculations as shown
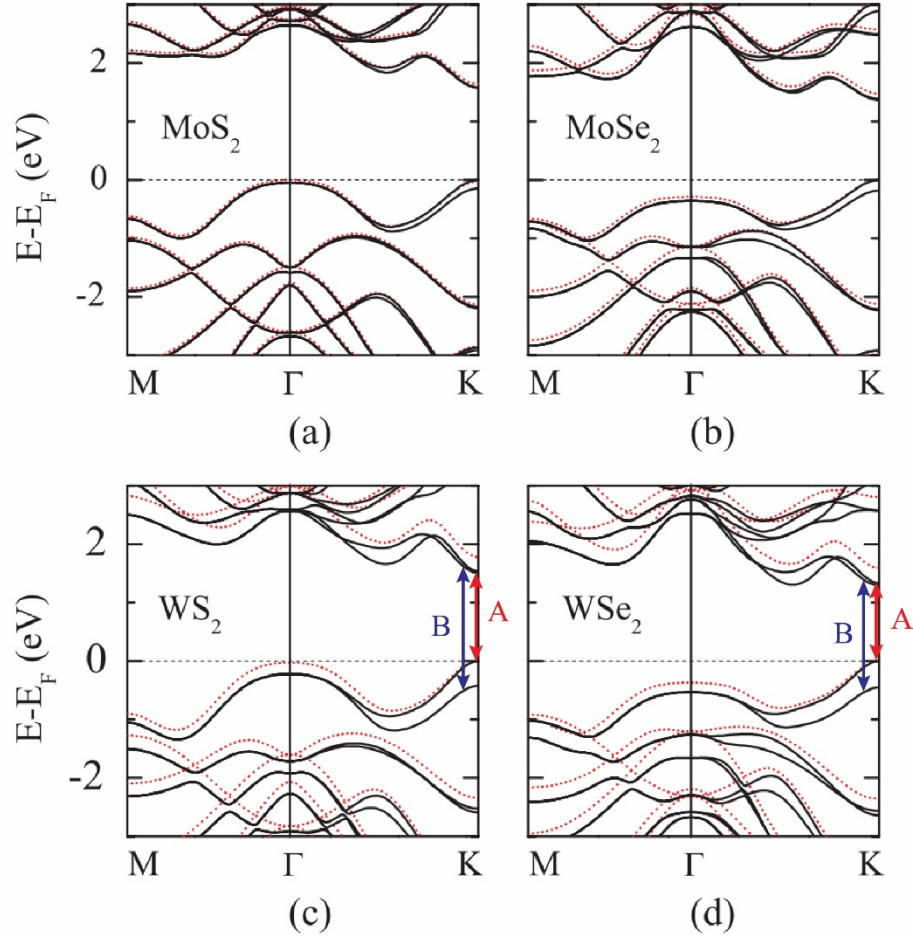
Figure 1.7. Electronic band structures for the MX_2 monolayers. Electronic band structures calculated for (a) MoS_2, (b) $MoSe_2$, (c) WS_2 and (d) WSe_2 monolayers, with SOC in solid lines and without SOC in dotted lines, respectively. Adapted from Ref. 38.

in Figure 1.7[38]. Note that the SOC splitting at **K** cannot be directly determined from the optical measurements: equating the difference between the A and B exciton peaks to the magnitude of the SOC splitting makes several assumptions, such as that the exciton binding energies of the A and B excitons are the same.

1.2.2.4 Spin-valley locking

As a result of the giant SOC, the VBM in monolayer TMDs has the spin index locked with the valley index. For example, valley **K** (-**K**) has only the spin up (down) holes as shown schematically in Figure 1.8a[41]. Another consequence of the SOC is that the valley-dependent selection rules also become spin dependent[22,42,43]. This selection rule gives the possibility of quantum control of the valley pseudospin through *e.g.* optical generation
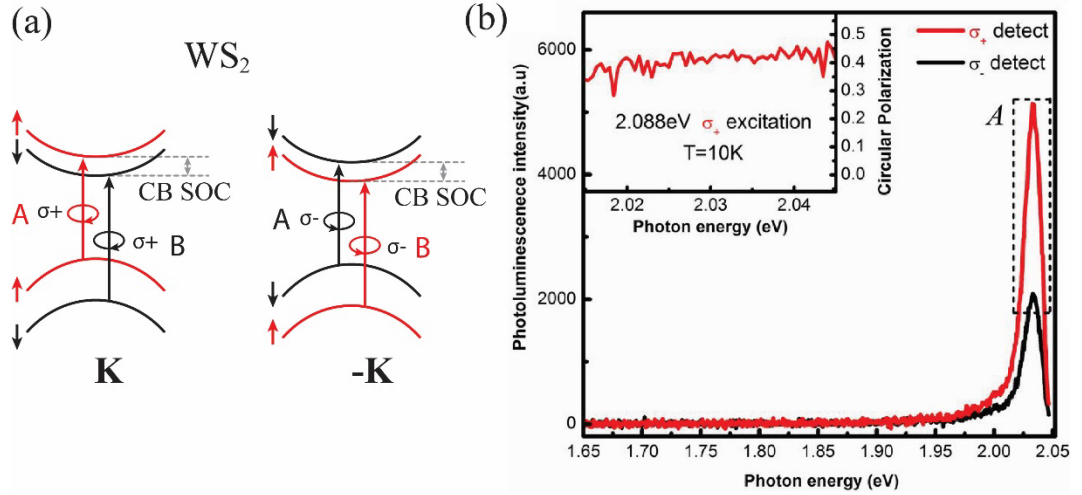
Figure 1.8. Optical selection rule. (a) Schematic diagram of the band structure at the band edges located at the $\pm\mathbf{K}$ points. (b) Polarization resolved PL spectra of monolayer WS_2 under $\sigma +$ (right hand circularly polarized) excitation at 10 K, adapted from Ref. 41.

and detection of valley polarization and valley coherence[41,43]. For example, valley polarization can be achieved by the polarization of the optical excitation, carried out experimentally by polarization resolved PL measurements[41].

Figure 1.8b shows PL spectra from monolayer WS_2 at 10 K[41]. The PL is dominated by the emission from the band-edge excitons (A exciton) at $\mathbf{K}$ and $-\mathbf{K}$ valleys[41]. The excitons carry a clear circular dichroism under near resonant excitation with circular polarization, confirming the valley-selective optical selection rules: the right-hand ($\sigma +$) polarization corresponds to the interband optical transition at $\mathbf{K}$ valley[41,44]. The degree of circular polarization can be defined as[41,44]

$$P = \frac{I(\sigma+)-I(\sigma-)}{I(\sigma+)+I(\sigma-)},$$

1. 3

in which $I(\sigma +)$ is the intensity of the right-handed circular polarization component, while $I(\sigma -)$ is the intensity of the left-handed circular polarization[41]. Under $\sigma +$ excitation, the degree of circular polarization is found to be $P = 0.4$[41].

1.2.3 Applications

As described above, TMDs exhibit unique electrical and optical properties making them promising candidate for a variety of optoelectronic applications such as solar cells[45], photodetectors[46], light-emitting diodes[17] and phototransistors[47].

For phototransistors, photons of energy greater than the band gap incident on a semiconductor create bound electron-hole pairs (excitons) or free carriers depending on the exciton binding energy in the semiconductor[11]. The bound excitons are separated by an applied or built-in electric field, generating a photocurrent[11]. A typical TMD-based photodiode is show in Figure 1.9a. When a laser with 514 nm excitation illuminates the MoS_2, a highly distinct photo-response can be observed under different gate voltages in scanning photocurrent mapping, as shown in Figure 1.9b[48]. By varying the thickness of the MoS_2 layer, as the band gap changes the detection range of the phototransistor can be tuned to absorb light of different wavelengths from ultraviolet (UV) to infra-red[49].

In general, there are three basic types of van der Waals heterostructures that have been explored as unique platforms for creating tunable photodetectors[6,11,49]. The first type has been shown in Figure 1.9. Figure 1.10b shows a device constructed from a p-n diode composed of a p-type and an n-type TMD flake. This kind of detector can achieve dynamic modulation of the diode characteristics, e.g. photoresponsivity and gain, since
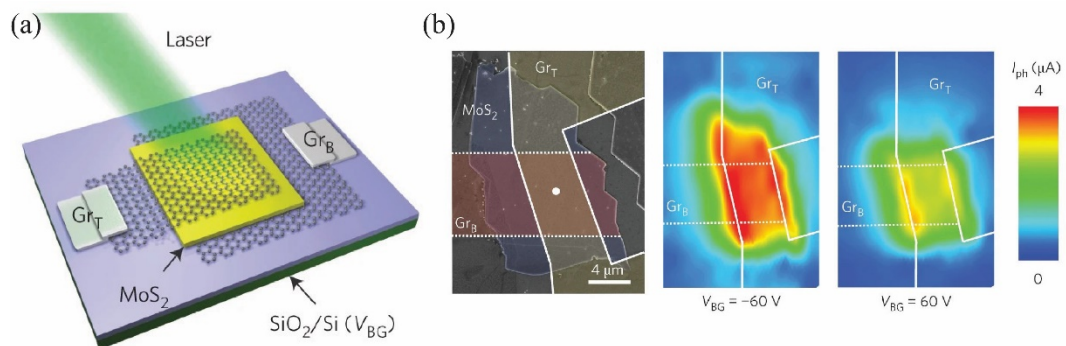
Figure 1.9. MoS_2-based van der Waals heterostructure optoelectronics. (a) Schematic diagram of the van der Waals vertical photodiode structure. (b) Colored scanning electron microscope image (left); scanning photocurrent images at gate voltage of -60 V (middle) and +60 V (right) under 514 nm laser excitation. Adapted from Ref. 48.

the majority carrier density can be tuned by applying external gate electric fields[12,17,50]. However, the carrier mobility of these devices is low while the series resistance for the charge transfer in the lateral channels is high, hence the high diffusion time of the majority carriers limits the responsivity and detection speed[12,17]. To avoid these limitations, graphene can be introduced as the electrodes, as shown in Figure 1.10c[12,50]. The generated carriers can be collected via direct vertical charge transfer instead of lateral diffusion. As a result, the interlayer recombination losses are reduced, leading to significantly increased charge collection efficiency[12].

According to the energy of photons detected, photodetectors can be divided into different categories, such as X-ray, UV, visible and infrared (IR), and terahertz (THz) detectors[49]. Since the band gaps of the TMDs range from less than 1 eV to above 2.5 eV, the corresponding TMD-based photodetectors can cover visible and near infrared (NIR) of the electromagnetic spectrum as shown in Figure 1.10d[49]. As this figure shows, 2D materials continuously cover a large range of the spectrum, including for example an alloy of black phosphorous (BP), $P_{1-x}As_x$, whose band gap is tunable through the mid-infrared (MIR) in the range 0.15 - 0.3 eV[51,52]. Moreover, p-n junctions can be formed in these devices by alloying or doping of the constituent layers. For example, $MoSe_2$ is
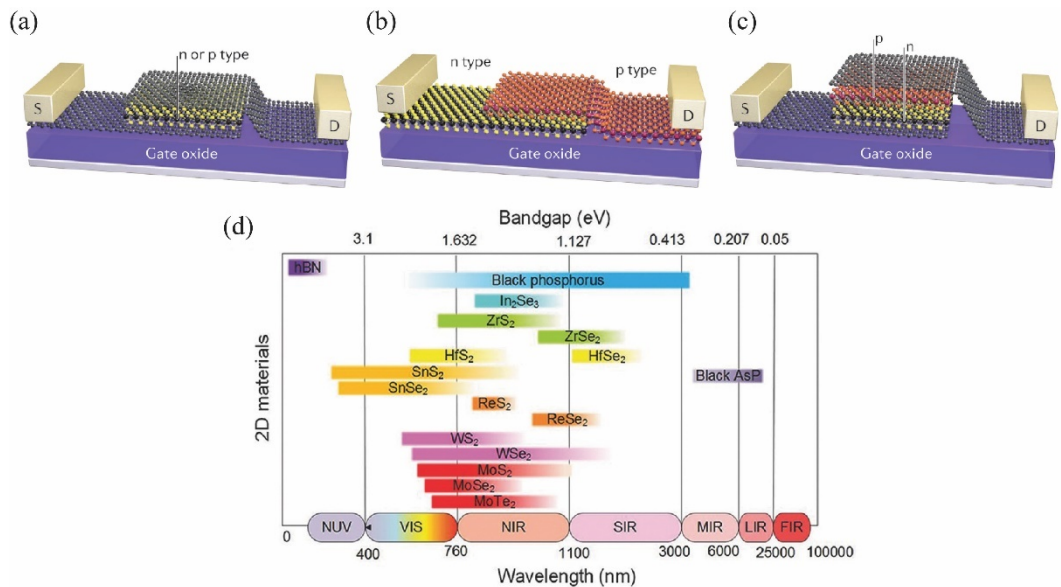
Figure 1.10. Van der Waals heterostructure optoelectronics. (a-c) Schematic diagrams of van der Waals vertical photodiode structures. Adapted from Ref. 12. (d) Band gap values of different 2D materials and their corresponding detection range. Adapted from Ref. 49.

usually a naturally n-type material but it can be p-type doped by the addition of Nb; stacking a layer of n-doped material onto a layer of p-doped material is a simple way of forming a vertical p-n junction with large interfacial area[53]. Therefore, alloying TMDs can make significant contributions to the abundance of useful building blocks for 2D optoelectronic devices[49].

1.3 TMD alloys

Ternary TMD alloys can be made through either addition of an extra type of metal atom to MX_2, or an extra type of chalcogen atom[11]. Creation of semiconductor alloys is an efficient way for the band gap and even spin-orbit engineering of bulk and thin materials, to be tuned for applications in specific optoelectronic devices[39]. As a result, there are many reports of 2D-TMD alloys with tunable band gaps and optical properties[40,54–58].

1.3.1 Synthesis of TMD alloys

There are two approaches that are widely used in nanomaterials fabrication: top-down and bottom-up techniques[11]. For synthesis of 2D TMDs, the top-down methods are to cleave bulk crystals into multi-layers or mono-layers by, for example, mechanical exfoliation, liquid exfoliation or electrochemical exfoliation *etc*. Bottom-up approaches include growth methods such as CVD, physical vapour transport and atomic layer deposition (ALD)[11].

Although there are many techniques introduced above for pure materials synthesis, among these there are only a few methods that can be used for fabricating TMD alloys[11]. CVD and chemical vapor transport (CVT) are the most widely used[11,19].

1.3.1.1 Chemical vapor deposition (CVD)

Many different setups have been reported for the CVD method, but Figure 1.11 shows a typical system[11,55,58–60]. The chalcogen (X = S and Se) powders are vaporised by heating
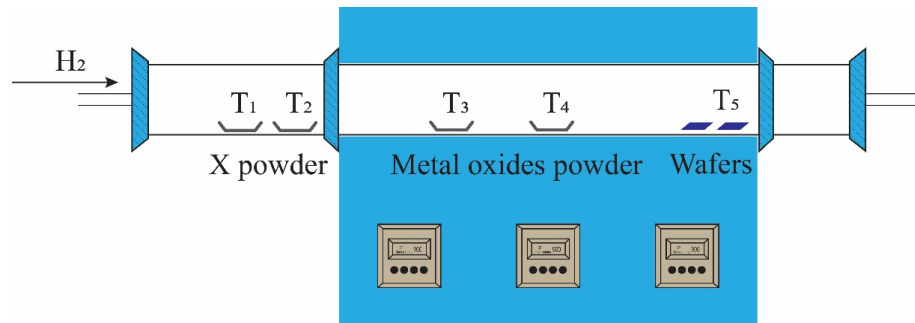
Figure 1.12. Schematic of a typical setup for chemical vapor deposition (CVD). Chalcogen (X = S, Se and Te) and transition metal (M = Mo, W and Nb *etc.*) powder are placed at left side and centre of the furnace, while the substrates (*e.g.* SiO_2/Si and sapphire) are located downstream.

to high temperature, T_1 and T_2[11,58]. Metal oxide powders are heated to T_3 and T_4 (higher temperature) for vaporisation[55,59]. The carrier gas (H_2) reacts with the chalcogen and with the metal oxide vapor, transporting them through the tube furnace. At the downstream end of the furnace, alloy flakes (*e.g.* $Mo_{1-x}W_xX_2$, $MoS_{2-2x}Se_{2x}$ and $WS_{2-2x}Se_{2x}$) are formed via chemical reaction and deposited onto substrates. Normally this method produces
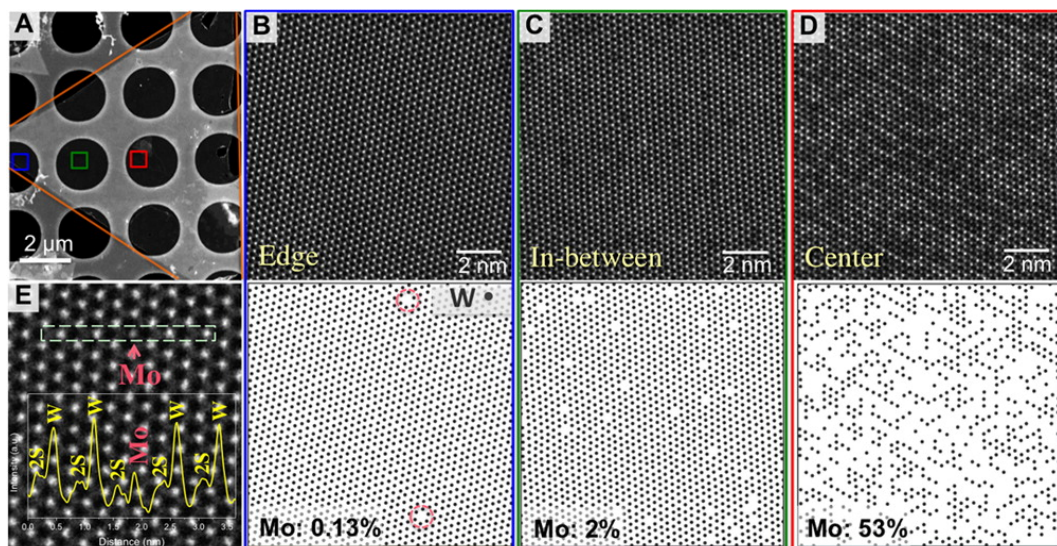
Figure 1.11. Atomic resolution scanning transmission electron microscopy (STEM) images of different regions on the same monolayer $Mo_{1-x}W_xS_2$ flake via CVD. (a) Dark field STEM image of a single layer $Mo_{1-x}W_xS_2$ on a TEM grid. ADF-STEM images of monolayer alloy $Mo_{1-x}W_xS_2$ from regions marked via (b) blue, (c) green and (c) red squares. The lower panels show distribution of W atoms in corresponding STEM images. (e) Intensity profile along the box with dash line. Adapted from Ref. 60.

triangular or hexagonal monolayer or bilayer alloy flakes with lateral dimensions of up to several tens of micrometers[55,58,59].

A typical alloy $Mo_{1-x}W_xS_2$ synthesized by CVD, using a similar system to that described above, is shown in Figure 1.12[55,60]. The atomic structure is visualised by annular dark field (ADF) scanning transmission electron microscopy (STEM) images. The atomic concentrations are different at the edge compared to the centre of the alloy flake[60]. This inhomogeneous distribution of W atoms leads to inhomogeneous properties of the same flake, for example the optical band gaps measured by PL emission depend on the composition of the alloy and so vary across the flake[55,60]. Therefore, visualisation of the atomic structure is essential for understanding the properties of these alloys.

1.3.2.1 Chemical vapor transport (CVT)

CVT is used to grow single crystals rather than isolated monolayers. For monolayers it has the key advantage that the powder precursors can be made stoichiometrically correct before the CVT process. In this way, unlike for CVD, the TMD compounds are already formed before the vapor transport process and as a result the distribution of alloy elements in the synthesised crystals is more homogeneous. A typical setup is shown in Figure 1.13[61]. The source materials and transport agent (CCl_4, Cl_2, Br_2 or I_2 crystals) are mixed
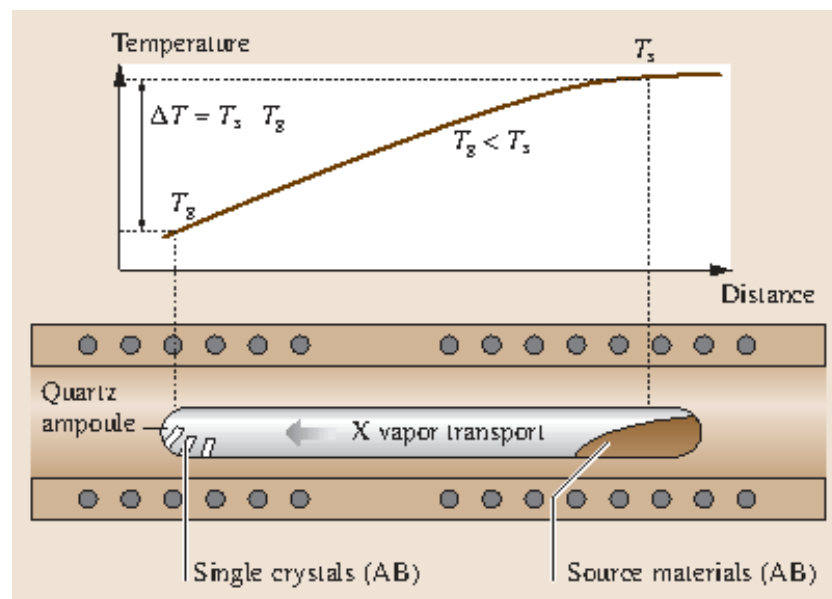
Figure 1.13. Schematic diagram of a typical setup of chemical vapor transport (CVT). Adapted from Ref. 61.

and placed at the end of an evacuated ampoule at the source zone of the tube furnace. The source and growth zone are heated to temperatures T_s and T_g, respectively (T_s>T_g)[61–63]. The compounds sublime and react with the transport agent in the source zone. The vapor phases diffuse down the ampoule towards the growth end, depositing on the cooler wall of the quartz ampoule at the growth end to nucleate and grow alloy crystals[61–63].

1.3.2 Tuning the electronic structures of 2D TMDs by alloying

There are many parameters for the electronic band structure of a TMD that can be tuned by alloying. However, the most important for optoelectronic devices are the band gap[56–58,64] and SOC[39].

1.3.2.1. Band gap engineering

PL emission from WS_2Se_{2-2x} monolayers can be tuned continuously from 626.6 nm (pure WS_2) to 751.9 nm (pure WSe_2) by changing the composition as shown in Figure 1.14a[64]. Plotting the band gap against the S concentration, Figure 1.14b, shows a linear relationship[64]. Similar results have been observed in other ternary alloys *e.g.* $Mo_{1-x}W_xS_2$, and $Mo_{1-x}W_xSe_2$ *etc.*[56,57]. However, the evolution of PL emission peaks against the alloy compositions are not linear for the various alloys, with different bowing factors found for each[56,57]. The fact that the band gaps can be continuously tuned over a large range, with high optical quality material, makes alloying a very promising technique for optimising 2D semiconductor devices to specific applications.
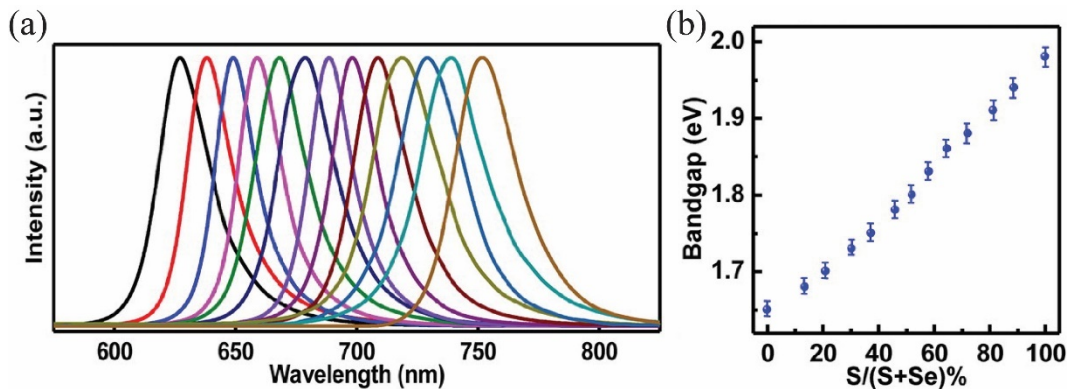
Figure 1.14. Evolution of PL emission peaks as a function of S compositions in $WS_{2x}Se_{2-2x}$ monolayers. (a) PL emission peaks as a function of S compositions. (b) Plot of band gaps against S/(S+Se) ratio. Adapted from Ref. 64.

1.3.2.2 Spin-orbit engineering

The large SOC at the VBM of the monolayer TMDs at **K** leads to important properties such as spin-valley locking, as discussed previously. As a result, there is interest in controlling the magnitude of SOC through alloying. The ternary $Mo_{1-x}W_xSe_2$ alloy is an interesting example. The sign of the spin-splitting in the CB depends on the transition metal, the order of the spin polarised states in the **K** valley at the CBM change from $MoSe_2$ to WSe_2, as shown schematically in Figure 1.15[39]. In the same set of alloys, the SOC induced spin-splitting of the upper VBs at **K** also changes significantly with composition, with magnitudes of up to hundreds of meV that are much larger than the splitting in the CB of around tens of meV[39]. Figure 1.15b shows the evolution of the energy difference between A and B excitons with W composition[39]. Although DFT predicts a linear change with composition, the optical measurements suggest that the change is non-linear.
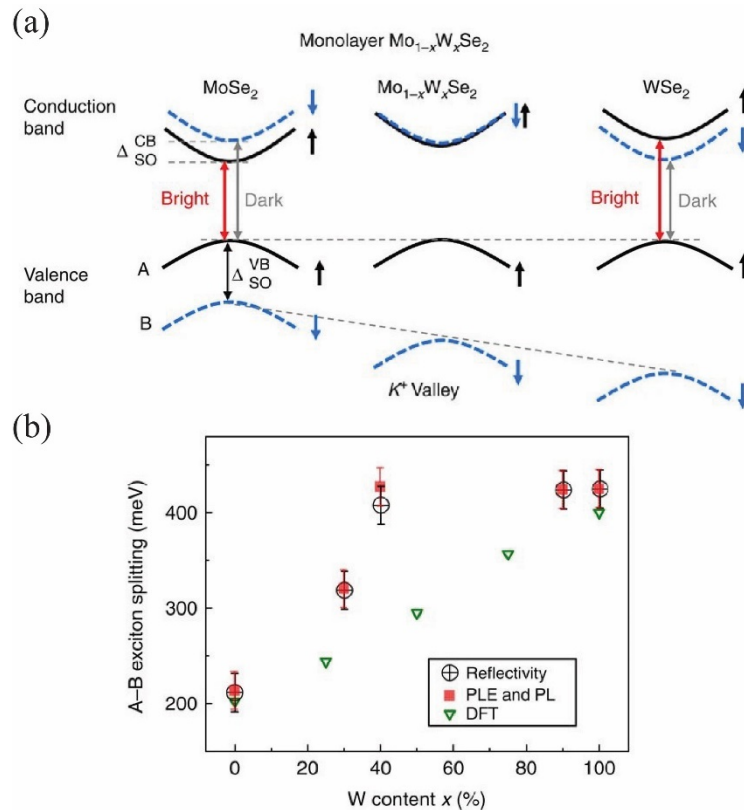
Figure 1.15. Spin-orbit engineering of $Mo_{1-x}W_xSe_2$ alloy monolayers. (a) Schematics of the evolution of the band structure at the **K** valley from $MoSe_2$ to WSe_2 showing the different signs and magnitudes of the VB and CB spin splittings. (b) Plot of the energy difference between A and B excitons against the W content. Adapted from Ref. 39.

Optical spectroscopy, measuring the difference in energy of the A and B exciton emission, has also been used to infer the spin-splitting in pure monolayer flakes of MoS_2[65,66], WS_2 and WSe_2[65,67]. However, the PL measures excitons, it is not a direct measurement of the electronic structure[39]. As shown schematically in Figure 1.15b, the energy difference between A and B exciton depends on the band gaps and the SOC splitting of both CB and VB, complicating determination of SOC splitting from these measurements[39]. The significant exciton binding energies must also be taken into consideration. Hence, finding an alternative technique that can give direct and precise results on determination of the electronic structure becomes an outstanding question.

1.3.3 Applications of TMD alloys

As described before, the Mo atoms in $MoSe_2$ can be replaced by Nb atoms that make the Nb-doped $MoSe_2$ a p-type material. Using this, a van der Waals homojunction p-n diode can be fabricated which exhibits typical rectifying behaviour at room temperature, as shown in Figure 1.16b[53]. Compared to heterojunctions composed of different TMDs, the homojunction p-n diode displays more efficient current rectification and photovoltaic response since its interface with continuous band bending contains fewer carrier trap sites than those of the heterojunctions[53]. Therefore, TMD alloys not only provide abundant building blocks with control over the material properties, but also present novel ways for constructing active devices[53,68].
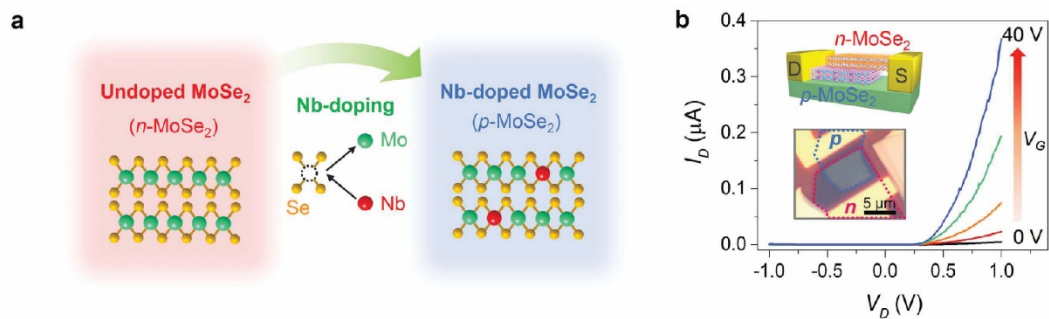
Figure 1.16. Vertical stacked homojunction p-n diode in $MoSe_2$. (a) Schematic on Nb-doping mechanism for p-type $MoSe_2$. (b) V_G-dependent rectifying behaviour of the $MoSe_2$ homojunction p-n diode in the log scale. Inset: Schematic and optical micrograph of the homojunction p-n diode. Adapted from Ref. 53.

1.4 Thesis outline

This thesis focuses on exploring the atomic and electronic structure of 2D TMD alloys. The synthesis of single crystals of TMD alloys by CVT is presented, along with techniques to reduce the materials to monolayer form on target substrates by mechanical exfoliation. Various procedures for the subsequent assembly of van der Waals stacks have been developed as part of this work, in order to achieve high-quality heterostructures suitable for high-resolution microscopy and spectroscopy investigations. The atomic structure of the TMD alloys $Mo_{1-x}W_xS_2$ and $Nb_{1-x}W_xS_2$ have been characterised via ADF-STEM images, with quantitative statistical analysis such as calculation of the Warren-Cowley short-range order (SRO) parameters. The electronic structure of these materials has been investigated by ARPES. First principles calculations have been performed to compare with and explain the experimental results.

Chapter 2 introduces the core experimental techniques that are applied in this thesis, e.g. CVT, Raman spectroscopy and PL, ADF-STEM and ARPES. The procedures for the growth of 2D single crystals by CVT and for the isolation of monolayers by mechanical exfoliation are also described.

Chapter 3 presents the optimised synthesis conditions for single crystals of $Mo_{1-x}W_xS_2$ and $Nb_{1-x}W_xS_2$ alloys via CVT. Various techniques for the assembly of van der Waals stacks are explained with examples, e.g. the pick-and-place and PMMA transfer method. In addition, a novel way has been developed for the fabrication of encapsulated TMD samples in such a way as to enable high-resolution ADF-STEM imaging with large contamination-free regions.

Chapter 4 presents quantitative analysis of the atomic structures of $Mo_{1-x}W_xS_2$ monolayers, as revealed by ADF-STEM imaging. Quantitative comparison with Monte Carlo simulations, parameterised by first principles calculations, shows that the atomic distributions are random, as expected from a growth process at high temperature. ARPES measurements of $Mo_{1-x}W_xS_2$ bulk crystals are used to directly determine the changes in VB structure with composition and are compared to optical spectroscopy and linear scaling DFT predictions. The changes with composition of key parameters, such as band gaps, VB SOC splittings and effective mass *etc.*, are presented.

Chapter 5 demonstrates the atomic structures of the $Nb_{0.1}W_{0.9}S_2$ and $Nb_{0.17}W_{0.83}Se_2$ monolayers via ADF-STEM images. The $Nb_{0.1}W_{0.9}S_2$ shows obvious ordered atomic lines along one of the equivalent crystallographic directions, while $Nb_{0.17}W_{0.83}Se_2$ reveals random atomic distributions. Linearly polarised Raman spectroscopy is applied to explore how these atomic lines affect the lattice vibrations. To support these measurements of the atomic structure, PL and ARPES measurements are used to explore the electronic structure of $Nb_{0.17}W_{0.83}Se_2$.

Chapter 6 summarises the results and contributions of this thesis and includes an outlook over the future work that should be continued in this area.

Chapter 2: Experimental Techniques

2.1 Material synthesis

As described in Chapter 1, for the experimental work presented in this thesis, CVT followed by mechanical exfoliation and stacking was the preferred method for sample fabrication. Since the bonding between grown monolayer TMD flakes and their substrates is much stronger than that of exfoliated samples, mechanical exfoliation is more suited to the fabrication of artificial heterostructures by stacking[18]. Compared to CVD-grown TMD materials, monolayer TMD flakes isolated by mechanical exfoliation are clean and highly crystalline, so exfoliated TMD based devices are cleaner and more stable[11]. Moreover, in terms of TMD alloy growth, the atomic distribution in TMD alloy flakes synthesised by CVT is more homogeneous than those grown by CVD method, as introduced in section 1.3.1.

2.1.1 Chemical vapor transport (CVT)

For CVT, there are two steps in the synthesis process: TMD alloy powder preparation; and CVT from this powder to single crystals. During compound preparation, powders of the metal and chalcogenide elements are mixed and added to a small ampoule, stoichiometrically. The ampoule is evacuated and sealed and placed in a box furnace, as
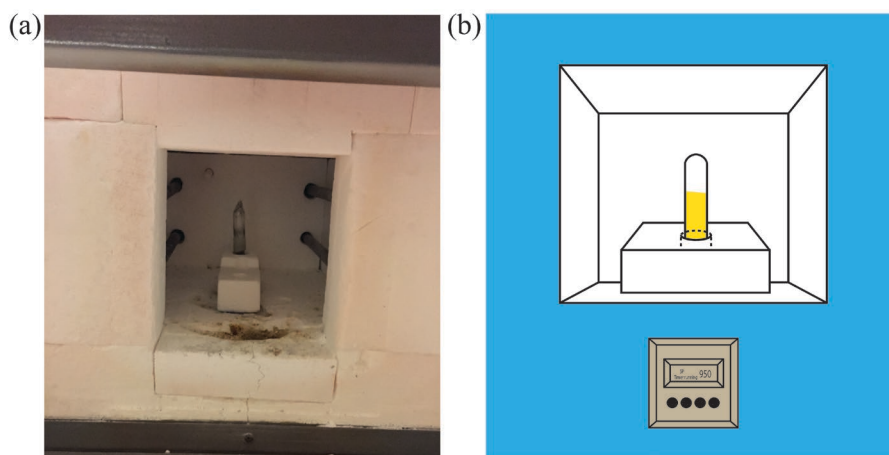
Figure 2.1. Box furnace for preparation of the alloy powders. (a) Photo of a box furnace. (b) Schematic diagram showing the furnace during the heating cycle.

shown in Figure 2.1, to heat up to a high temperature for the formation of the alloy TMD compounds.

A mixture of the alloy compounds and transport agent, here iodine, is added to a new quartz ampoule with larger inner diameter which is evacuated and sealed for crystal growth. A tube furnace with three zones with independent temperature control is used, as shown schematically in Figure 2.2b. The temperature of the source and growth zone is ramped to (T + ΔT) and T, respectively, and maintained at those temperatures for the required time period. The temperature profile along the furnace is shown in Figure 2.2b. Finally, the furnace is allowed to cool to room temperature.
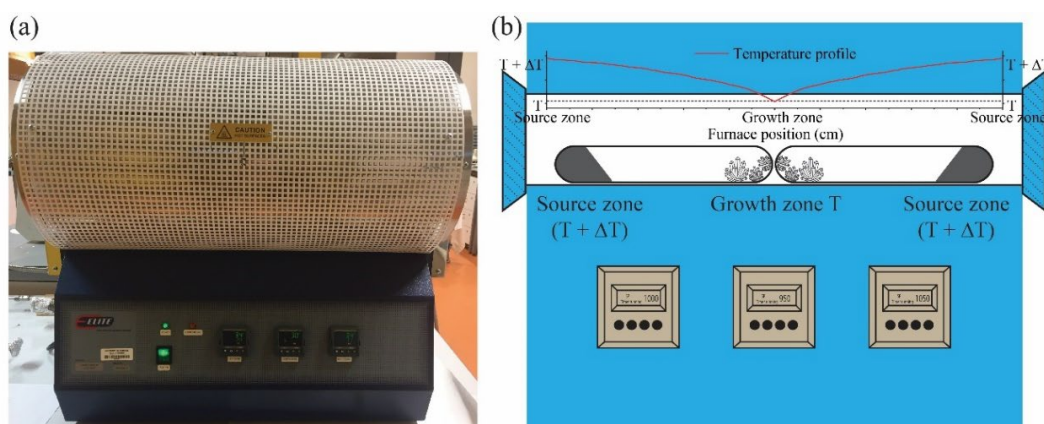
Figure 2.2. A tube or three-zone furnace for CVT. (a) Photo of three-zone furnace. (b) Schematic diagram of the furnace during heating for CVT, with measured heating profile along the tube.

2.1.2 Mechanical exfoliation

Figure 2.3 schematically shows a typical process for mechanical exfoliation: a scotch tape is placed on thin graphite or TMD crystals to peel off a few layers, then the tape with these layers is stuck to a substrate, normally a SiO_2/Si wafer[69]. These layers are further cleaved after the tape is removed, single or multi-layer TMD flakes can be observed under an optical microscopy as shown in Figures 2.3a and 2.3b[11].
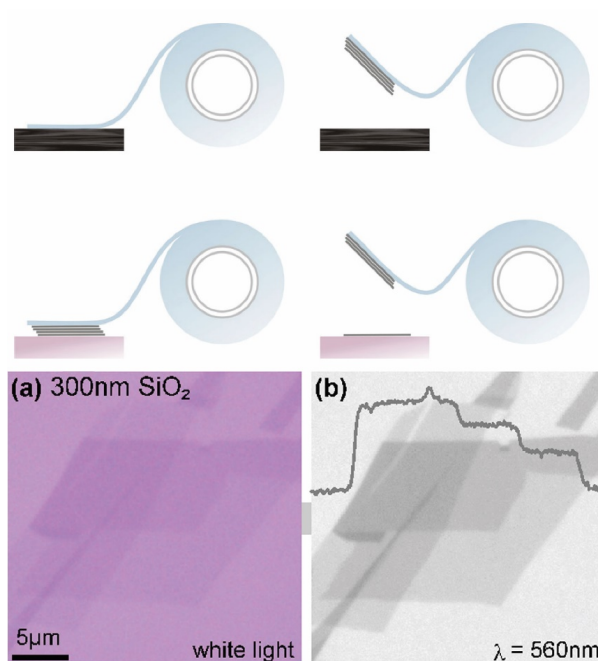
Figure 2.3. The mechanical exfoliation procedure and optical images of exfoliated flakes. Top: Schematic diagram showing the procedure for micromechanical exfoliation using scotch tape. Adapted from Ref. 11. Bottom: optical image of exfoliated graphene on 300 nm SiO_2/Si with (a) white light and (b) 560 nm light. Adapted from Ref. 69.

This process has been developed and improved to obtain bigger flakes via optimising the fabrication conditions. For example, gold (Au) substrates can be excellent alternatives to SiO_2/Si wafers, since the chemical adhesion between Au and sulphur is stronger than between sulphur and SiO_2[70]. The polymer adhesion layer of tape can be optimised. Moreover, the exfoliated flakes increase from several tens of microns to hundred microns via raising the exfoliation temperature[71].

2.2 Raman spectroscopy

2.2.1 Light-matter interaction

Incident photons interacting with atoms and molecules can be absorbed or scattered. The scattering mechanisms can be divided into two types, elastic (Rayleigh scattering) and inelastic (such as Raman scattering) as shown in Figure 2.4a[72]. For Rayleigh scattering, the energy and momentum of the incident and transmitted photons will be
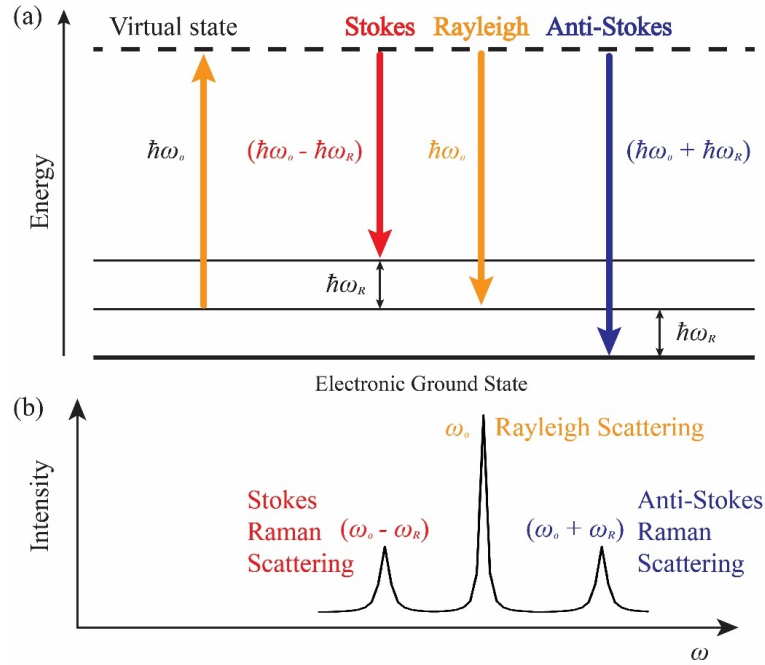
Figure 2.4. Schematic diagram of a scattering process. (a) Schematic diagram shows the virtual state reached by the excitation and the emission processes corresponding to the different transitions. (b) Schematic of the corresponding Raman spectrum.

conserved during the scattering processes[72,73]. While for an inelastic scattering process, the scattered photons have different energies compared to the incident photons[72,73].

Figure 2.4b shows schematically the scattering intensity versus frequency for a photon incident on a material, with peaks corresponding to Stokes and anti-Stokes Raman scattering as well as Rayleigh scattering[72,73]. In the Stokes Raman scattering process, an incident photon creates a scattered photon of lower energy as well as a phonon, so the Stokes scattering line is shifted to lower energy compared to the Rayleigh scattered line, as indicated in red colour[72,73]. In contrast, in anti-Stokes Raman scattering a phonon and incident photon combine to emit a scattered photon of higher energy, so the anti-Stokes line is blue-shifted, as indicated by the blue-coloured transition in Figure 2.4[72,73].

When a material is placed in the electric field (E) of an incident light, an electric dipole will be induced within the material. The dipole moment (μ) can be related to the electric field (E) as following[72–76]

$$\boldsymbol{\mu} = \tilde{\boldsymbol{\alpha}} \, \boldsymbol{E} \,, \qquad\qquad 2.1$$

in which $\tilde{\boldsymbol{\alpha}}$ is the molecular polarizability[72–76].

The external electric field can be written as[72–76]

$$\boldsymbol{E} = \boldsymbol{E_0} \cos(\omega_0 t) \,, \qquad\qquad 2.2$$

in which $\boldsymbol{E_0}$ is the vector amplitude of the external electric field, and ω_0 is its oscillation frequency[72–76].

For a small nuclear displacement, the change of polarizability can be expanded as a Taylor series[72–76],

$$\alpha = \alpha_0 + \left(\frac{\partial \alpha}{\partial q}\right)_{q_0} q + \cdots . \qquad\qquad 2.3$$

where q is individual normal mode. Oscillations with characteristic frequency ω_q along each normal coordinate q can be excited, thus[72–76]

$$q = q_0 \cos(\omega_q t) \,. \qquad\qquad 2.4$$

To insert equation 2.2 and 2.3 into 2.1, then it yields[72–76]

$$\mu(t) = \alpha_0 \cdot \boldsymbol{E_0} \cdot \cos(\omega_0 t) + \frac{1}{2}\left(\frac{\partial \alpha}{\partial q}\right)_{q_0} \cdot q_0 \cdot \boldsymbol{E_0} \cdot \cos[(\omega_0 - \omega_q)t]$$

$$+ \frac{1}{2}\left(\frac{\partial \alpha}{\partial q}\right)_{q_0} \cdot q_0 \cdot \boldsymbol{E_0} \cdot \cos[(\omega_0 + \omega_q)t] \qquad\qquad 2.5$$

There are three terms in this equation. The first term $\alpha_0 \cdot E_0 \cdot \cos(\omega_0 t)$ oscillates at the same frequency as the incident radiation, corresponding to Rayleigh scattering[72–76]. The second term is red-shifted to lower frequency, corresponding to Stokes scattering[72–76]. The last term is characterised by the frequency $(\omega_0 + \omega_q)$, blue-shifted compared to the frequency of the incident radiation, hence it represents anti-Stokes scattering[72–76].

Following Equation 2.5, the selection rule for Raman scattering is that the derivative of the polarizability along the q-th normal coordinate must be non-zero value, $\left(\frac{\partial \alpha}{\partial q}\right)_0 \neq 0$. This is illustrated schematically for the example of a small molecule in Figure 2.5[73,76], two vibrational modes are indicated by the light-yellow arrows. The vibration mode with anisotropic polarizability $\left(\frac{\partial \alpha}{\partial q}\right)_0 \neq 0$ is Raman active, while the vibration with isotropic polarizability $\left(\frac{\partial \alpha}{\partial q}\right)_0 = 0$ is Raman inactive[73,76].

There are many limitations of the classical theory of Raman scattering[73]. For example, one of the failures is that the ratio of the Stokes and anti-Stokes intensities in experiments is not in agreement with the prediction of the classical theory. Specifically, the ratio of the Stokes and anti-Stokes intensities according to the classical theory yields $I_{Stokes}/I_{anti-Stokes} \propto (\omega_0 + \omega_q)^4/(\omega_0 - \omega_q)^4$. However, the intensity of Stokes Raman scattering is much higher than anti-Stokes Raman scattering from experiments. Hence, quantum mechanics model is introduced and explains the intensity in experiments[72–76].
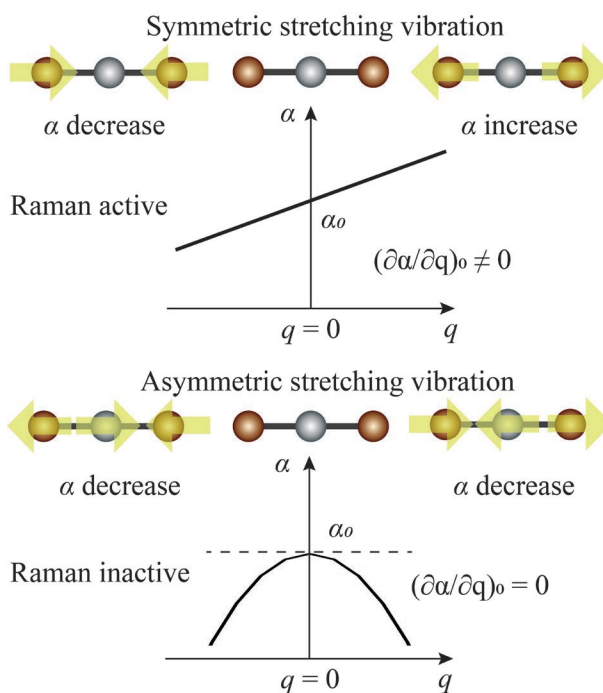
Figure 2.5. The polarizability of a molecule changes as a function of the nuclear displacements. The graphs schematically indicate the derivatives of the polarizability for different vibrational modes[73,76].

2.2.2 Confocal Raman spectrometers

For a confocal Raman spectrometer, a typical experiment setup is shown schematically in Figure 2.6a. There are three main parts to the Raman spectrometer, a laser source, a microscope and a spectrometer with CCD detector[73]. Since the Raman signals are weak, each part of this system has to be optimised to allow a reasonable signal passing through to the detector[73].

Figure 2.6b and 2.6c schematically show two typical setups for angle-resolved polarised Raman spectroscopy (ARPRS)[73,77,78]. In the first, the laser polarisation is fixed along the y axis while the analyser direction is set to either horizontal or vertical with respect to the laboratory coordinates[77,78]. The sample is rotated around the z axis by an angle θ (the angle between the sample coordinate and the laboratory coordinate) and the spectra are collected as a function of θ[77,78]. Figure 2.6c shows a setup with a half-wave plate, in this case the sample and laboratory coordinates are fixed and hence θ is known. However, the polarisation state of the laser can be controlled by rotating the fast axis of the half-wave plate. When the half-wave plate is rotated $\alpha/2$ from its fast axis, the incident laser polarisation is rotated α with respect to the y axis of the laboratory coordinate, in this way the spectra are collected as a function of $\alpha/2$.
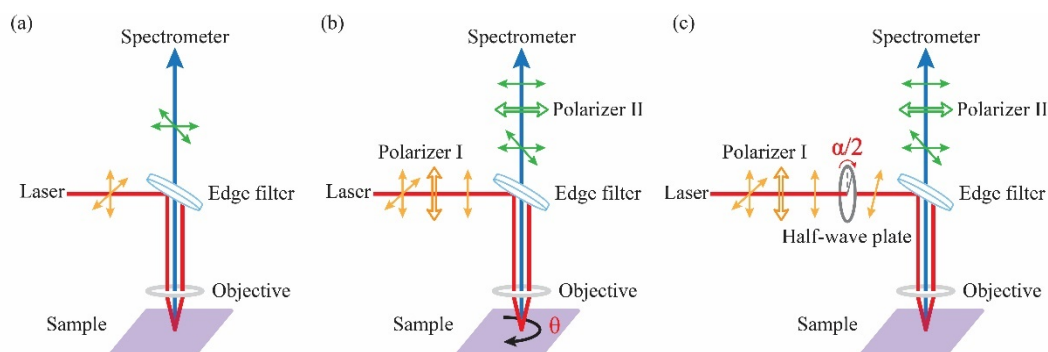
Figure 2.6. Schematic illustrations for the setups of typical confocal Raman spectrometers. (a) Schematic diagram shows a typical Raman spectroscope. Two setups for angle-resolved polarised Raman spectroscope (ARPRS) are shown in (b) and (c). In (b) the sample is rotated for angle-resolved measurements, while in (c) the polarisation state of the incident laser is controlled by a half-wave plate.

2.2.2.1 Raman shifts

For 2H-MX$_2$ polytype bulk crystals, the point group is D_{6h} (space group P6$_3$/mmc)[24,79]. There are 6 atoms in the unit cell, with 18 phonon modes, as shown in Figure 2.7: 3 acoustic and 15 optical modes[79]. Hence, the lattice vibrations at the Γ point can be expressed as the irreducible representations[79]

$$\Gamma = A_{1g} + 2A_{2\mu} + 2B_{2g} + B_{1\mu} + E_{1g} + 2E_{1\mu} + 2E_{2g} + E_{2\mu} . \qquad 2.6$$

Among these vibrations, one $A_{2\mu}$ and $E_{1\mu}$ are acoustic modes that are inactive; A_{1g}, E_{1g} and E_{2g} are Raman active modes; the other $A_{2\mu}$ and $E_{1\mu}$ are infrared active modes; and B_{2g}, $B_{1\mu}$ and $E_{2\mu}$ are silent modes that are optically inactive[79].

A typical Raman spectrum of a 2H-TMD bulk crystal is shown in Figure 2.8a[80]. In the back-scattering configuration, the E_{1g} mode, associated with an in-plane motion of only chalcogen atoms, is forbidden[79,80]. The E_{2g}^2 is a shared mode originating from the relative
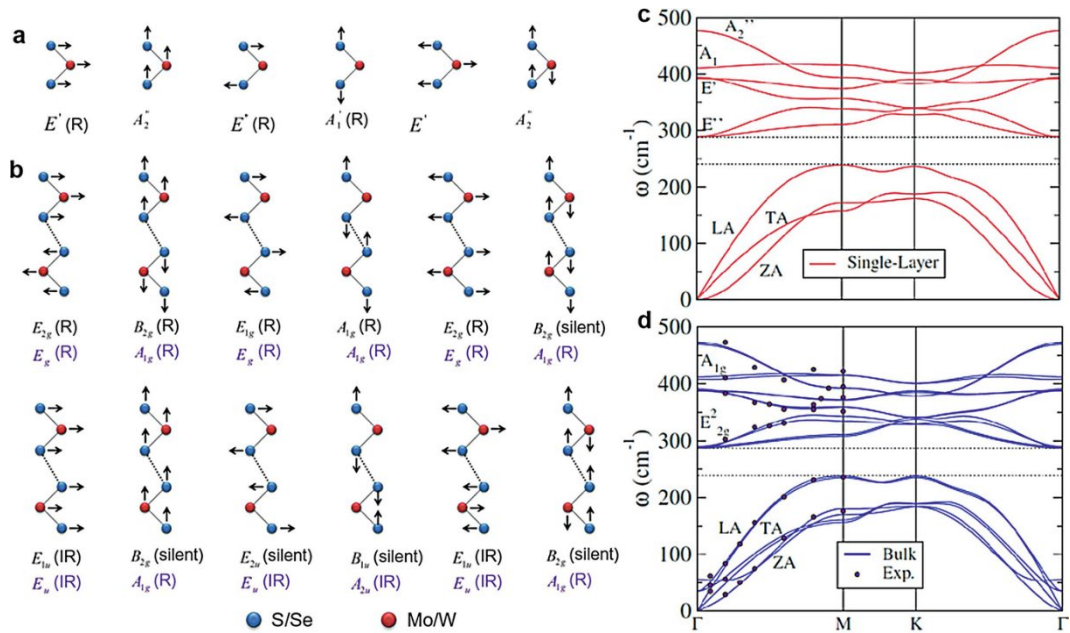
Figure 2.7. A summary of phonon modes for 2H-MX$_2$ monolayer and bulk crystals. Normal displacements of vibration modes for (a) monolayer and (b) bulk crystals. Adapted from Ref. 79. Calculated phonon dispersion curves of (c) monolayer and (d) bulk crystals for MoS$_2$. Adapted from Ref. 79.

motion of the atoms in different layers and is only observed in the very low frequency region[79]. Therefore, the dominant Raman scattering features are the two first-order Raman modes, E^1_{2g} and A_{1g}, as indicated in Figure 2.8a. The E^1_{2g} mode corresponds to the in-plane vibration of the metal and chalcogen atoms, while the A_{1g} mode is for the out-of-plane motion of the chalcogen atoms, as shown in Figure 2.7.

When the thickness of MX_2 is reduced to a monolayer, its symmetry is reduced to D_{3h} point group (space group P6m2), reducing the number of phonon modes to 9, as shown in Figure 2.7. The vibrations can then be expressed via the irreducible representations at the Γ point[79]

$$\Gamma = 2A_{2\mu} + E_{1g} + A_{1g} + 2E_{2g} ,\qquad\qquad 2.7$$

in which one of the $A_{2\mu}$ and the E_{2g} are acoustic modes; the other $A_{2\mu}$ is infrared active; A_{1g} and E_{1g} are Raman active modes; and the other E_{2g} mode is both Raman and infrared active[79].

A typical Raman spectrum from a TMD monolayer is shown in Figure 2.8a[80]. Due to the back-scattering geometry of the measurement, E_{1g} is again absent[80]. Therefore, the Raman modes E^1_{2g} and A_{1g} are still the dominant peaks in the Raman spectrum of the
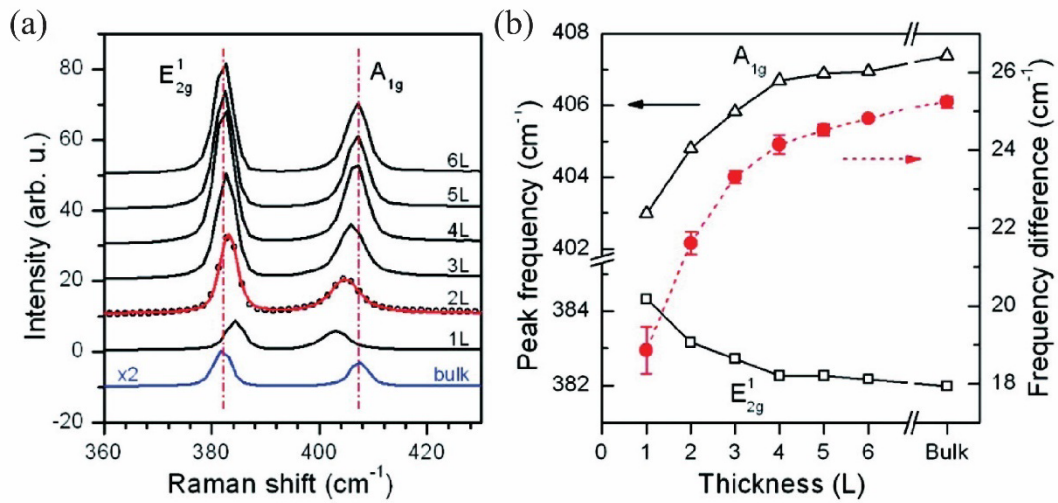
Figure 2.8. Raman spectra of bulk and monolayer MoS_2 crystals. (a) Raman spectrum of MoS_2 crystals with different layer numbers under 532 nm laser excitation. (b) Peak frequency of E^1_{2g} and A_{1g} modes as a function of sample thickness. Adapted from Ref. 80.

monolayer. Compared to bulk crystals, the E_{2g}^1 mode upshifts while the A_{1g} mode shifts to lower frequency, hence the Raman modes are sensitive to the number of layers, as shown in Figure 2.8b[80].

2.2.2.2 Linearly polarised Raman spectra

For a given Raman mode, the Raman scattering efficiency can be expressed as[24,72–76,81]

$$S = A|e_i \cdot R \cdot e_s|^2 ,$$

2. 8

where e_i is vector representing the polarisation direction of incident light and e_s represents the polarisation direction of the scattering light. R is the Raman tensor of the given Raman mode of the material. The Raman tensors are only related to the point group and the symmetry of the Raman modes, as listed in Table 2.1[24,81]. Finally, to detect the Raman signals, this efficiency needs to be a non-zero value.

Table 2.1. Raman tensors for hexagonal point group. Adapted from Ref 24,81.

Crystal system	Point group	Irreducible representations of Raman active modes and their Raman tensor				
Hexagonal	D_6	A_1	E_1	E_1	E_2	E_2
	C_{6v}	A_1	E_1	E_1	E_2	E_2
	D_{3h}	A'	E''	E''	E'	E'
	D_{6h}	A_{1g}	E_{1g}	E_{1g}	E_{2g}	E_{2g}

$$\begin{pmatrix} \alpha_{xx} & 0 & 0 \\ 0 & \alpha_{yy} & 0 \\ 0 & 0 & \alpha_{zz} \end{pmatrix} \begin{pmatrix} 0 & 0 & 0 \\ 0 & 0 & \alpha_{yz} \\ 0 & \alpha_{yz} & 0 \end{pmatrix} \begin{pmatrix} 0 & 0 & -\alpha_{xz} \\ 0 & 0 & 0 \\ -\alpha_{zx} & 0 & 0 \end{pmatrix} \begin{pmatrix} 0 & \alpha_{xy} & 0 \\ \alpha_{xy} & 0 & 0 \\ 0 & 0 & 0 \end{pmatrix} \begin{pmatrix} \alpha_{xx} & 0 & 0 \\ 0 & -\alpha_{xx} & 0 \\ 0 & 0 & 0 \end{pmatrix}$$

2.3 Electron microscopy

Experimental work using electron microscopy and related techniques is an essential part of this work, since allows direct imaging and provides direct structural information of the material. The latest generation of electron microscopes can resolve individual atoms, an essential requirement in 2D materials. Ernest Abbe worked out that the resolution of the optical instruments is limited by diffraction of the light[82], so the resolution of high quality visible light microscopes is limited by the wavelength of the illumination source and the optic apertures. Thus, the resolving power in light

microscopy, defined as the smallest distinguishable distance, d_0, is determined by the equation 2.9[82]

$$d_0 = \frac{0.61\lambda}{n\sin\alpha},$$ 2. 9

where λ is the wavelength of the radiation, n is the refractive index of the medium, and α is the collection semi-angle[82]. Additionally, the diffraction barrier restricts the optical instruments to distinguish two objects separated by a lateral distance less than $\sim\lambda/2$, with λ being the wavelength of light used by the instrument. This diffraction limits the resolution of a good optical microscope to approximately 200 nm[82]. However, this resolution is not enough to image many features in materials, *e.g.* dislocations and grain boundaries[82].

Using high energy electrons as an illumination source, electron microscopy can achieve improved spatial resolution compared with other microscopy techniques[82]. According to de Broglie's equation, and taking into consideration relativistic corrections for voltages higher than 100 kV, the wavelength of the electrons when accelerated by a potential difference V can be calculated using equation 2.10:

$$\lambda = \frac{\hbar}{\left[2m_0 eV\left(1+\frac{eV}{2m_0 c^2}\right)\right]^{1/2}}.$$ 2. 10

where $\hbar$ is the Planck's constant, m_0 is the electron mass and c is the speed of light[82].

The calculated wavelength of electrons at 80 and 200kV (accelerating voltages in the TEMs used in this thesis) are $\sim$ 0.04 and 0.03 Å, respectively[82]. These wavelengths are even smaller than atomic diameters and therefore theoretically, any electron microscope operating at 200 kV should be able to image individual atoms[82]. However, the diffraction and spherical and chromatic aberrations limit the resolution of conventional electron microscopes, and the resolution limit of an electron microscope at 200 kV is $\sim$2 Å, which is not enough to resolve individual atoms in a non-periodic structure. Both spherical and chromatic aberrations are unavoidable in the static rotational symmetric electromagnetic lenses that constitute the electron microscope. Further details about the aberration correction in electron microscopy can be found in section 2.3.2.
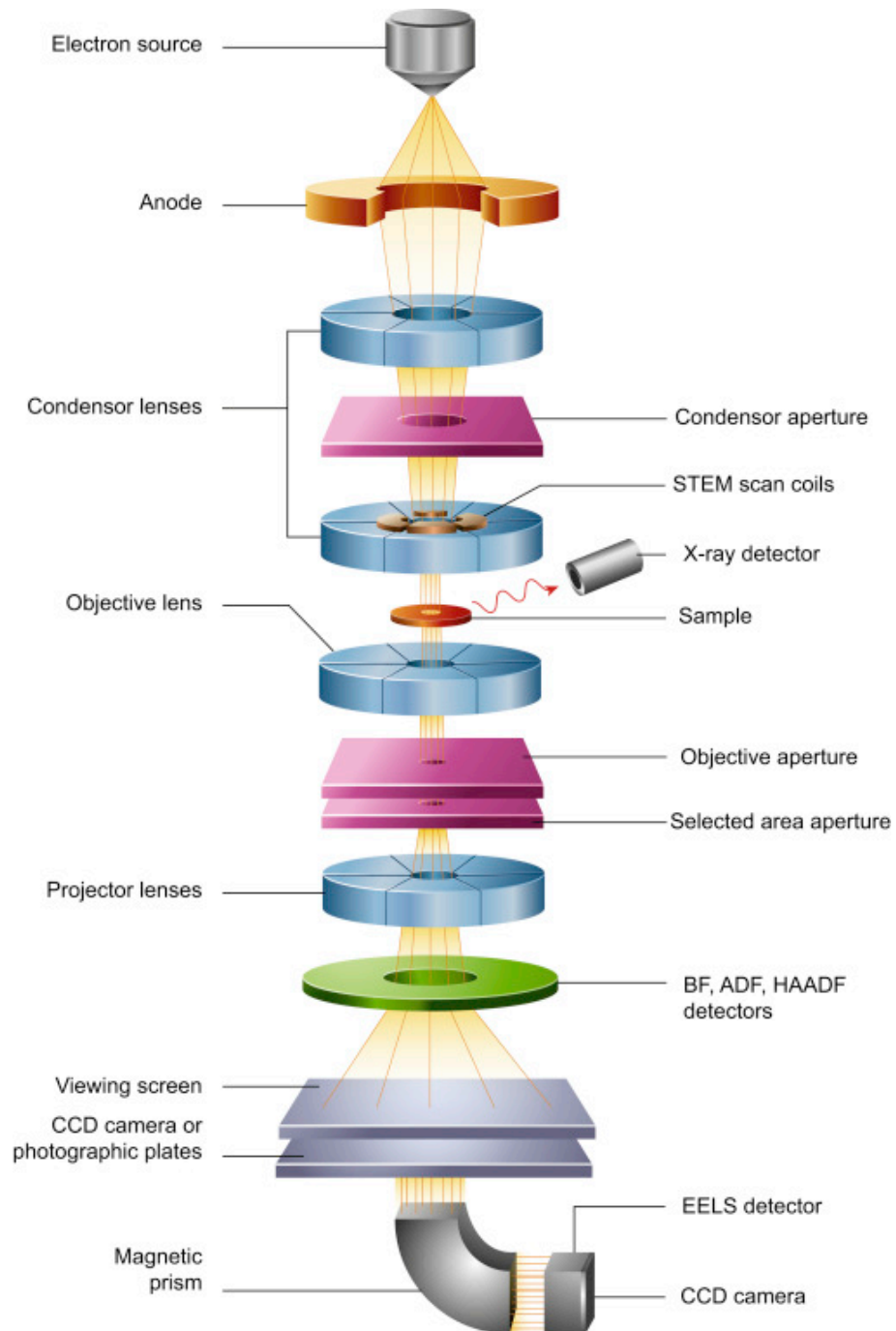
Figure 2.9. Schematic cross-section of a modern TEM. The vacuum system is not shown here. Adapted from Ref. 83.

In a conventional transmission electron microscopy (CTEM), the sample is illuminated by a plane wave of electrons generated by the electron gun either through a thermionic or field emission process. After the interaction of this plane wave with the specimen, the transmitted electrons are projected onto an electron detector, forming an image. Figure 2.9 corresponds to a schematic diagram of a TEM[83]. The electrons are
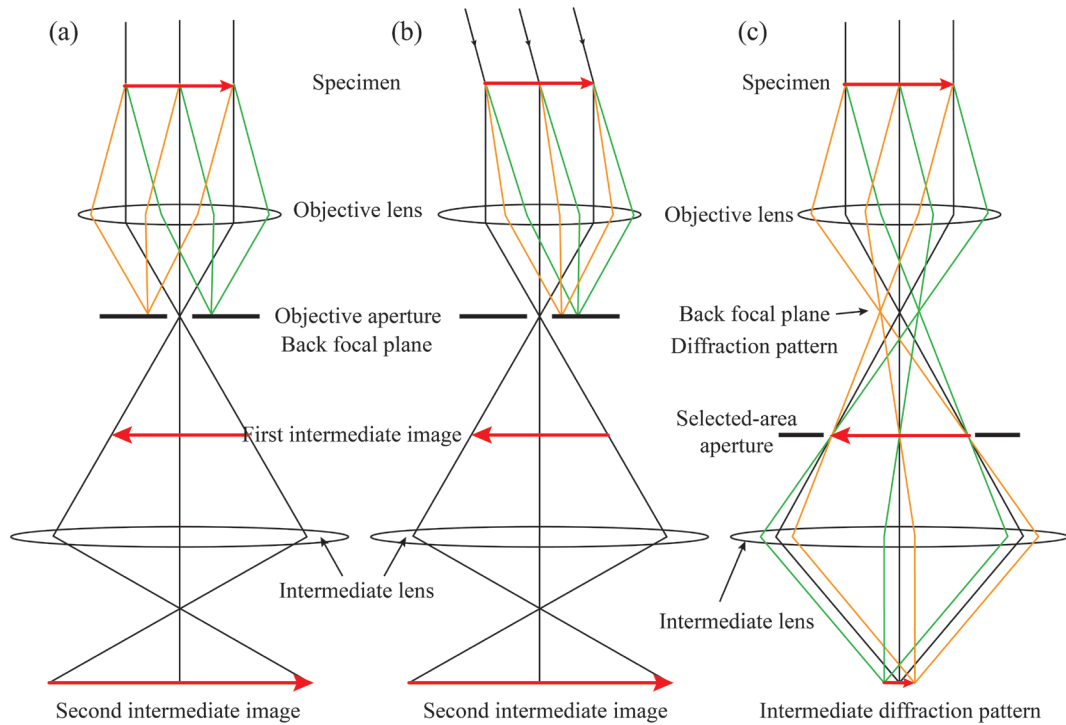
Figure 2.10. Schematic ray diagram of three basic operation modes in a TEM. (a) Bright-field (BF) image. (b) Dark-field (DF) image. (c) Selected area diffraction mode. Adapted from Ref. 82.

generated by the electron gun either through a thermionic or field-emission process before accelerated to the typical working voltage, 80 or 200 kV for the analysis carried out in this PhD.

Once extracted, the condenser lens system (upper lenses) of the TEM allows the probe formation to certain size. The condenser system (lenses and apertures) also determines the type of illumination, i.e. parallel or convergent electron beam. In a microscope, the objective lenses are the most important lens which generate the first intermediate image determining the resolution of the final image. The objective lens may focus the transmitted and scattered beams into the back focal plane (BFP), forming a diffraction pattern, or further down into the image plane, forming an image of the specimen. The intermediate and projector lens magnify the image/diffraction pattern onto the detection system, i.e. a CCD camera to capture the signal.

Additional electron beam deflectors may be installed before the specimen, called scan coils, which have different uses. Although the key use is to scan the electron beam across

the specimen in STEM mode, they can also be used to tilt a parallel electron beam to work in conventional dark-field TEM imaging mode.

Nowadays, state-of-the-art microscopes incorporate further lenses to correct for example the spherical aberration before and after the specimen (probe and image correction) improving enormously the spatial resolution of the electron microscopes.

2.3.1 TEM and STEM

In conventional TEM mode (Figure 2.11), a broad close-to-parallel electron beam illuminates the area of interest in the specimen[84]. The electrons interact with the matter through a range of different mechanisms, generating a wide range of signals that can be used to analyse the material. Different modes of imaging can be achieved by selecting different electrons. The two basic modes of TEM imaging operation are bright-field (BF) and dark-field (DF) mode as shown in Figure 2.10a and 2.10b, respectively[82,85]. An aperture is positioned to pass only the un-deflected (direct) transmitted electrons in the former and to pass some diffracted electrons in a particular diffraction condition in the latter. These operating modes in TEM using an objective aperture will provide strong
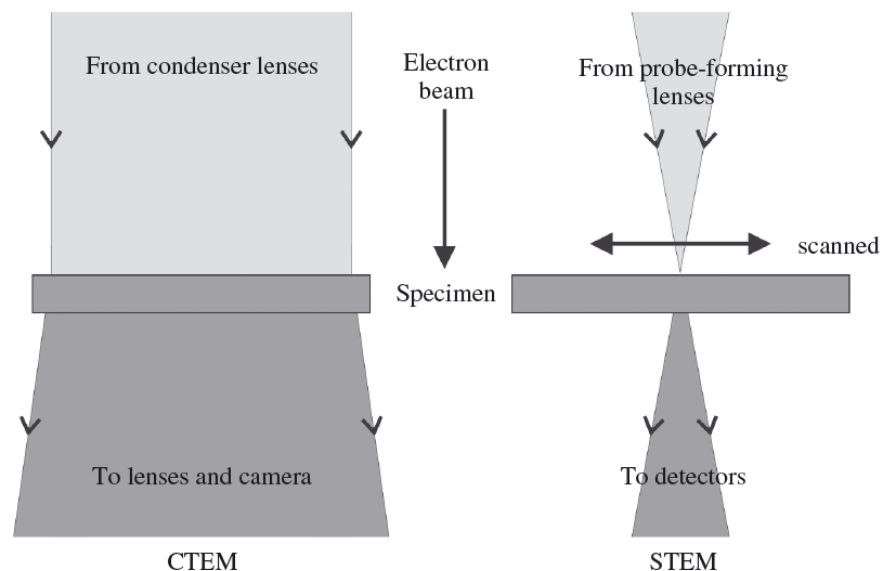
Figure 2.11. The electron beam in CTEM and STEM instruments. Schematic ray diagram of a CTEM (at left) and STEM (at right) passing through the specimen. There are STEM instruments with the beam travelling upwards. Adapted from Ref. 84.

diffraction contrast imaging since the diffracted intensity does not recombine with the straight through beam intensity (or vice versa) to form the image.

If no aperture is used, a mass-thickness contrast image is formed. To obtain lattice images, a large objective aperture will be introduced allowing many beams, including the direct beam, to pass. This generates a phase contrast image formed by the interference of the diffracted beams with the direct beam. This technique, also called high-resolution TEM (HRTEM), can be used to investigate the atomic structure of crystalline materials. The microscope affects the image contrast, and this is described by the Contrast Transfer Function (CTF), which is expressed as the contrast dependence on reciprocal lattice spacing for a given objective lens defocus.

Figure 2.10c is a ray diagram corresponding to the generation of a diffraction pattern in the TEM[82]. Here another aperture (different to the objective one) is introduced to limit the diffraction pattern to a selected area of the sample. This technique is known as selected
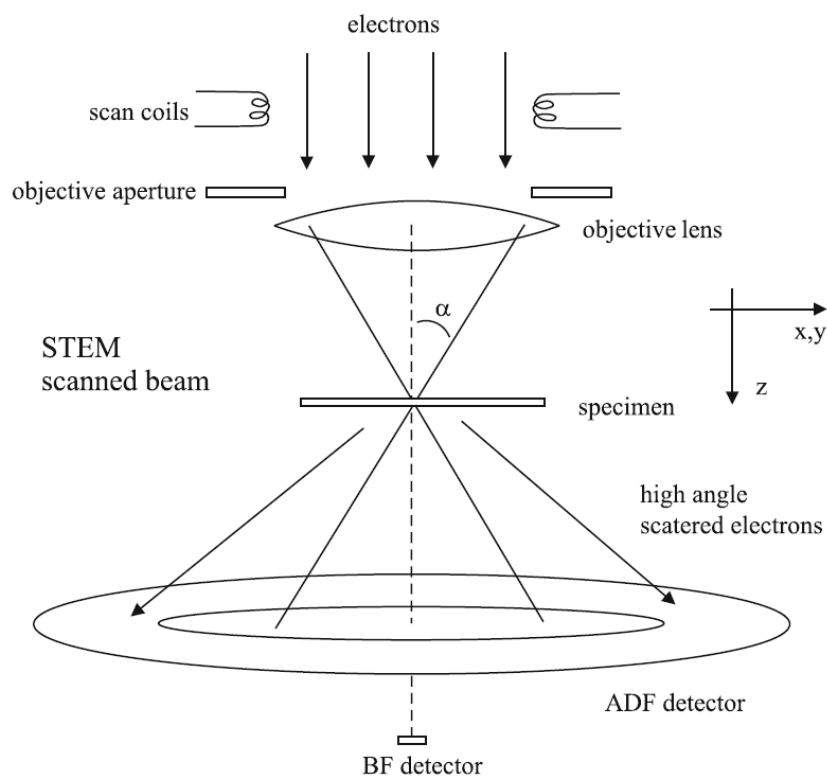
Figure 2.12. Schematic diagram of the bright field (BF) and concentric ADF detectors in STEM mode. Adapted from Ref. 86.

area electron diffraction (SAED). A diffraction pattern consisting of the direct and the diffracted beams coming from the ROI will be imaged in the viewing screen and collected by a CCD device.

In STEM mode, the electron beam is converged into a single narrow probe on the specimen (Figure 2.11), forming a convergent beam electron diffraction pattern (with overlapping disks) in the BFP[84]. The convergent beam is scanned across the specimen, originating in a convergent beam diffraction pattern for each pixel. The size of the disks depends on the convergence angle and overlapping of the disks is required in order to resolve the structure[82,84]. The probe size is inversely proportional to the convergence semi-angle[82,84]. Each diffraction disk subtends the same semi-angle, and overlapping disks are required to allow atomic resolution imaging in STEM[82,84]. At each point (x,y) on the specimen an intensity of electrons is collected to form the image. Depending on the position of the detector and the detection angle different images can be formed (see Figure 2.12)[86]. The most common imaging detector is an ADF detector that is a ring centred on the optic axis (see Figure 2.12)[86]. Usually, the inner radius of this detector is chosen such that no directly transmitted electrons are detected and the signal depends only on electrons deflected by a sufficiently large angle. A small on-axis detector, with an outer collection angle typically less than 5 mrad, produces a BF-STEM image.

Although there are many different modes to work in TEM and STEM, the achievable resolution of the electron microscopes is mainly limited by the inherent aberration of the lenses, as mentioned before. This has been a key point to obtain 2D-materials images, so the aberrations, how to correct them and the main imaging technique used to analyse 2D materials are as follow.

2.3.2 Aberration-corrected CTEM and STEM

2.3.2.1 Aberrations

Conventional magnetic electron lenses are ~ 100 times worse than the optical lenses, due to aberrations. The Scherzer theorem states "*Spherical and chromatic aberrations are unavoidable for static rotationally symmetric charge-particle lenses free of space charges*" [87]. Nevertheless, there are many aberrations in the convergent electromagnetic lenses, affecting the path of the electrons.

For high resolution TEM the wave aberration function is defined as the phase difference $\chi_{x,y}$ or distance difference $W_{x,y}$ in the path of the ideal spherical wave and an actual wavefronts in the diffraction plane due to the lenses[87]

$$\chi = \frac{2\pi}{\lambda} W \ . \qquad\qquad 2.\ 11$$
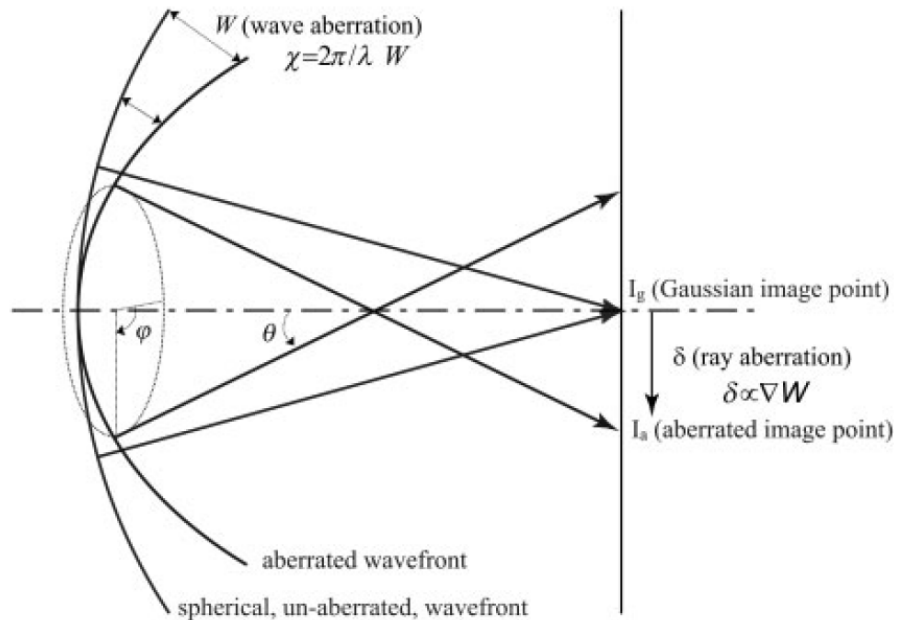
Figure 2.13. Wave and ray aberration. The wave aberration W measures the distance by which an aberrated wavefront deviates from the ideal spherical case. The corresponding phase difference is called the aberration function χ. The shift of the Gaussian image point due to the aberrations is called the ray aberration. The ray aberration δ is proportional to the gradient of the wave aberration W. Adapted from Ref. 87.

Figure 2.13 corresponds to a schematic representation of the wave aberration function $\chi_{x,y}$ and the ray aberration (δ_r). The 2D surface can be expressed as a function of the angle θ to the optic axis and the azimuthal angle φ around the optical axis[87].

The wave aberration function expanded as a Taylor series is described in equation 2.12. Using polar notation makes the azimuthal and radial dependence of some of the terms more apparent[87,88],

$$\chi(\theta, \varphi) = cst + \frac{\theta^{N+1}}{N+1}\{C_{NSa}\cos(S\varphi) + C_{NSb}\sin(S\varphi)\}$$

$$= cst + \theta\{C_{01a}\cos(\varphi) + C_{01b}\sin(\varphi)\}$$

$$+ \frac{\theta^2}{2}\{C_{10} + C_{12a}\cos(2\varphi) + C_{12b}\sin(2\varphi)\}$$

$$+ \frac{\theta^3}{3}\{C_{23a}\cos(3\varphi) + C_{23b}\sin(3\varphi) + C_{21a}\cos(\varphi) + C_{21b}\sin(\varphi)\}$$

$$+ \frac{\theta^4}{4}\{C_{30} + C_{34a}\cos(4\varphi) + C_{34b}\sin(4\varphi) + C_{32a}\cos(2\varphi) + C_{32b}\sin(2\varphi)\}$$

$$+ \frac{\theta^5}{5}\{C_{45}\cos(5\varphi) + C_{45b}\sin(5\varphi) + C_{43a}\cos(3\varphi) + C_{43b}\sin(3\varphi) + C_{41a}\cos(\varphi) + C_{41b}\sin(\varphi)\}$$

$$+ \frac{\theta^6}{6}\{C_{50} + C_{56a}\cos(6\varphi) + C_{56b}\sin(6\varphi) + C_{54a}\cos(4\varphi) + C_{54b}\sin(4\varphi) + C_{52a}\cos(2\varphi) + C_{52b}\sin(2\varphi)\}$$

$$+ \cdots, \qquad\qquad 2.12$$

where the numerical coefficient C_{NS} is defined as the aberration coefficients, N is the order of the aberration, S denotes azimuthal symmetry of the aberration, and cst is initial constant term[87,88]. Figure 2.14 shows the surface plots of individual terms in the aberration function from 0th to 5th order. For N = odd and S = 0, it means a round aberration with no azimuthal dependence, *e.g.* defocus and spherical aberration *etc.*[87,88]
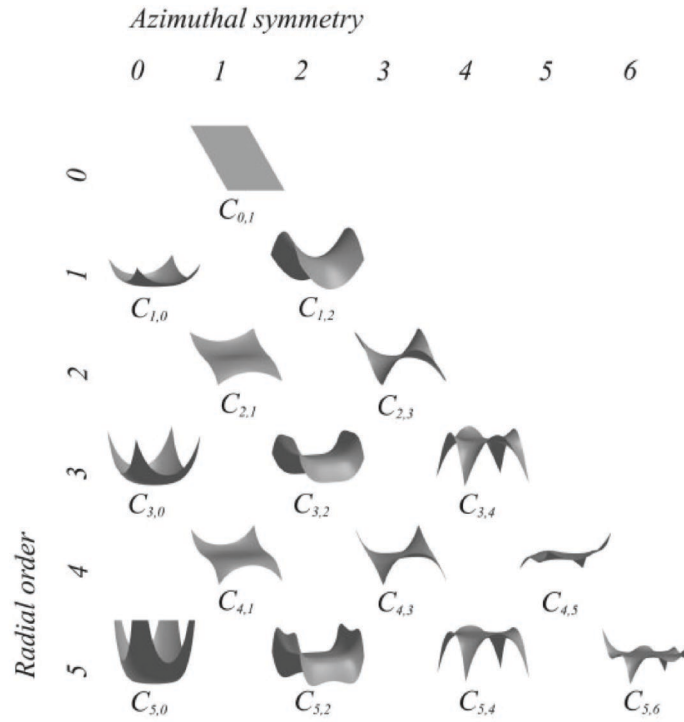
Figure 2.14. Aberration coefficients from 0th to 5th order. Adapted from Ref. 87.

For non-round aberrations (S $\neq$ 0), the C_{NSa} and C_{NSb} coefficients represent the projection of the overall aberration C_{NS} along two orthogonal axes[87,88].

Figure 2.15 shows the ray diagrams illustrating the change in focus for some of the main aberrations of the electron optics, such as chromatic aberration, spherical aberration, astigmatism and coma[89]. Explained in simple terms, the chromatic aberration of the lenses causes electrons with different wavelengths to focus at different points on the optic axis as shown in Figure 2.15a[89]. For spherical aberrations, C_3, the electrons through the periphery of the lens are focused more strongly than those close to the axis. As a consequence, in the image plane each point of an object is imaged as a disk due to different distances at the optical axis as shown in Figure 2.15b[89]. The two-fold axial astigmatism, $C_{1,2}$ brings the incoming wavefront of the electron rays traveling at different azimuths to different focus points as shown in Figure 2.15c[89]. Axial coma aberration, $C_{2,1}$ will displace radially the centers of concentric circles (Figure 2.15d[89]) and distorts a round beam into a characteristic comet shape.

(a) Chromatic aberration

E1
E2

E2
E1

Plane of least
confusion

(b) Spherical aberration

Disc of least
confusion,
diameter d$_g$

α

Plane of least
confusion

(c) Astigmastism
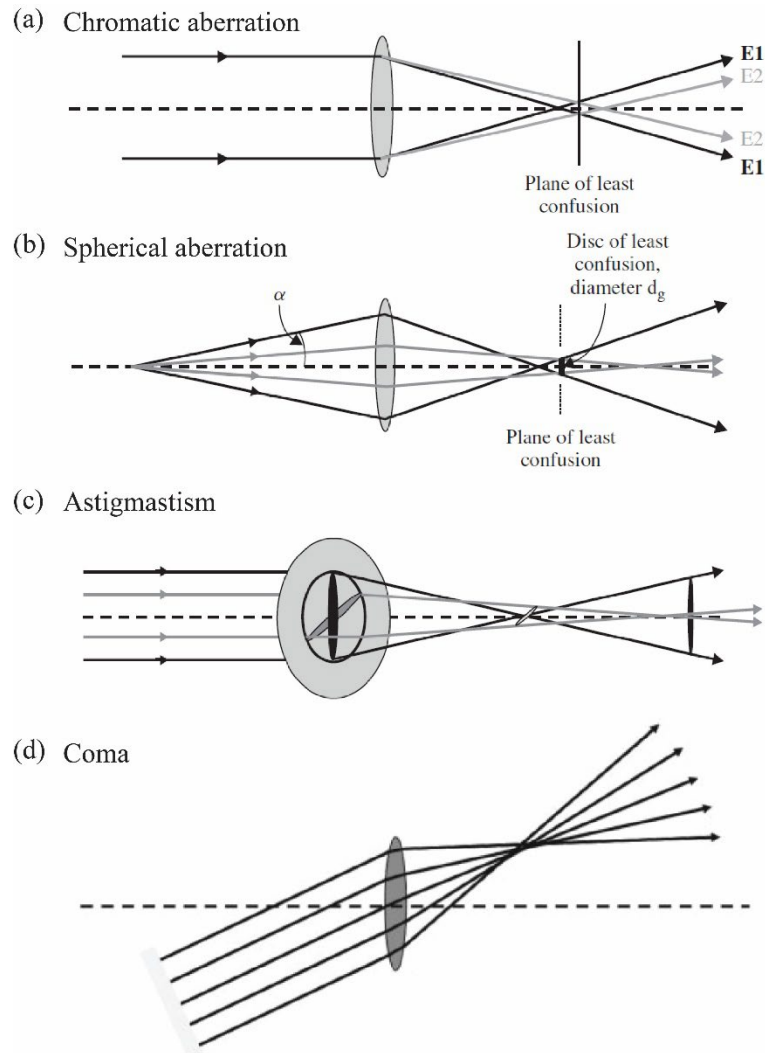
(d) Coma

Figure 2.15. Aberrations in the lenses. (a) Chromatic aberrations in the lenses result waves of different wavelengths and energies are focused to different points along the optic axis. (b) Spherical aberration. (c) Astigmatism. (d) Coma aberrations cause the beam to focus off-axis. Adapted from Ref. 89.

2.3.2.2 Spherical aberration-correction

Electromagnetic lens aberrations affect not only image formation but also the resolving power in STEM, since the probe-forming depends on a combination of the diffraction limit and the aberrations of the lenses. In an aberration-corrected STEM, a multi-multipole lens probe aberration corrector is inserted between the condenser system and the probe forming lens[87]. However, for an aberration-corrected TEM, an image corrector is placed after the objective lens[87]. The first step to compensate the aberrations in the microscope illumination system is to measure such aberrations. This can be achieved

41

using Zemlin-tableau method[90]. In the image corrector, the aberrations are measured using diffractograms of an amorphous area recorded at different tilt angles. The probe correctors use similar principle to measure the aberrations but the Zemlin-tablau is built using images over- and under-focus for different tilts and compare them with the image close to focus. The CEOS correctors used in the ARM200 microscope used in this work employ a symmetric hexapole doublet to compensate for the spherical aberration of the objective lens in TEM. The same principle and a similar design are used for the CEOS hexapole STEM corrector. The first hexapole of the corrector deforms the beam which is projected into a second hexapole that compensates for this deformation leaving only a higher order effect, acting like a negative C_s and compensating the positive C_s in the objective lens.

The next section describes the main imaging technique used in a double-corrected ARM200 to characterise the 2D-TMD layers in this research.

2.3.3 Annular dark field-STEM images

Probe corrected electron microscopes can generate focused spots with a diameter smaller than 0.1 nm. Additionally, the stable electronics make positioning of the probe to pm accuracy possible, allowing atomically resolved images. The direct transmitted electrons are collected using a BF detector. A concentric ADF detector (Figure 2.12) is normally used to collect the scattered electrons. ADF detectors collect electrons transmitted through the specimen and scattered within a certain angular range, determined by the inner and outer diameters[86]. If the inner angle of the ADF detector is similar to the probe convergence angle, coherent diffracted electron beam can reach the detector contributing to the image contrast[86]. On the other hand, when the inner angle is three or more times larger than the probe convergence angle, the scattered electrons reaching the detectors correspond to high-angle Rutherford scattered electrons from the nuclei[82]. Normally the inner radius of the detector is chosen so no direct transmitted electrons are detected. Thus, in each point the ADF image is proportional to the total number or incoherently scattered electrons reaching the detector[82]. Therefore, in this last case the ADF image contains strong atomic-number contrast and not much diffraction contrast (most of the diffracted electrons have a scattering angle less than inner angle and pass through the central hole in the detector). Therefore, the images contain composition

information, since the cross section for Rutherford scattering is a strong function of the atomic number (Z) and the thickness of the specimen[82]. The intensity in the ADF-STEM images is proportional to Z^2. Thus, the contrast allows a clearer visualization of the different elements in the structure, in particular heavier elements.

The atomic-resolution STEM images acquired in this Ph.D. used a double aberration-corrected JEOL ARM-200F operating at 200 kV and 80kV. ADF images were formed using a collection angle of 45-180 mrad and 20-100 mrad for each voltage respectively. The convergence semiangle used was ~25 mrad and ~30 mrad at those voltages.

So far, only elastic scattering processes have been mentioned. The inelastic scattering of electrons transfer energy to the sample and different signals can be produced.

2.3.4 Electron energy loss spectroscopy (EELS)

Electron energy loss spectroscopy (EELS) is based on the distribution of scattered electrons with a given energy loss. It is a powerful technique for determining the composition and bonding in the material, a good approach for the microanalysis of light elements. Additionally, a range of scattering mechanisms can be evaluated, such as plasmon or phonon scattering. EEL spectrometers are generally post column filters, which analyse the electron energy with a series of dispersing elements, and generating the spectrum. The change in energy ranges from 0 eV to a few keV. The EEL spectrometers use a magnetic field to disperse electrons with different energies and then a sequence of optical elements to guide these electrons to a detector, comprising a scintillator and a CCD camera. This then records a spectrum of intensity against energy loss.

An EELS spectrum (Figure 2.16) is composed of three regions: the zero-loss peak (ZLP), the low-loss (LL) and the core-loss (CL) region[82].

The zero-loss peak (ZLP) is the peak located at 0 eV, and corresponds to the transmitted and direct electrons, with either zero or unmeasurable energy loss[82]. In very thin specimen, the most electrons are elastically scattered, so the ZLP is usually the most intense peak in the EELS spectrum[82]. The thickness of the specimen can be estimated from the ratio between the integrated area under the LL region and the ZLP.
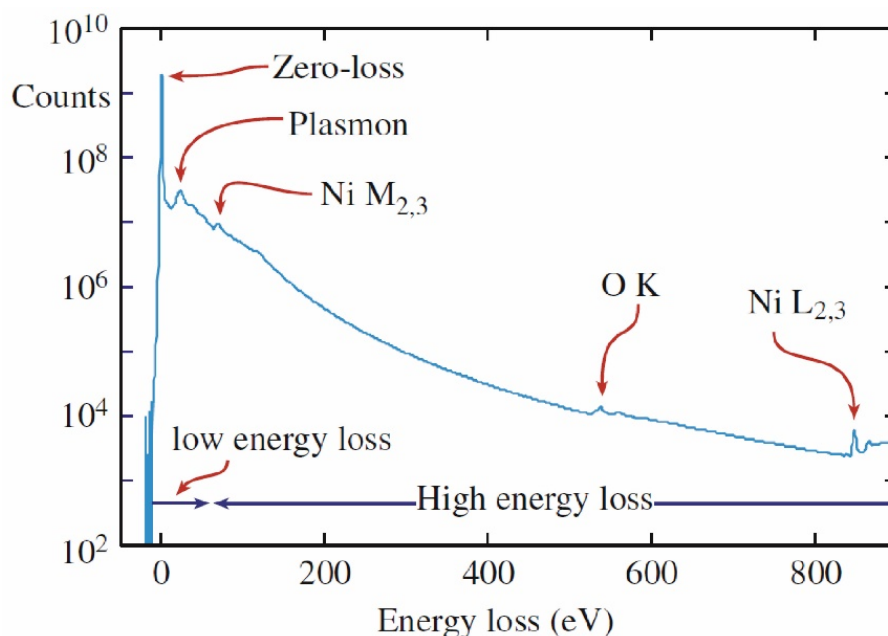
Figure 2.16. An electron energy loss spectroscopy (EELS) spectrum in logarithmic intensity mode. Adapted from Ref. 82.

LL region (<50eV) contains information about the interactions between the incident electron beam and the solid[82]. Excitons and plasmons dominated this area of the spectrum. The LL contains information about the excitation of the VB electrons (which can be thought of as a set of coupled oscillators), the inter- and intra-band transitions, phonon, excitons and the plasmon excitations[82]. Thus, after the ZLP, the major feature in this region of the spectrum corresponds to the bulk plasmon, a collective oscillation of the loosely bound electrons, which runs as a longitudinal wave through the volume of the crystal with a characteristic frequency[82]. The energy distribution in this area is closely related to the specimen dielectric function of the material[82]. In the case of 2D materials, this is very important, since the excitations can differ strongly from those in the bulk counterparts. Thus, there are reports on using low-loss EELS spectrum with a monochromator to characterise the optical signals (*e.g.* PL peaks) of 2D materials in range of 1-3 eV[91,92] and its difference with the bulk material. Additionally, the fine structure of the ionization edge, can provide information of the density of unoccupied states in the CB. Thus, details of the bonding, coordination and density of states can be obtained when the fine structure is analysed[82].

The EELS spectra analysed in this PhD were acquired in a Nion UltraSTEM100 working at 60kV (Trinity College Dublin, Ireland). A 30 mrad convergence angle, a 48 mrad collection aperture, an energy dispersion of 50 meV/pixel were the acquisition parameters.

2.3.5 Radiation damage

Electron irradiation damage can be categorized in two types according to the type of electron scattering[93].

(i) During elastic scattering processes, the incident electrons are electrostatically deflected by the Coulomb field of the atomic nucleus[93]. Under certain circumstances, this can result in atomic displacements and/or electron beam sputtering[93].

(ii) The interaction of the incident electrons with the atomic electrons surrounding the nucleus originate inelastic scattering[93]. The inelastic scattering can cause secondary electrons, emissions of X-rays and the EELS spectra. The process can result structure change, mass loss and hydrocarbon contaminations[93].

2.3.5.1 Atomic displacement (knock-on damage)

For elastic scattering, the energy and momentum are conserved, so the amount of energy E transferred by the electron is[93]

$$E = E_{max}sin^2(\theta/2) \, , \qquad\qquad 2.\,13$$

where θ is the angle that the electron is deflected in the field of a single atomic nucleus, and E_{max} can be expressed as[93]

$$E_{max} = E_0(1.02 + \frac{E_0}{10^6})/(465.7A) \, , \qquad\qquad 2.\,14$$

where E_0, the energy of the incident electron in eV and A is the atomic mass number[93]. When θ is small, the term sin^2 in equation 2.13 is small hence the transferred energy is almost negligible ($E \ll 1$ eV)[93]. However, considering extreme conditions, $\theta = 180°$, the transferred energy is E_{max}. This value increases with the incident energy E_0 for low the mass number. If the transferred energy is larger than displacement energy, $E \gg E_d$, the

electrons with high angle elastic scattering can knock-on displace the atoms, hence resulting in defects in the crystal structure[93].

The displacement energy E_d is a property of the material related with the bond strength and atomic mass and crystal structure[93]. In practice, E_d values can be determined experimentally, then the corresponding threshold values for the incident beam energy E_0 can be calculated by equation 2.13 and 2.14[93]. The only way to avoid atomic displacement is to use electron beams with lower energy than the threshold value for the material to analyse[93,94].

2.3.5.2 Electron beam sputtering

The energy required for atom displacements at the surface of the material if high angle elastic scattering occurs is much lower than that in bulk[93]. The surface atomic displacement is similar to sputtering, i.e. surface atoms displaced by an ion beam[93]. Since the momentum transfer in high angle collisions occurs mainly in the incident direction, sputtering results on the beam exit surface[93]. According to equation 2.14, sputtering is more likely to involve atoms with low atomic number, so limiting the radiation dose, or protecting the specimen beam-exit surface with a heavy element can reduce the sputtering process[82,93,94].

2.3.5.3 Electron beam heating

Inelastic scattering involves the incident electrons and the atomic electrons, with similar mass. Therefore, appreciable energy can be transferred in the process. Most of this energy ends up as heat within the specimen, giving rise to a local temperature[93]. If the thermal conduction in the surrounding material is poor, local heating can produce broken bonds, atom diffusion, and loss of volatile materials[93].

2.3.5.4 Electrostatic charging

There are several sources of the charges, *e.g.* the primary electrons from the incident electrons trapped in the materials, high-angle scattered electrons and emitted secondary electrons from inelastic scattering processes[93]. When the electron beam hits the surface of an electrically insulating specimen, the specimen may absorb more electrons than ejected[93,94]. Thus, if the charge dissipation is insufficient, a localized current can occur.

Since insulating materials do not provide a path to ground for the current, they may experience electrostatic charging when exposed to the electron probe, where a localized net build-up of static electric charge is generated[93,94]. If the local charge in the specimen is negative, it will repel/deflect the incident electrons resulting in image distortion and instabilities[82].

2.3.5.5 Radiolysis effect (ionisation damage)

Radiolysis damage is a type of ionisation damage resulting from inelastic scattering. The energy lost from the incident beam can be transferred to the atoms. Thus, single or collective atomic electron transitions can occur, being different for metals, semiconductors and insulators[93]. For metal, the CB electrons are excited to empty states above the Fermi level, leaving a vacancy in the VB that will be filled rapidly because of the high density of conduction electrons[94]. Meanwhile, the de-excitation process releases energy, creating phonons and leading to thermal vibrations of atomic nuclei, therefore a rise in temperature instead of permanent atomic displacements[94].

In contrast, for an insulating or semiconducting specimen, electrons in the VB are excited into CB, generating an electron-hole pair[94]. Since the electron concentration in the CB is low, it takes longer to fill the holes in the VB. This implies that during this period, the electron wave functions may change and some of the excitation energy is stored as potential energy resulting in changes in the interatomic bonding (broken bonds)[94]. Moreover, when an inner shell electron is excited via an inelastic scattering process, a VB electron fills the core hole, so an Auger electron can be generated resulting in the creation of secondary electrons that can break bonds and further damage the specimen[94].

2.4 Introduction to angle-resolved photoemission spectroscopy (ARPES)

2.4.1 Fundamentals of ARPES

Angle-resolved photoemission spectroscopy (ARPES) is a powerful technique for probing the electronic structure of solids[95]. A typical ARPES setup is shown schematically in Figure 2.17a[95]. A sample is placed under ultrahigh vacuum and

illuminated by a monochromatic light source. Electrons in the specimen can absorb photons in the incident light, when the photon energy is higher than the work function of the specimen, electrons can be photo-emitted and escape into the vacuum[95]. An electron analyser (spectrometer) is placed next to the sample to collect these electrons (photoelectrons), measuring their kinetic energies and emission angles as shown in Figure 2.17[95].

Conservation of the photo-emitted electron results in the following relation[95,96]

$$E_{kin} = h\nu - \Phi - E_B \,, \qquad\qquad 2.\,15$$

where E_{kin} is the kinetic energy of a photoelectron, $h\nu$ is the energy of the incident photon, Φ is the work function of the material and E_B is the binding energy of the electron in the sample[95,96]. The work function $\Phi = E_{vac} - E_F$, in which E_{vac} is the vacuum level while E_F is the Fermi level, as shown in Figure 2.17b[95,96]. Accordingly, ARPES is mainly used for studying the occupied electronic states below Fermi level[95,96].

During the photoemission process shown in Figure 2.17, along with the energy of the electron, its momentum parallel to the plane of the sample, $\hbar\boldsymbol{k}_\parallel$, is also conserved. This can then be determined from the angle of emission of the electron. For the geometry shown in Figure 2.17a[95,96] this gives

$$\hbar\boldsymbol{k}_\parallel^f = \hbar\boldsymbol{k}_\parallel^i = \sqrt{2mE_{kin}}(sin\theta cos\varphi\widehat{\boldsymbol{k}}_x + sin\theta sin\varphi\widehat{\boldsymbol{k}}_y) \,, \qquad\qquad 2.\,16$$

in which $\hbar\boldsymbol{k}_\parallel^f$ is the parallel components with respect to the sample surface of the momenta of the photoelectron, while $\hbar\boldsymbol{k}_\parallel^i$ is the initial in-plane momentum, θ and φ are the emission angles of the photoelectron, $\hbar$ is the reduced Planck's constant and m is the electron rest mass[95,96].

Due to the broken symmetry at the surface, the momentum perpendicular to the surface ($k_\perp$) is not conversed, so $k_\perp^f \neq k_\perp^i$. Instead the momentum perpendicular to the surface can be found from[95,96]

$$k_\perp^i = \sqrt{2m(E_{kin}cos^2\theta + V_0)}/\hbar \,, \qquad\qquad 2.\,17$$
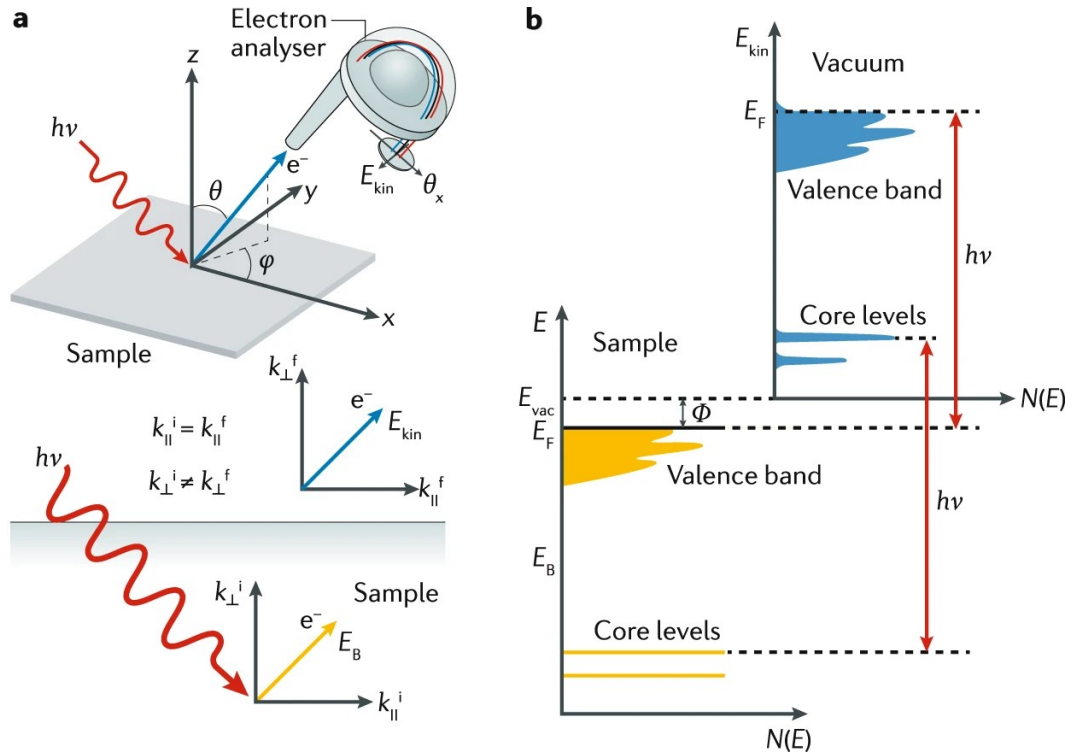
Figure 2.17. Schematic diagrams of a typical angle-resolved photoemission spetroscopy (ARPES) setup. (a) Upper: schematic diagram shows the geometry of the ARPES measurements. Lower: schematic of the wavevectors of the electron in the sample and as it leaves the sample surface. Here $k_{\parallel}$ represents the vector components parallel to the surface and $k_{\perp}$ represents the vector component that is perpendicular to the surface. (b) Energy diagram schematically illustrating the photoemission process. Adapted from Ref. 95.

in which V_0 is a constant called the inner potential. From equation 2.17, measuring at different photon kinetic energies changes E_{kin} for the same E_B, and thus samples different $k_{\perp}^i$. In principle, V_0 can be determined by measuring over a range of photon energies and then fitting the periodicity of the measured band structure along the $k_{\perp}$ direction to the known periodicity of the BZ[95,96].

Photoemission data are usually discussed within the three-step model which divides the photoemission process into three independent and sequential steps: optical excitation of an electron, electron transport to the surface, and emission of the electron into the vacuum[95,96]. The sudden approximation is usually applied; it is assumed that the system does not relax until after the electron has escaped, so the N-particle final state can be

simplified as a combination of the photoelectron and the N-1 particle state[95,96]. In this way, the ARPES photoemission intensity $I(\boldsymbol{k}, E)$ is commonly written as[95,96]

$$I(\boldsymbol{k}, E) = I_0(\boldsymbol{k}, \nu, \boldsymbol{A}) A(\boldsymbol{k}, E) f(E, T) , \qquad \qquad 2.\,18$$

where $A(\boldsymbol{k}, E)$ is the single-particle spectral function and $f(E, T)$ is the Fermi-Dirac distribution[95,96]. $I_0(\boldsymbol{k}, \nu, \boldsymbol{A}) \propto \sum_{f,i} |M_{f,i}^k|^2$, where $M_{f,i}^k = \Phi_f^k | A \cdot P | \Phi_i^k$ is the photoemission matrix element that describes the transition of the initial state Φ_i^k to the final state Φ_f^{k}[95,96].

In practice, the hemispherical analyser usually contains a 2D detector that measures the kinetic energy of photoemitted electrons across a limited range of one angle, e.g. θ in Figure 2.17a, for a specific value of the other angle, φ[95,96]. A three-dimensional dataset of the photoemission intensity as a function of kinetic energy and emission angle, $I(\theta, \varphi, E_{kin})$, is acquired by recording a set of these slices at varying φ. From this the three-dimensional dataset $I(\boldsymbol{k}_\parallel, E_B)$ is determined by interpolation, using Equations 2.15 and 2.16. The Fermi energy is determined by fitting the Fermi-Dirac distribution to the fall in intensity across the Fermi edge for a metallic sample. From the 3D datasets, energy-momentum slices can be extracted along the high-symmetry directions, or constant energy maps across regions of the BZ. The results are ARPES spectra that directly show the band dispersions as a function of energy and momenta within the plane and at the surface of the sample, ideally suited to the measurement of 2D materials.

2.4.2 Key parameters of band structure

Typical ARPES spectra from monolayer, bilayer and multilayer regions of a WSe$_2$ flake are presented in Figure 2.18[97], demonstrating the evolution of the VBM from the $\boldsymbol{\Gamma}$ to the $\boldsymbol{K}$ point as the thickness of WSe$_2$ reduces from bulk to single layer. The SOC splitting of the VB in monolayer is measured to be (500 ± 30) meV from the data in Figure 2.18. Within uncertainty it is the same as that of the bilayer and bulk WSe$_2$[97].

The dispersion of each band can be obtained by extracting energy distribution curves (EDC), $I(E_B)$ for fixed momenta, out of a 3D spectra, fitting the peak positions, and repeating across a range of momenta. From this data, key band parameters can be determined. Around the high-symmetry points, the band dispersions were fit by a
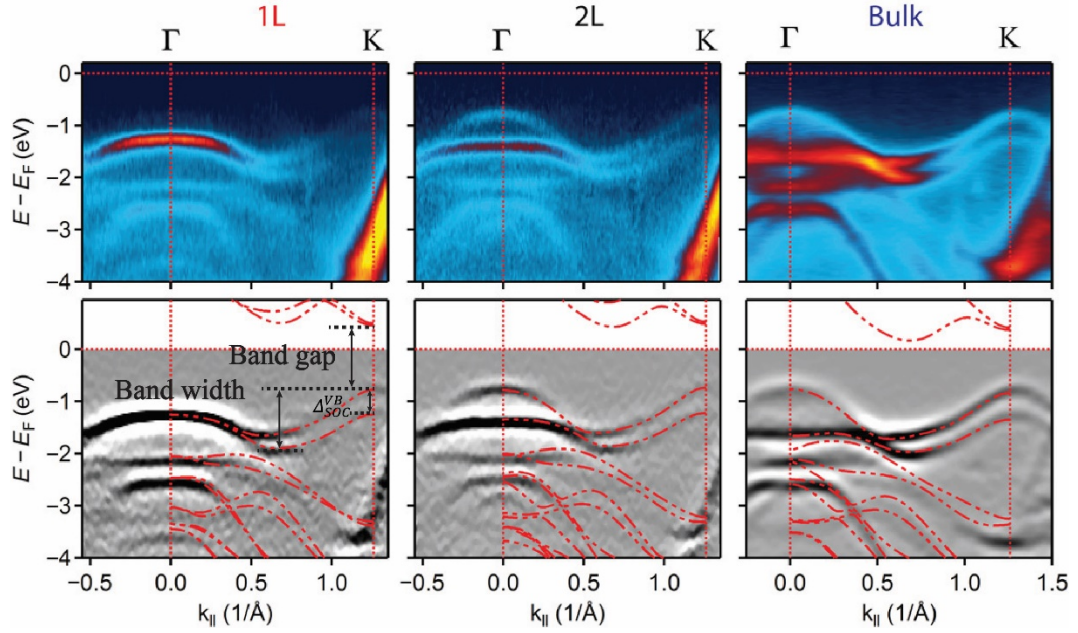
Figure 2.18. Bands structures of WSe$_2$ with different thickness via ARPES. From left to right: band structure of monolayer, bilayer and bulk form WS$_2$ crystals, respectively. Lower is the intensity twice-differential with respect to energy with overlaid DFT calculation. Adapted from Ref. 97.

parabola. The band maxima and minima were then used to determine the VBM, band offsets, band widths, and the spin spliting of the VB at **K** as indicated in Figure 2.18[97]. The curvature of the parabola determines the effective mass, from $E = \frac{\hbar^2 k^2}{2m^{*2}}$ in which m^* is the effective mass.

If the CB is also populated, for example if the material is electron-doped, the band gap of the material can be directly obtained via fitting the energy difference between the CBM and VBM measured from the ARPES spectra.

Chapter 3: Synthesis of TMD Alloys and Hetero-structure Assembly

3.1 Introduction

As introduced in chapter 1, TMD materials show unique electrical and optical properties in their single layer configuration, *e.g.* an indirect to direct band gap transition[29,98] and optically controllable valley polarisation[43,99]. Although many reported TMD-based devices *e.g.* field effect transistors (FET)[23], optoelectronic devices[100], valleytronics[101] *etc.* show high device performance, the tunability for related properties such as band gaps and SOC is limited. As in conventional silicon technology, doping and alloying are widely used to achieve functionality of a semiconducting material[102,103], this can be brought to TMD materials[103]. By substituting or alloying the metals or chalcogens of the TMDs, the materials have additional tunability in band gap[40,56,57] and spin-orbit engineering[40,104,105].

To further investigate how the extra tunability can be achieved, it is essential to develop the techniques for material synthesis and sample fabrication. Among all the synthesis techniques mentioned in Chapter 1, CVD is the most widely used bottom-up approach for TMD alloy growth[19]. However, the CVD-grown alloy monolayers show inhomogeneous atomic distribution, higher concentration at the edges and lower at the centre[60]. This can result in unstable and heterogeneous properties, poorly suited for device applications. Another significant drawback of this technique is that complicated stacks with desired artificial sequences, *e.g.* heterostructure with more than three layers, are hard to prepare via this method. Therefore, we chose to develop CVT, mechanical cleavage and dry transfer for van der Waals stack assembly for this thesis.

Therefore, this chapter will first start with a description of single crystal growth via CVT, followed via a top-down method, mechanical exfoliation, to reduce the bulk crystals to monolayers. Moreover, several experimental techniques have been developed in our laboratory to place the atomic flakes on desired locations in a controlled way in order to achieve the artificial assembly of atomically controlled 2D heterostructures.

It is well-known that the atomic structure has significant influence on the physical properties of atomically thin layers of materials. For example, heterogeneous atomic distribution in CVD-grown TMD alloy flakes can result in the shift of the PL emission peak across the flake[106,107]. Therefore, the visualisation of the atomic structure is essential for the investigation of alloys. However, knock-on damage occurs rapidly once these atomically thin layers are exposed to the high-energy electron beam in an electron microscope. Here, to mitigate this damage, a novel procedure for TEM characterisation has been developed.

3.2 Crystals synthesis

3.2.1 Compounds preparation

As introduced in section 2.1.1, element powders of metals (M = Mo, W and Nb, with purity 99.99%) and chalcogens (X = S, Se and Te, with purity 99.99%) were stoichiometrically added to an ampoule with inner diameter 1.2 cm. This ampoule was pumped down to a pressure of 10^{-5} torr and sealed. Before placing the ampoule in a box furnace, as shown in Figure 2.3, the ampoule was shaken for several hours to mix the powder uniformly. There are three heating cycles for the TMD compound preparation, as shown in Figure 3.1. During the first cycle, the furnace temperature was ramped to 150°C at a rate of 15°C/h and maintained at this temperature for 1 hour. After this time, the furnace temperature was similarly ramped to 300°C, followed by 1 hour at 300°C, and then to 450°C at the same rate, with a final dwelled at that temperature for 72 hours as shown in Figure 3.1a. In the end, the furnace was allowed to cool to room temperature[62].

The temperature profile of the second cycle was similar to the first, heating by 150°C at 15°C/h then dwelling for 1 hour, except that the furnace temperature reached 750°C, Figure 3.1b[62]. For the final cycle, Figure 3.1c, the temperature profile was initially similar, but once the furnace reached 750°C, a dwell of 10 hours was used as a precaution to avoid explosion. Next, the temperature was further increased to 1000°C and dwelled for 72

hours, before allowing to cool down to room temperature[62]. Figure 3.2 shows photographs of MoS_2 compound preparation before and after each heating cycle.
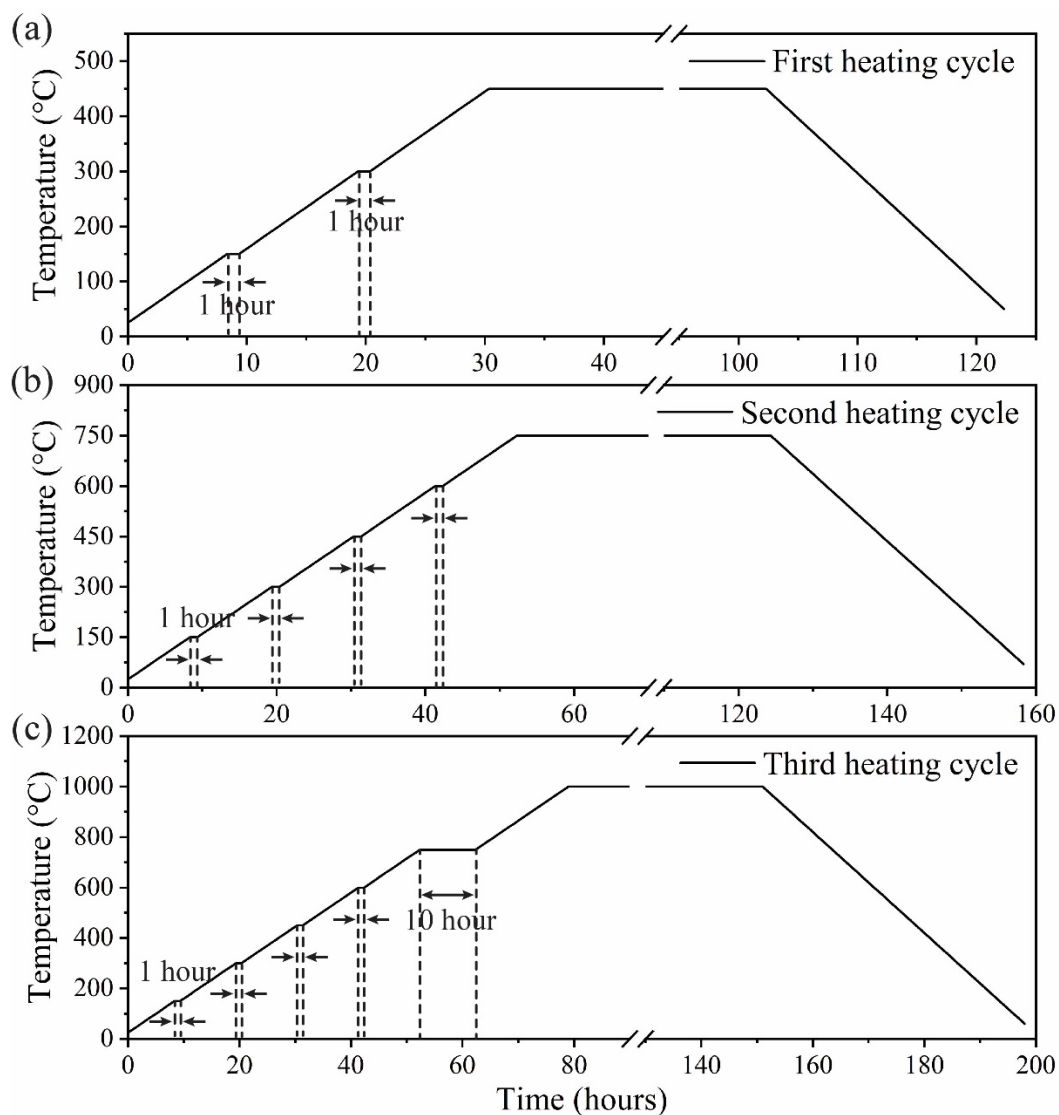
Figure 3.1. Heat profiles for transition metal dichalcogenide (TMD) powder preparation. Heating profiles of (a) first heating cycle dwelling at 450°C, (b) Second heating cycle heating to 750°C and (c) third heating cycle with dwell temperature at 1000°C.
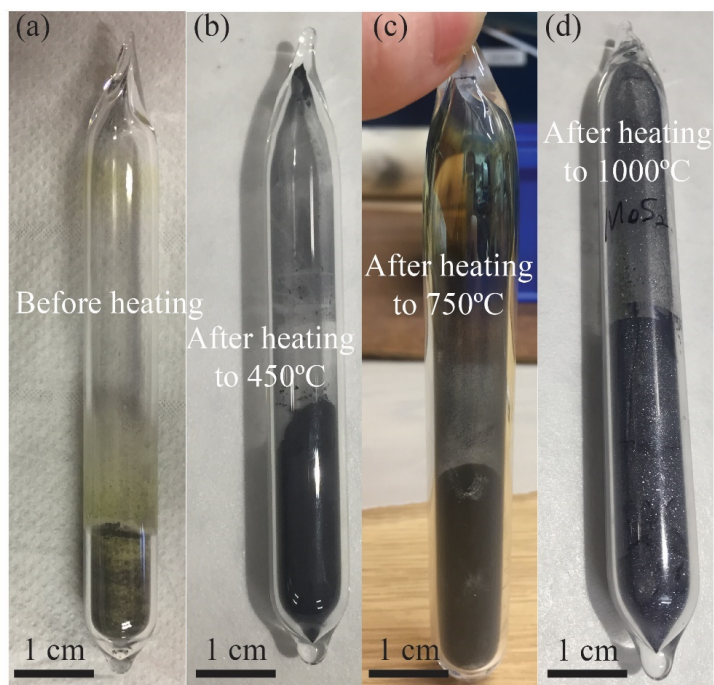
Figure 3.2. Photos of compound preparation in an ampoule before and after heating. (a) Mixture of element powder, sulphur and molybdenum. (b) Products of first heating cycle with maximum temperature at 450 °C. (c) Compounds of second heating cycle dwelling temperature at 750 °C. (d) Compounds of final heating cycle reaching temperature 1000°C.

The ampoule was carefully broken and the synthesised powder was collected and characterised by X-ray diffraction (XRD). Figure 3.3 shows powder XRD patterns of $Mo_{0.29}W_{0.71}S_2$ and WS_2 compounds, with predicted diffraction patterns for 2H and 3R WS_2 single crystals shown at the bottom[108,109]. The first observation from these X-ray scattering patterns is that the powder has already formed compounds and crystallites. Secondly, the phase of these compounds can be determined directly via comparing the X-ray scatterings (Figure 3.3a and 3.3b) with the predicted patterns (lower in Figure 3.3b). The matched peaks are labelled by the purple triangle symbols: both compounds can be identified as 2H polytypes. Moreover, the crystal structure of $Mo_{0.29}W_{0.71}S_2$ compounds are closer to 2H-WS_2 than to 2H-MoS_2.

The peak profiles in Figure 3.3 are much broader than those from single crystal samples (see Figure 4.4 in Chapter 4). The peak profiles can be influenced by many factors such as instrument resolution, crystallite size, micro-strain, solid solution inhomogeneity and temperature[110–112]. As these powder diffraction patterns were
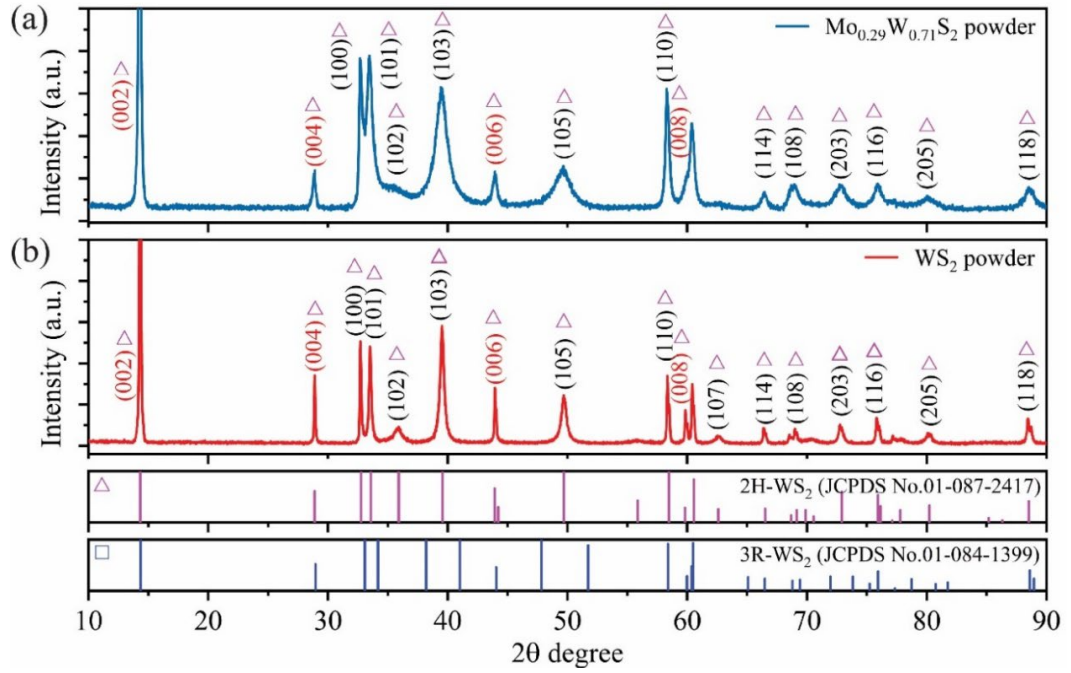
Figure 3.3. X-ray diffraction patterns of $Mo_{1-x}W_xS_2$ compounds in powder form before CVT. (a) X-ray powder diffraction pattern of $Mo_{0.28}W_{0.72}S_2$. (b) X-ray powder diffraction pattern of pure WS_2. Lower panels show predicted diffraction patterns for the common 2H and 3R polytypes of single crystal WS_2[108,109]. The symbols with different colours and shapes mark the peaks matched with those in the expected diffraction patterns, as labelled.

performed in the same instruments under the same conditions, the peak width broadening in Figure 3.3 is mainly attributed to the crystallite size, indicating the crystallites are small. Assuming that the dominant contribution to the peak width is the crystallite size, the characteristic crystallite size can be estimated from the Scherrer equation[110,111]

$$B(2\theta) = \frac{K\lambda}{L\cos\theta},$$
$$3.1$$

in which B is the peak width, K is the Scherrer constant, λ is the wavelength of the X-ray source, θ is the Bragg angle and L is the average crystallite size perpendicular to the reflecting planes[110,111]. Hence, the crystallite size can be simply estimated from the XRD patterns and is inversely proportional to the peak width. The peaks in Figure 3.3a are wider than those in Figure 3.3b, but also there is variation in peak widths within each spectrum *e.g.* the peaks of planes (100), (101) and (102) *etc.* This can be attributed to the solid solution inhomogeneity leading to variation in composition that creates a distribution of d-spacing for a crystallographic plane[113]. However, taking a typical peak

width, we can estimate a crystallite size around 37 nm and 77 nm in $Mo_{0.29}W_{0.71}S_2$ and WS_2 powders, respectively.

3.2.2 Chemical vapor transport (CVT)
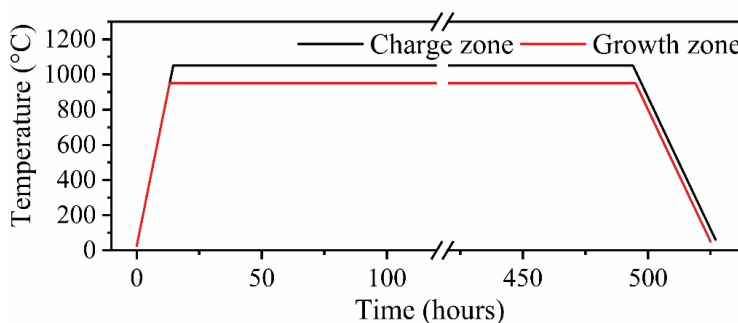
Figure 3.4. Heat profiles for the charge and growth zone of the box furnace during CVT. The black solid line represents the temperature of the charge zone against time, while the red line is for that of the growth zone.

The synthesised compounds (typically between 2 and 3 grammes) and transport agent (iodine crystals, the amount of which depended on the volume of the sealed quartz tube) were added to a new quartz tube with larger inner diameter (typically around 1.6 cm). The tube was evacuated to 10^{-6} mbar whilst being cooled by ice to stabilise the iodine, and then sealed. The length of the tube, around 30 cm, defines the length of travel of the vapor phases. For crystal growth, a tube furnace with three heat zones was used, as shown schematically in Figure 2.4b. The temperatures of the source/charge and growth zones were ramped at a rate of $70°C/h$ to $1050°C$ and $950°C$, respectively. A typical growth time was around 20 days after achieving the desired temperature, but it varied for specific materials. Finally, the furnace was air cooled to room temperature over around one day.

3.2.2.1 Synthesis of $Mo_{1-x}W_xS_2$ single crystals

For a transport system with $MS_2/I_2/H_2O$ (M = Mo or W), the migration of MS_2 can be achieved via vapor phases of MO_2I_2 and S_2 in the reversible reaction[62,63]

$$MS_2 \text{ (s)} + 2H_2O \text{ (g)} + 3I_2 \text{ (s)} \rightleftharpoons MO_2I_2 \text{ (g)} + 4HI \text{ (g)} + S_2 \text{ (g)} .$$
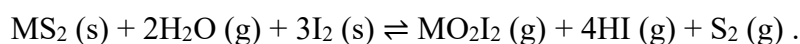
The hot vapor phases form at the source zone, then diffuse towards the cooler end of the quartz tube. When they hit the glass wall at the cooler end (growth zone), the MS_2 crystals start to nucleate and grow. The conditions during growth, such as temperature (T + ΔT) at the source zone, temperature T at the growth zone, temperature gradient (ΔT) over the tube as schematically shown in Figure 2.2a (the temperature does not linearly decrease along the tube), flux of the transport agent, the growth time and the amount of source materials *etc*., lead to different final products.

For example, the size of $Mo_{0.5}W_{0.5}S_2$ single crystals are around 1-2 mm when the growth temperature is 900°C in Figure 3.5b, however they can achieve 1-2 cm when the
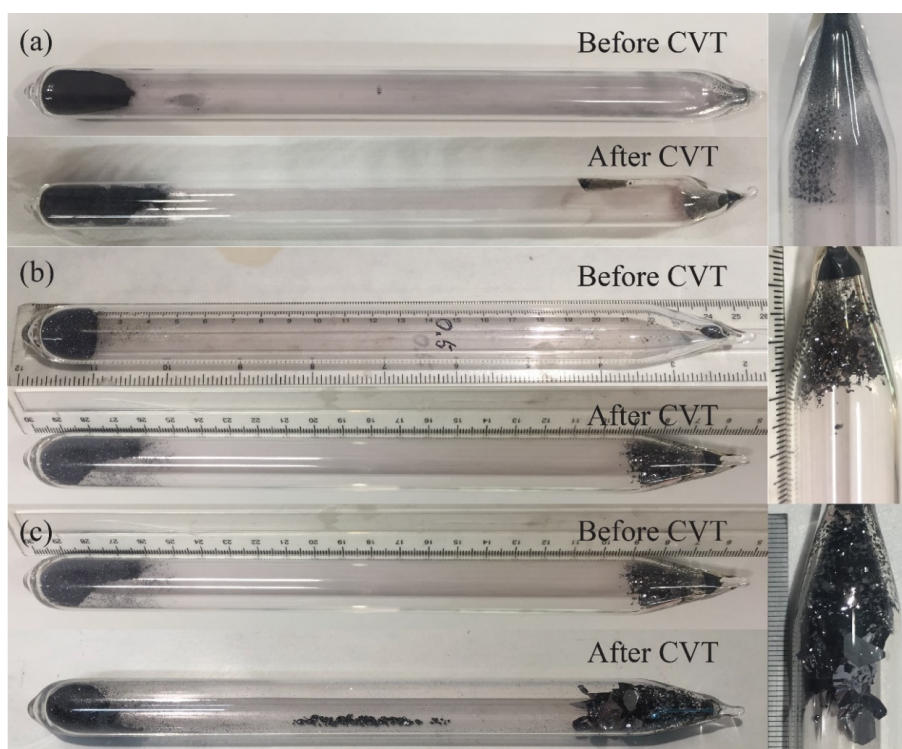
Figure 3.5. Influence of growth parameters on the single crystal products. (a) Mixture of $Mo_{0.5}W_{0.5}S_2$ compounds and I_2 crystals before and after CVT. The length of tube is around 30 cm. The temperature of the source and growth zone were set to 1030 and 980°C, respectively. Magnified image of its growth zone is presented at right. (b) A new quartz tube with $Mo_{0.5}W_{0.5}S_2$ compounds and I_2 crystals before and after CVT. The length of this tube is around 25 cm, with source and growth temperatures at 1050 and 900°C, respectively. (c) The same quartz tube in 5b before and after a second CVT cycle, the source and growth temperature were 1050 and 950°C, respectively.

growth temperature goes to 950°C as shown in Figure 3.5c. Meanwhile the length of the quartz tube also affects the final products, since this will influence the diffusion length of the vapour phases (WO_2I_2, HI and S_2) and the temperature distribution along the tube. For instance, the tube is around 29 cm in Figure 3.5a and around 25cm in Figure 3.5b, but under the same growth conditions small $Mo_{0.5}W_{0.5}S_2$ single crystals can only be obtained in the smaller tube (Figure 3.5b).

CVT conditions were determined for the growth of a series of $Mo_{1-x}W_xS_2$ alloys, as summarised in Table 3.1.

3.2.2.2 Synthesis of $Nb_{1-x}W_xS_2$ and $Nb_{1-x}W_xSe_2$ single crystals

The growth parameters of Nb-containing WS_2 alloys, *e.g.* the growth time and the length of tubes, were similar to those of the $Mo_{1-x}W_xS_2$ alloys. However, the temperature of source and growth zone were different. The source temperature was set to 1050°C while the growth temperature was set to 930°C for $Nb_{1-x}W_xS_2$ alloys[114,115]. The CVT parameters are summarised in Table 3.2. Three compositions of $Nb_{1-x}W_xS_2$ powders were made, but only $Nb_{0.1}W_{0.9}S_2$ single crystals was successfully obtained by CVT.

For Nb-containing WSe_2 single crystals, the growth parameters were close to those used for pure WSe_2 synthesis. The source temperature was set to 1000°C while the growth temperature was 850°C[62,116,117]. The flux of transport agent for the selenides was slightly lower than for the sulphides due to the different chemical reactions involved. The growth conditions for these samples are summarised in Table 3.2.

The reversible reaction of a selenide is[116,117]

$$2WSe_2 \text{ (s)} + 3I_2 \text{ (g)} \rightleftharpoons 2WI_3 \text{ (g)} + 2Se_2 \text{ (g)} .$$
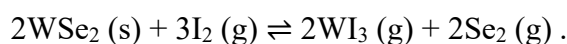
Similarly, to the sulphides, the hot vapor phases formed at the source then diffuse towards the growth zone. When the vapors meet the colder glass wall, crystals start to nucleate and grow.

Table 3.1. CVT growth conditions for $Mo_{1-x}W_xS_2$ single crystals.

Compositions	Source temperature T_1 (°C)	Growth temperature T_2 (°C)	Growth time (days)	Flux of agent (g/cm³)	Length of quartz tube (cm)	Typical crystal size (mm)
MoS_2	1050	950	20	10	28 - 29	0.5 - 1
$Mo_{0.82}W_{0.18}S_2$	1050	950	20	5	27 - 28	1 - 2
$Mo_{0.63}W_{0.37}S_2$	1050	950	20	10	28 - 29	2 - 3
$Mo_{0.51}W_{0.49}S_2$	1050	900	21	8	25	3 - 4
	1050	950	21	8	25	10 - 15
$Mo_{0.31}W_{0.69}S_2$	1050	950	20	5	27 - 28	1 - 3
$Mo_{0.28}W_{0.72}S_2$	1050	950	20	10	28 - 29	10 - 20
$Mo_{0.14}W_{0.86}S_2$	1050	950	20	5	27 - 28	0.5 - 1
WS_2	1050	950	28	10	29	0.5 - 1
	1050	950	20	10	27 - 28	2 - 3

Table 3.2. CVT growth conditions for $Nb_{1-x}W_xS_2$ and $Nb_{1-x}W_xSe_2$ single crystals.

Compositions	Source temperature T_1 (°C)	Growth temperature T_2 (°C)	Growth time (days)	Flux of agent (g/cm³)	Length of quartz tube (cm)	Typical crystal size (mm)
$Nb_{0.1}W_{0.9}S_2$	1050	930	20	8	27	0.5 - 1
$Nb_{0.17}W_{0.83}Se_2$	1000	830	20	5	27	3 - 4

Table 3.3. CVT growth conditions for other single crystal samples.

Compositions	Source temperature T_1 (°C)	Growth temperature T_2 (°C)	Growth time (days)	Flux of agent (g/cm³)	Length of quartz tube (cm)	Typical crystal size (mm)
Re-MoS$_2$	1030	950	20	8	28	3 - 4
WSe$_2$	1000	850	14	5	27	3 - 4
WSSe	1000	900	20	5	28	2 - 3

3.2.2.3 Synthesis of other single crystals (Re-MoS$_2$ and WSe$_2$)

As introduced in Chapter 2, two techniques, CVD and CVT, are widely used in synthesis of doped or alloyed layered TMD (MX$_2$) materials[11]. However, the composition of CVD-grown MX$_2$ monolayer alloys can be inhomogeneous. Moreover, the composition of the as-grown monolayers is not always directly defined by the stoichiometry of the source material[59,106]. Therefore, compared to CVD, CVT can be a better choice for controllable synthesis for material doping and alloying.

3.3 Mechanical exfoliation

Single crystals were flatly and gently placed on a piece of scotch tape. The tape was fixed on a stage with the sticky side face up, a new tape was put on it gently, then this tape was split rapidly at a low angle. Normally, the crystals on the fixed tape were thicker, thus the other tape was folded several times to split and thin down the crystals. After that, the tape was stuck to a clean SiO$_2$/Si wafer, pressing gently to remove bubbles between the tape and wafer. It was noted that the tape should be peeled off at a low angle and rapidly. The most important step was to then scan the whole wafer and identify thin flakes through their contrast in the optical microscope. For this, the thickness of the oxide layer is important[69]. For most of the work reported in this thesis, 100 mm p-doped Si wafers with resistivity of 1-10 Ohm.cm, thickness of 525 µm, single side polished and thermal oxide of thickness 300 nm were used, purchased from IDB Technologies.

This form of mechanical exfoliation was first used to exfoliate bulk graphite onto SiO$_2$/Si wafers, making their single-layer form visible[69]. Although many techniques, top-down methods *e.g.* electrochemical exfoliation, bottom-up methods *e.g.* CVD and atomic layer deposition (ALD) *etc.*, have been developed to synthesise monolayer materials, mechanical exfoliation is still the first-choice technique for assembling high quality stacks[5,18]. Hence, this technique has been improved/developed later by optimising the temperature at which the exfoliation is made and the holding time for the tape on the wafers[71].

3.3.1 SiO$_2$ substrate

After the tape was pressed onto a SiO$_2$/Si wafer, the best exfoliation condition found for graphite was to place the wafer on a hotplate at 100°C for 3 minutes[71]. To optimise the exfoliation conditions for other 2D materials, such as hBN, MS$_2$ and MSe$_2$ (M = Mo, W and Nb), many experiments were performed, changing the exfoliation temperature and the holding time. The parameters yielding the best samples are listed in Table 3.4.
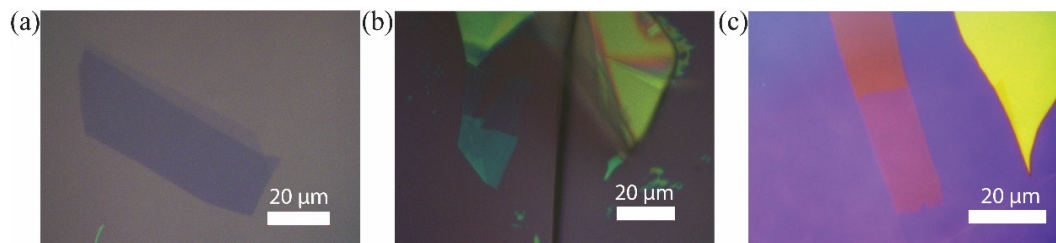
Figure 3.6. Optical images showing exfoliated flakes of different 2D materials on SiO$_2$ substrates: (a) graphene, (b) hBN and (c) Mo$_{0.5}$W$_{0.5}$S$_2$.

Figure 3.6 shows examples of typical graphene, hBN and Mo$_{0.5}$W$_{0.5}$S$_2$ flakes found under the optimised exfoliated conditions.

Table 3.4. Optimised mechanical exfoliation conditions for various 2D materials, on SiO$_2$ wafers.

Materials	Temperature (°C)	Time (minutes)
hBN	100	5 minutes
Graphene	100	3 minutes
MX$_2$ (X = S)	130	2.5 minutes
MX$_2$ (X = Se)	100	2 minutes
WSSe	120	3 minutes

3.3.2 Other substrates

For exfoliating TMD crystals on a CVD-grown graphene on a copper foil, the temperature of the hotplate was set to 130°C and the holding time to 2.5 minutes. After cleaving the tape at a low angle, monolayer TMD flakes could easily be found on the graphene/copper foil via their optical contrast, as shown in Figure 3.7a.

For PMMA and polyvinyl alcohol (PVA) coated Si wafers, the exfoliation procedure was slightly different. The PMMA/PVA/Si wafer was placed on a hotplate with temperature set to 130°C. After the temperature of the wafer reached 130°C, it was moved to a stage then the tape with thin crystals was pressed on the wafer immediately, holding for one minute. As before, the tape was cleaved at a low angle and monolayer TMD flakes could be found by optical microscopy as shown in Figure 3.7b.

3.4 Van der Waals heterostructures assembly

As described in Chapter 2, there are two main methods widely used in van der Waals stack assembly, pick-and-place (PDMS) transfer and PMMA dry transfer[18,118]. In our laboratory, a transfer system (as shown in Figure 3.8) has been built and developed for both of these two techniques.
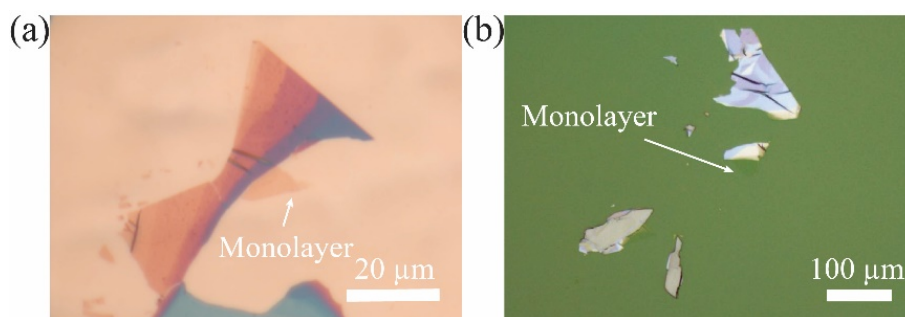
Figure 3.7. Optical images of exfoliated TMD flake on different substrates: (a) on CVD-grown graphene and (b) on PMMA/PVA coated Si wafer as substrates.

There are three main parts to the system: an optical microscope, a sample stage and a transfer arm. The sample stage connects to the optical microscopy and is rotatable. Samples are fixed in place using a vacuum chuck whose temperature can be accurately controlled. The sample stage moves in both X and Y axes (horizontally), while the optical objective can move in the Z axis to adjust the focal plane. The transfer arm is mounted on an XYZ micromanipulator, so the stamps/plectrums can be moved accurately (better than 1 μm) in the X, Y and Z axis, even tilting in the XZ-plane, once they are mounted on the transfer arm.
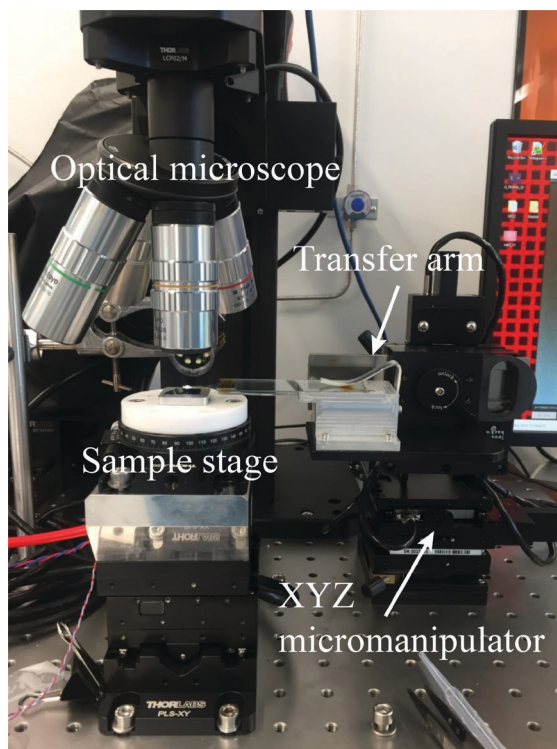
Figure 3.8. Photo of the dry transfer system in the laboratory at the University of Warwick for pick-and-place (PDMS) and PMMA transfer techniques.

3.4.1 Pick-and-place transfer

Prior to the pick-and-place procedure, it is essential to make a good PDMS stamp. The PDMS stamp is a stack of glass slide/ double-sided sticky tape/ PDMS/ polypropylene carbonate (PPC) film/ Scotch tape.

There are two steps for PDMS fabrication. The PDMS base and its curing agent (purchased from Sigma Aldrich) are first mixed in the volume ratio 10:1. The PDMS is poured into a petri dish and dried by heating in a vacuum oven at 100°C for 2 hours. Then the cured PDMS is cut into small discs around 5 mm in diameter and 1 mm in thickness. To aid with smooth peeling onto and away from the substrate, the top surface of the PDMS should be a concave dome. To form this, a droplet of PDMS is placed on a cured PDMS disc and cured upside down under the same conditions. Since they are the same material the droplet spreads on the disc. The balance of surface tension and gravity forms a dome shape on the PDMS during the curing procedure.

A piece of double-sided sticky tape is placed on one end of a glass slide and a PDMS dome is positioned in the middle of the tape. A hole (5 mm) is punched in the middle of a piece of scotch tape, a PPC film (8% weight percentage PPC dissolved in chloroform) is stuck down onto the tape. This PPC film plays an important role during pick-up. The PDMS dome is coated by the PPC film, slightly stretched. Therefore, the final structure of the stamp is as schematically shown in Figure 10: the dome area is transparent so that flakes can be seen through it.

The procedure of pick-and-place transfer is illustrated in Figure 3.9, with an example at the side of the figure. A SiO_2/Si wafer with exfoliated graphene is placed on the temperature-controlled vacuum stage (Figure 3.9a). The sample stage is first set to 80°C, a clean area of the wafer is found and aligned to the centre of the PDMS stamp. To test, the stamp is first lowered via the z-axis micromanipulator of the transfer arm until a touching area can be observed via the optical microscope, then lifted. When no bubbles form between the PDMS and PPC film, and no damage is observed on the PPC film, the stamp is ready for pick-up. The targeted graphene is then aligned to the centre area of the stamp and the stage temperature set to 100°C. The procedure is the same, the stamp is brought down to touch the graphene flake then raised upwards rapidly; the graphene is picked-up from its SiO_2/Si wafer and adheres to the PDMS stamp.

Next, the picked-up flake is aligned to a second layer and the sample plate is set to 130°C, as shown in Figure 3.9c. The targeted TMD flake can be picked up by the graphene and PPC film via the same operation. The example shown here is to make a van der Waals stack in a sequence of partial coverage graphene/TMD flake/hBN. For more complicated stack assembly, the procedure can be repeated to stack more layers. However, the temperature of the sample plate may need to be varied from 100 to 130°C depending on the pick-up materials. Finally, the assembled stacks can be placed on many substrates, e.g. SiO_2/Si wafer with metal coatings, deposition electrodes or exfoliated flakes on top, depending on the sample requirements. The example shown here in Figure 3.9e is to put the stack on a target hBN on SiO_2/Si wafer.

(a) Glass slide
Double-sided sticky tape
PC film
Scotch tape

PDMS stamp

Exfoliated graphene
SiO₂ wafer

Sample stage

Exfoliated graphene flake
Graphite
200μm

Schematic side view of a dry transfer system with a PDMS stamp. The sample stage is heated to 90ºC. An optical image at right shows exfoliated flakes on a SiO₂ wafer.

(b) Graphene
TMD flake

Exfoliated TMD flake
Bilayer
Monolayer
40μm

Alignment of the graphene flake on the PDMS stamp with a TMD flake. The optical image below shows the targeted TMD flake.

(c) Bilayer
Graphite
Monolayer
40μm

Picking up the TMD layer. The optical image shows the resultant graphite / TMD stack.

Figure 3.9. Schematic diagrams showing, step-by-step, the pick-and-place (PDMS) transfer. (a) Pick-up of the first layer. (b) Alignment of the first layer with the second layer. (c) Approach and contact with the second layer and SiO$_2$/Si wafer. (d) Alignment of the top two layers with the bottom layer. (e) Approach of the stamp to complete the heterostructure. (f) Deposition of the structure on the wafer. Optical images are shown as examples at each stage of the fabrication of a van der Waals stack by this hot pick-and-place method.

After aligning the stack to the new hBN layer, the stamp is brought down to contact with the wafer, then the stage temperature is set to 175°C for 5 minutes to melt the PPC film. Afterwards, the transfer arm is lifted immediately; the centre area of the PPC film will be teared and left on the wafer as shown in Figure 3.9f.

Subsequently, the PPC film can be dissolved in a chloroform solution at 90°C for 30 minutes. Then placed in acetone to wash away the chloroform and finally rinsed in iso-propyl alcohol before drying. To remove any remaining polymer residue, the sample can be placed in an annealing furnace; normally, a temperature of 250°C (sometimes 300°C) at a ramping rate 8°C/min is used, and the sample is annealed for 4 hours under a mild vacuum (about 10 Torr) with a low flow of gas (5% H_2 in Ar).

3.4.2 PMMA Dry transfer

A PVA layer (3% weight percentage 50k PVA dissolved in H_2O, purchased from Sigma Aldrich) was spin coated with a spin speed of 5000 rmp onto a clean piece of Si wafer (around 5 cm × 5 cm). The substrate was then baked at 130°C for 5 minutes immediately after spin-coating. Then a PMMA layer (A8, 8% weight percentage 950k PMMA dissolved in anisole, purchased from Sigma Aldrich) was spin coated onto the PVA coated Si wafer at the same spin speed and again baked at 130°C for 5 minutes. The combined thickness of the PVA and PMMA layer was controlled to be around 400 nm. This PMMA membrane was then attached to a plectrum to be used as a stamp[18,119].

As described in section 3.3.2, TMD crystals were exfoliated onto pieces of PMMA/PVA/Si wafer, as shown in Figure 3.10a. A circle ring scratch, with diameter slightly larger than the circular ring of the plectrum, was drawn using a scalpel that is sharp enough to penetrate the PMMA and PVA layer. Then the wafer was immersed in fresh DI water in a petri dish. The sacrificial PVA layer dissolves in the DI water, after which the PMMA layer floats to the surface of the DI water, as shown schematically in Figure 3.10b. A plectrum was prepared by dipping in PMMA (A4, 4% weight percentage 950K PMMA dissolved in anisole, purchased from Sigma Aldrich) and baking at 130°C for several minutes. After that, the A8 PMMA membrane with target flake was transferred onto the plectrum which was immediately placed on a hot plate and heated at 90°C until the DI water is removed, as shown schematically in Figure 3.10c.

(a) TMD flake
PMMA coating
PVA coating
Si wafer

40 μm

Exfoliate TMD flakes onto PMMA/PVA/Si wafer. An optical image is shown at left, monolayer is almost invisible.

(b) Immerse in fresh DI water. the PVA layer is dissolved in water, the PMMA layer with target flake is floating on water.

(c) Plectrum

Transfer the PMMA layer on a new plectrum coated with PMMA. Heating to 90ºC to remove water.

(d) Monolayer TMD flake

40 μm

Glass slide
Plectrum
PMMA layer
TMD flake

Graphene
SiO₂ wafer

Sample stage

Align the target flake with a graphite flake on SiO₂ wafer. An optical image through the plectrum is shown at left.

Figure 3.10. Schematic diagrams showing the PMMA transfer step-by-step. (a) A monolayer is found on a PMMA/PVA/Si wafer. (b) The PVA layer is dissolved in fresh DI water. (c) The PMMA membrane is transferred onto a plectrum. (d) The top layer on the PMMA membrane is aligned to the bottom layer. (e) The top layer is brought into contact with the bottom layer. (f) The PMMA membrane is lifted-up, leaving the stack on the SiO$_2$/Si wafer. Optical images are shown as examples of the fabrication of a van der Waals stack by this method.

71

The plectrum was attached to one end of a glass slide, and this slide fixed to the transfer arm. The target TMD flake on PMMA was re-found in the optical microscope (Figure 3.10d) and aligned to a graphite flake on the SiO_2/Si wafer. After that, the temperature of the sample stage was set to 70°C, and the transfer arm brought down, so that the PMMA membrane approached the surface of the silicon. The temperature was increased to 80°C, using the round head of a tweezers to press the PMMA membrane to the wafer slightly making a small contact area, then this contact area would gradually expand, bringing the target flake into contact with the graphite (Figure 3.10e). After that, the plectrum was lifted leaving the TMD flake on the graphite (Figure 3.10f). Although the example shows a double-layer stack, the method is not limited to this. The procedure can be repeated to build up more complicated structures with more layers.

The example shown in Figure 3.10 is ideal since there are no breaks in the PMMA membrane during transfer. However, this is often not the case due to the fragility of the PMMA membrane. When there is a break or crack in the membrane, some areas adhere such that some of the PMMA membrane is left behind on the transfer arm / plectrum after lifting. To solve this, the PMMA layer is scratched/cut via tweezers with sharp tips; hence, the adhesive areas are left on the substrate.

To remove the PMMA from the silicon, the piece of wafer was immersed in acetone at 90°C for several hours. However, compared to the PPC film, the PMMA is not easy to remove. More of the polymer residue can be removed by an additional annealing step, this time at 300°C for 5 hours.

3.4.3 Comparison of PDMS and PMMA transfer

Compared to the PMMA transfer, the pick-and-place PDMS transfer has advantages in the preparation of the exfoliated flakes, especially for thin layers (e.g. mono- and bi-layers). As shown in Figure 3.6 and Figure 3.7b, the contrast of samples (monolayer graphene and $Mo_{0.5}W_{0.5}S_2$) on SiO_2/Si wafers under an optical microscopy is greater than those (monolayer $Nb_{0.1}W_{0.9}S_2$) on PMMA/PVA/Si wafers. When a van der Waals stack is successfully assembled without leaving PMMA membrane on top, i.e. by peeling away the PMMA, it is much cleaner than samples assembled via the PDMS pick-and-place transfer. However, when there is PMMA membrane left on the stacks, the samples from the pick-and-place are superior, especially for TEM samples, since the PPC film is easier
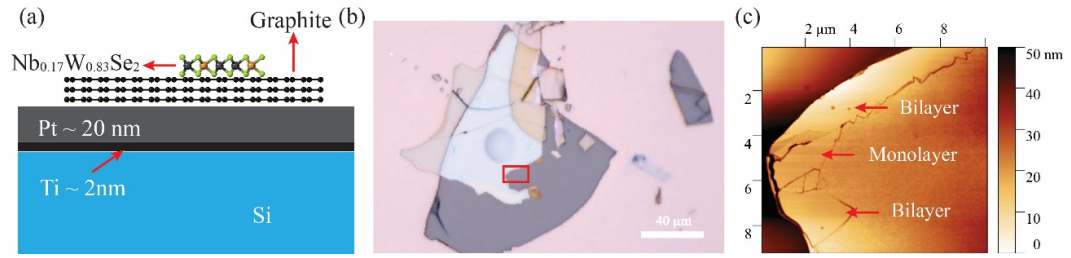
Figure 3.11. ARPES sample fabrication via the pick-and-place technique. (a) Schematic Figure shows the cross-section of the ARPES sample: van der Waals stack (top) on metal-coated Si wafer. (b) Optical image of the stack, the monolayer region is too small to be seen. (c) An AFM image, from the region marked by the red box in Figure 4b, showing the bilayer and monolayer regions.

to remove. This is clear from comparison between Figure 3.15a and 3.15c: there are much larger contamination free regions in Figure 3.15c.

Although thin materials are easier to find on SiO_2/Si wafers, they are not strong. Hence, the pressure introduced during the pick-and-place procedures can cause cracks and folds in the 2DM flakes. Another significant drawback of the pick-and-place technique is that it relies on a specific top layer (hBN or graphene) to pick the subsequent layers, hence the sequences of stacks are limited. In summary, each technique has advantages and disadvantages and the fabrication process must be chosen to match the samples that are required.

3.4.4 Sample fabrication for ARPES

Since ARPES measurements are surface sensitive, the requirement for cleanness is high. As introduced in Chapter 2, the measurement is also sensitive to the sample geometry, and therefore flat samples are required. Figure 3.11a shows a schematic cross section of an assembled van der Waals stack, $Nb_{0.17}W_{0.83}Se_2$/Graphite on a Pt(20nm)/Ti(2nm)/Si substrate, for ARPES measurements. The monolayer area is very small making it difficult to distinguish by optical microscopy (Figure 3.11b). Nevertheless, 2 µm by 2 µm monolayer and 2 µm by 8 µm bilayer regions were confirmed by atomic force microscopy (AFM) (Figure 3.11c). The AFM image shows a clean and homogeneous specimen without visible contaminants or bubbles.

3.5 A novel way to prepare TEM samples

3.5.1 Preparation of TEM samples of single 2DMs

Preparing 2DM samples for TEM, from single crystals, requires first mechanical exfoliation and then transfer of the resultant flakes to a TEM support grid. The simplest and quickest way is to transfer the flakes alone, without the fabrication of a heterostructure. The procedure for this is shown schematically in Figure 3.12, with optical images illustrating the process with $Mo_{1-x}W_xS_2$ flakes. A PMMA layer was spin-coated on pieces of SiO_2/Si wafers with exfoliated $Mo_{1-x}W_xS_2$ flakes (around 20 μm by 8 μm). The SiO_2/Si pieces were immersed in 2M potassium hydroxide (KOH) solution at $90^{\circ}C$ for 20 minutes which etched the SiO_2, releasing the PMMA coating which floated to the surface with the TMD flakes attached. To wash away the KOH residues, the PMMA layer was transferred to several batches of fresh DI water. Then a copper TEM grid (mesh size 400 μm) with a lacey carbon support film was used to capture the PMMA. Finally, the grid was immersed in acetone at $90^{\circ}C$ for several hours to remove the PMMA, leaving the TMD flakes on the lacey film as shown in the optical images in Figure 3.12. The monolayer area is almost invisible in the optical images but can be clearly resolved in the TEM images in Figure 3.12.

3.5.2 A novel way for encapsulated TEM samples preparation

As discussed in Chapter 2, although knock-on and ionisation mechanisms are both observed during imaging semiconductor TMD crystals[120,121], the dominant beam damage mechanism here is radiolysis since the electron beam energy 80 keV is lower than the experimentally determined threshold energy for atomic displacements for most 2D TMD materials[93]. An encapsulation layer can be effective in protecting the specimen[94], however, there are several considerations for choosing an effective coating material.

   i. The material should give low background signal so that the signal-to-noise (S/N) ratio is high[120,121].

   ii. The material should be a good electrical and thermal conductor so that the effects of charge and thermal vibration can be minimised[93,120].
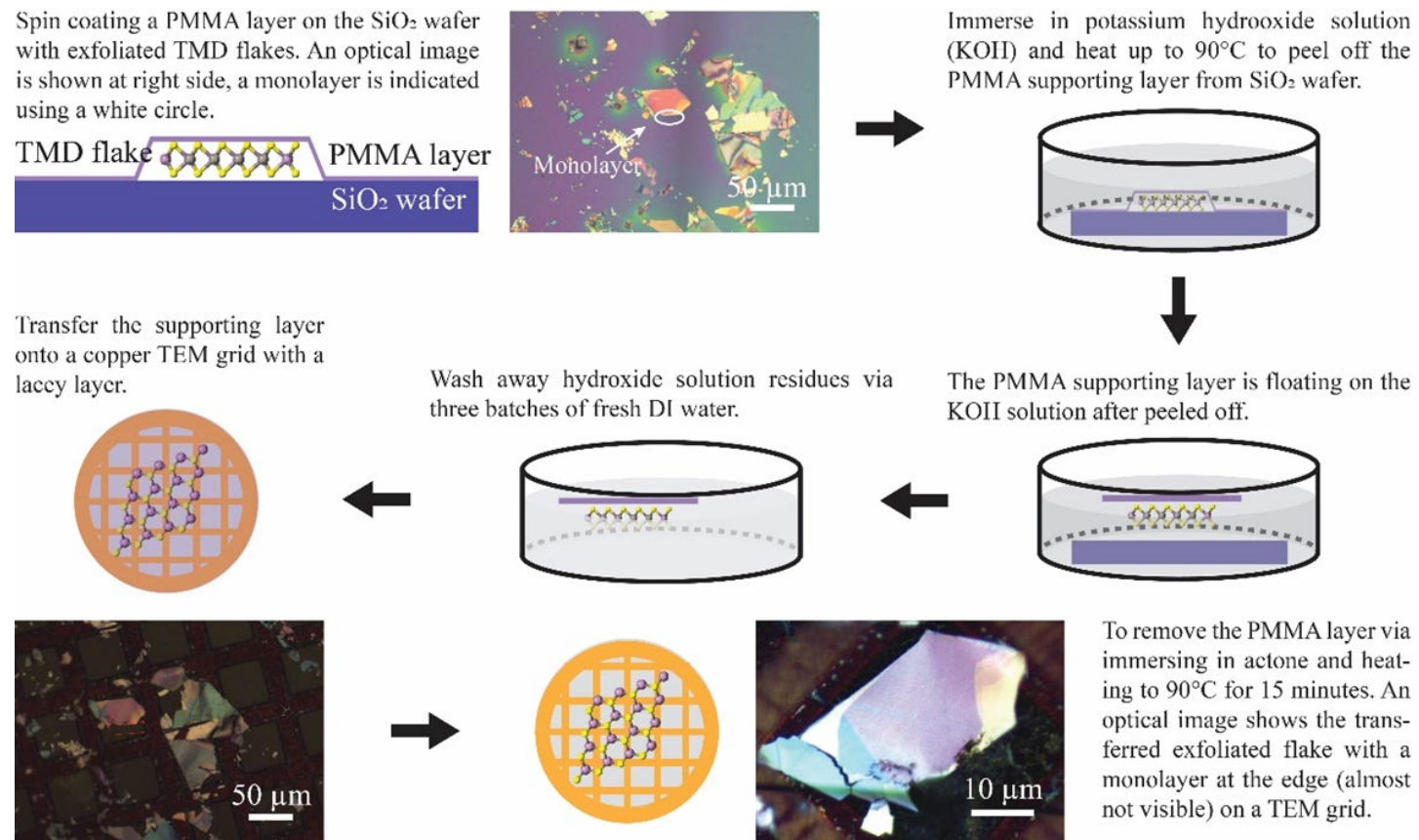
Figure 3.12. Wet transfer of TMD flakes exfoliated on SiO_2 wafer using a PMMA coating as a supporting layer. Optical images show an example of a $Mo_{0.63}W_{0.37}S_2$ monolayer transferred in this way.
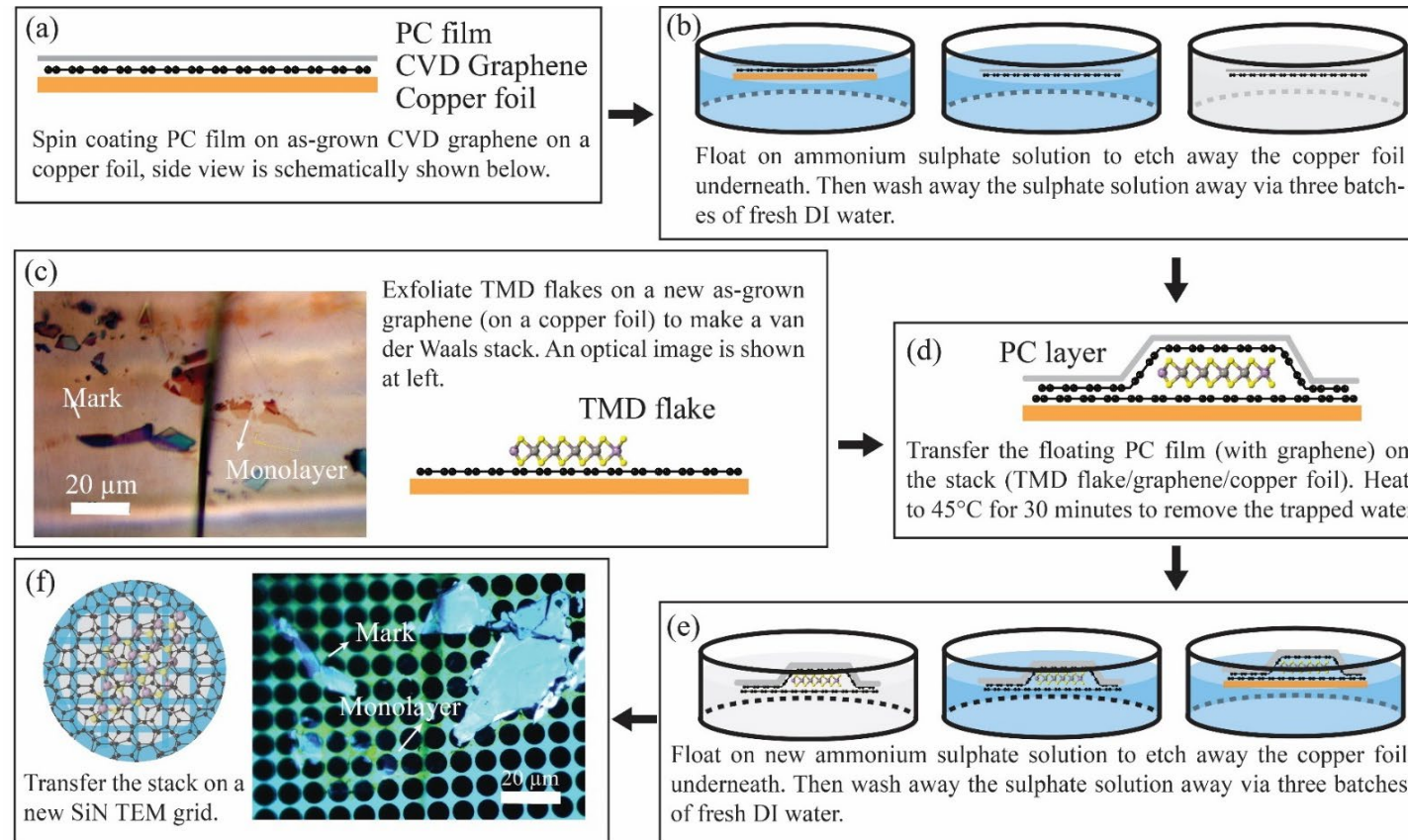
Figure 3.13. Schematic diagrams showing the technique developed for fabrication of TEM samples of encapsulated TMD flakes. (a) Coat graphene-on-copper with a PPC film. (b) Etch away the copper foil. (c) Exfoliate TMD flakes onto the CVD-grown graphene-on-copper foil. (d) Transfer the structure PPC film / graphene onto the stack TMD flake / graphene / copper foil. (e) Etch away the copper foil. (f) Transfer the stack (PPC film / graphene / TMD flake / graphene) onto a new SiN grid. The optical images show an example of a Re-MoS$_2$ monolayer prepared for TEM analysis via this technique.

Graphene ideally satisfies these constraints, so we developed a technique for fabricating graphene encapsulated flakes for TEM analysis.

The pick-and-place techniques described earlier in this chapter could be used for encapsulating flakes in graphene (see next section). Nevertheless, the process has many steps, the yield can be low when using only such thin layers in the stacks and transferring the resultant heterostructure to the TEM grid can be complicated. To address this, we developed a wet transfer technique using large-area CVD grown graphene on copper foil, as shown schematically in Figure 3.13[122].

First a polymer-supported floating layer of CVD-grown graphene is formed. A PPC film is spin-coated onto a piece of copper foil which has been covered by graphene using CVD. The foil is placed on top of an ammonium sulphate solution (50 mg/ml) for 30 minutes. The ammonium sulphate etches the copper, breaking the graphene coating on the back side of the foil. The damaged graphene is washed away by DI water. Then the foil is replaced on the ammonium sulphate solution for a few more hours to finish etching away the copper foil, leaving the PPC supported graphene floating on the surface. This is washed by carefully transferring to three successive petri dishes of fresh DI water.

Next, TMD crystals are exfoliated on to another piece of CVD-grown graphene and a monolayer area found by optical microscopy as shown in the optical image in Figure 3.13. The PPC film/graphene is transferred onto the targeted area and the stack is heated to 45°C for 30 minutes on a hot plate to remove the water trapped between the top and bottom graphene. Then the back-side graphene and copper foil are removed as previously described.

Finally, the stack (PPC film/Graphene/TMD flakes/Graphene) is transferred onto a SiN grid and the PPC film dissolved in chloroform solution. An optical image of a completed sample in Figure 3.13, shows the successful transfer of the target area/flake.

3.5.3 Encapsulated TEM sample via dry transfer

Encapsulation by wet transfer with CVD-grown graphene, as described above, proved to be a comparatively simple and high-yield approach. But it does have some limitations: mechanical exfoliation of each type of flake onto the graphene on copper must be
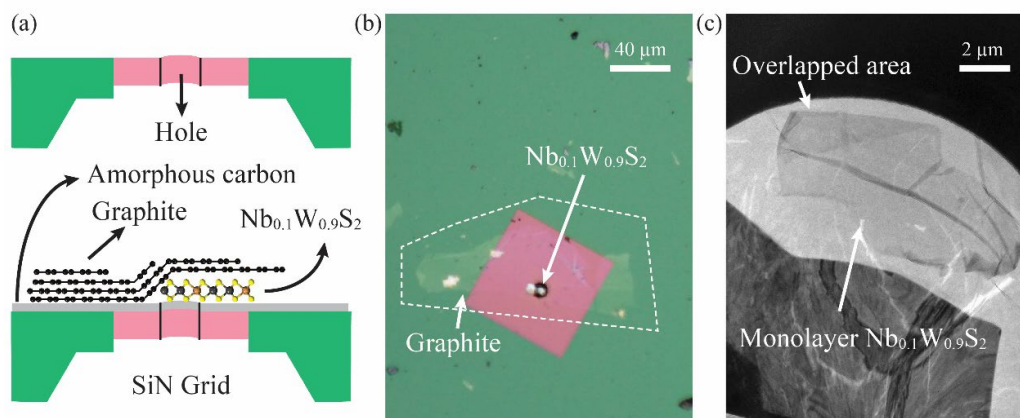
Figure 3.14. TEM sample fabrication. (a) Schematic figure showing the cross-section of SiN grid (top) and the van der Waals stacks (bottom) on amorphous carbon coated grid. (b) Optical image of the stacks (the monolayer region is too small to be seen). (c) Corresponding STEM image at low magnification showing the stacks suspended on the hole of SiN grid.

optimised and more complicated heterostructures are difficult to make in this way. For this reason, we also developed TEM sample fabrication by pick-and-place transfer. Figure 3.14a schematically shows a van der Waals stack (graphene/$Nb_{0.1}W_{0.9}S_2$) on an amorphous carbon coated SiN grid with a single central hole to facilitate finding the sample. First, graphene was picked up by a PDMS/PPC film, as described before, and this was used to pick up a $Nb_{0.1}W_{0.9}S_2$ flake. The SiN grid was coated with an amorphous carbon layer, to reduce charging and increase adhesion of the stack. The grid was stuck to a glass slide and mounted on the sample stage of the pick-and-place system. The desired stack was aligned to the central hole and put down on the SiN grid. Finally, the PPC film was dissolved by chloroform and then annealed at 200°C for 4 hours.

With this methodology, it was difficult to accurately align the area of interest, i.e. the monolayer/bilayer region, with the SiN membrane hole. The $Nb_{0.1}W_{0.9}S_2$ flake was not visible in the optical images (Figure 3.14b) since the area was too small (white arrow indicates the flake position). Nevertheless, the monolayer/bilayer $Nb_{0.1}W_{0.9}S_2$ specimen can be observed at low magnification in STEM (Figure 3.14c), the flake is clean with little visible contamination, indicating that the 10 μm by 4 μm monolayer/bilayer flake was successfully and precisely placed on the 20 μm hole. This demonstrates that this transfer system is clean, accurate and reliable.

3.5.4 Annealing

As a final step, to remove water, polymer residues and other contaminants such as adventitious carbon, the TEM grids were carefully annealed in a vacuum tube furnace. This was necessary for samples made both by dry and wet transfer. The tube furnace was operated at low pressure (around 10 Torr) under a low flow of a mixture of H_2 and Ar_2 gas The samples were heated to 200°C at a rate of 8°C/minute, maintained at that temperature for 4 hours and then allowed to cool to room temperature. STEM analysis was performed as soon as possible after removal from the annealing furnace.

3.5.5 Comparison of TEM samples

Figure 3.15a is an ADF-STEM image of a $Mo_{0.63}W_{0.37}S_2$ monolayer prepared without encapsulation using the wet transfer described in section 3.5.1, using an A4 PMMA as the supporting layer. Most of the flakes are lying on lacey film so they are exposed to the electron beam during characterisation. The beam will damage/burn a monolayer rapidly before the line-by-line STEM scans finish. Moreover, in the image captured before damage, many regions are covered by thick amorphous contamination that obscures the flake to be covered. The dominant source of this contamination is polymer residue from the A4 PMMA which cannot be fully removed by annealing. Therefore, although this method is comparatively simple and is widely used in TEM sample preparation, its disadvantages are obvious.

Figure 3.15b shows an ADF-STEM image of a Re-MoS$_2$ monolayer prepared using the novel protocol introduced in section 3.5.2. The TMD flake is encapsulated by a top and bottom layer graphene, considerably reducing the electron beam damage. The PPC support film used for the transfer, 1wt% PPC dissolved in chloroform, is easier to remove. As a result, there are larger contamination free regions in Figure 3.15b compared to Figure 3.15a.

Figure 3.15c shows an ADF-STEM image of a $Nb_{0.1}W_{0.9}S_2$ monolayer prepared by the dry transfer technique described in section 3.5.3. The graphene covering on the TMD flake makes the characterisation process easier and improves the quality of the images. Although a thicker PPC film was used, 8wt% PPC dissolved in chloroform, there are still

large enough contamination free regions to allow statistical analysis of the atomic structure.

Comparing the ADF images in Figures 3.15b and 3.15c, both techniques allow the preparation of stable and clean samples suitable for high-resolution STEM analysis. However, compared with dry transfer, the G/TMD/G stack assembly via direct exfoliation is faster and cheaper. Therefore, this method can be a good alternative to dry transfer for imaging TMD monolayers.

3.6 Conclusion

In summary, single crystals of pure and alloy TMD materials such as $Mo_{1-x}W_xS_2$, $Nb_{0.1}W_{0.9}S_2$, $Nb_{0.17}W_{0.83}Se_2$, WSeS and WSe_2 have been synthesized by CVT. A dry transfer system has been developed for the 2D heterostructure fabrication and optimised for the sample designs required for this thesis; both PDMS and PMMA based transfers have been shown to be effective for the fabrication of samples of different types. Moreover, a novel transfer method was developed to prepare encapsulated TEM samples. As will be shown in the following chapters, the preparation of high-quality and clean heterostructure samples via these techniques is necessary for detailed atomic and electronic structure investigations.
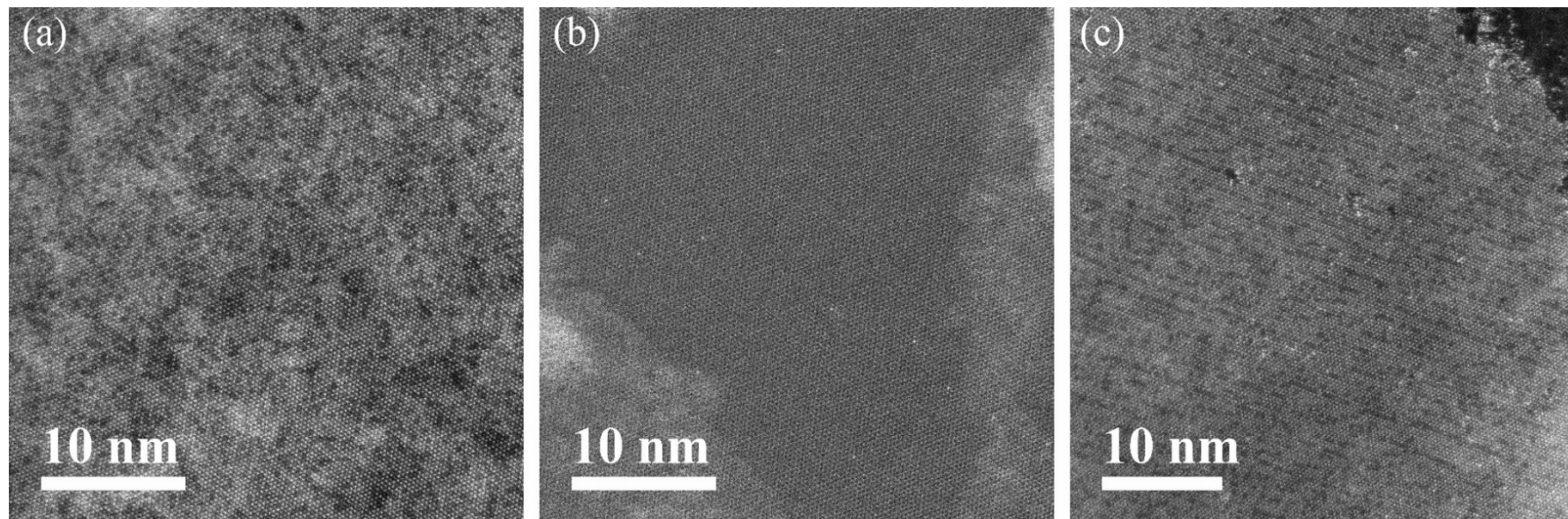
Figure 3.15. Comparison of ADF-STEM images of TEM samples prepared via different transfer techniques. (a) ADF-STEM image of a $Mo_{0.63}W_{0.37}S_2$ monolayer prepared by the PMMA transfer method shown in Figure 3.12. (b) ADF-STEM image of a Re-MoS$_2$ monolayer, under the same image conditions, prepared by the novel wet transfer method shown in Figure 3.13. (c) ADF-STEM image of a $Nb_{0.1}W_{0.9}S_2$ monolayer prepared by the pick-and-place transfer technique.

Chapter 4: Atomic and Electronic Structure of Random Distributed Alloys

4.1 Introduction

Recently, several studies have focused on how to control/tune the atomic and electronic structure of the semiconducting MoWSeS TMD family via alloying[39,40,56,57,123]. Optical spectroscopy measurements have been used to indirectly determine band structure parameters like the band gaps[40,56] and the SOC splits at the band edges[39]. However, there is an obvious drawback; these measurements, primarily based on PL, do not accurately determine the single-particle electronic structure. The optical band gaps measured via PL correspond to the energy given out by the recombination of an electron in the CB and a hole in VB which are bound together through the Coulomb interaction to create an exciton. The high exciton binding energies complicate and obscure the analysis of electronic structure parameters from these optical spectroscopy measurements[22,124]. By contrast, ARPES measurements based on a photoemission process are more direct, giving a visual representation of the full VB structure from which the electronic structure parameters can be directly measured[22].

Therefore, this chapter will focus on 2D $Mo_{1-x}W_xS_2$ alloys, correlating the evolution of the atomic structure (directly measured by electron microscopy) and the electronic structure (measured by ARPES) as a function of W content (x), and comparing these measurements to first principles calculations. To achieve this, TMD alloy crystals were initially synthesised via CVT, as described in section 3.2, and their composition was carefully measured using a combination of analytical techniques. The atomic structure of $Mo_{1-x}W_xS_2$ monolayer flakes (shown schematically in Figure 4.1) was visualised using ADF-STEM imaging, quantitatively analysed, and compared to first principles calculations and Monte Carlo simulations. These direct measurements of the atomic

structure revealed that the W atoms are randomly distributed in the Mo matrix with atomic arrangements consistent with those thermodynamically expected.

To directly study the electronic structure changes in $Mo_{1-x}W_xS_2$ alloys, ARPES measurements were undertaken on these well-characterised single crystals, revealing how the SOC scaled linearly with the stoichiometry (x). Linear scaling DFT, using large unit cells to avoid simulation artefacts, was carried out by our collaborators in the group of Dr Nicholas Hine; their results are compared with the atomic and electronic structure of $Mo_{1-x}W_xS_2$ that were determined experimentally. The predictions obtained are consistent with the ARPES results, validating both the experimental measurements and theoretical predictions.
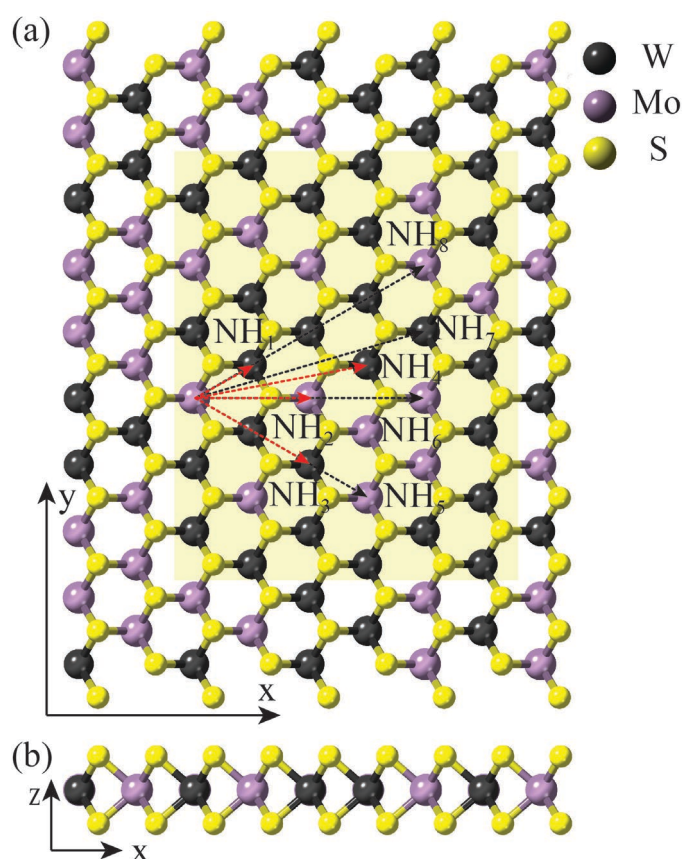
Figure 4.1. Atomic structure of $Mo_{1-x}W_xS_2$ monolayer. (a) Top view of $Mo_{1-x}W_xS_2$ monolayer. Purple, dark grey and yellow atoms present molybdenum, tungsten and sulphur, respectively. The area with a yellow background is the selected simulation area used in red box in Figure 4.8c. (b) Side view of $Mo_{1-x}W_xS_2$ monolayer.

Furthermore, although the predictions indicate that the SOC at the CBM should be less than the spatial fluctuations in potential energy due to disorder in the alloys at intermediate compositions, polarisation resolved PL measurements on a $Mo_{0.5}W_{0.5}S_2$ monolayer flake demonstrate that the spin-valley locking is retained across the alloy range.

4.2 Sample fabrication

4.2.1 Material synthesis

The crystals were grown via CVT as described in Chapter 3. The photographs in Figure 4.2 show a series of $Mo_{1-x}W_xS_2$ bulk crystals with compositions from $x = 0$ to 1. The sizes of these crystals vary with their composition due to the different growth conditions used (*e.g.* flux of transport agent, growth temperature, time *etc.*). Bulk crystals with optimised conditions, like $Mo_{0.51}W_{0.49}S_2$, can be up to 2 cm across, while if the conditions were less favourable, such as for WS_2, the crystals are smaller than 0.5 mm across.
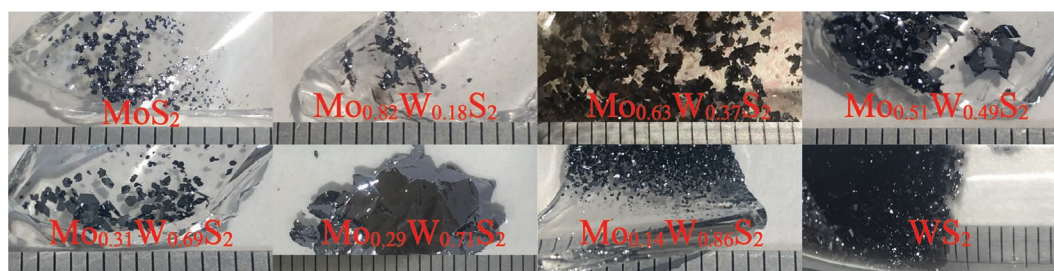
Figure 4.2. Photos of as-grown $Mo_{1-x}W_xS_2$ bulk crystals. The composition $x = 0$, 0.18, 0.37, 0.49, 0.69, 0.71, 0.86 and 1, respectively.

4.2.2 TEM sample preparation

To prepare samples for transmission electron microscopy (TEM), $Mo_{1-x}W_xS_2$ single crystals were first exfoliated onto CVD grown graphene on copper foil to form a heterostructure (see schematic in Figure 4.3a). $Mo_{1-x}W_xS_2$ monolayers can be easily identified via their optical contrast, as indicated in Figure 4.3a. PPC supported graphene, again grown by CVD, was wet transferred onto these structures, as described in Chapter 3. After etching the copper foil away, the heterostructures (PPC layer/graphene/Mo_{1-}

$_x$W$_x$S$_2$ flake/graphene) were left floating on fresh DI water. Silicon nitride TEM grids (from Silson Ltd.) were used to scoop the heterostructures from the water surface. An example of a Mo$_{0.78}$W$_{0.22}$S$_2$ flake encapsulated by graphene and transferred onto a silicon nitride TEM grid is shown in Figure 4.3b. The flake appears with a bluish colour in the optical image. After drying the specimen under a lamp, the PPC film was washed away using fresh chloroform and then acetone. The silicon nitride TEM grid containing the heterostructure stack was annealed at 300 °C under H$_2$/Ar gas for three hours to finish the removal of the polymer supporting layer.
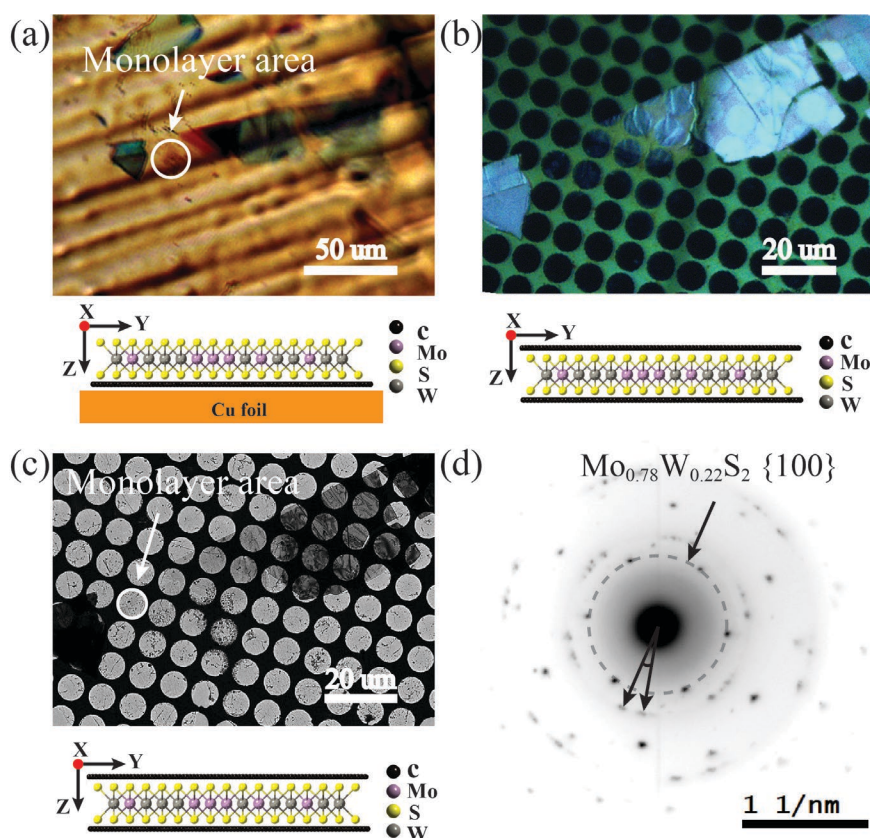
Figure 4.3. TEM sample of graphene encapsulated Mo$_{0.78}$W$_{0.22}$S$_2$ flake. (a) Optical image of Mo$_{0.78}$W$_{0.22}$S$_2$ monolayer flakes exfoliated onto graphene on copper foil. (b) Optical image of flakes encapsulated by graphene after transfer onto a SiN TEM grid. (c) Low magnification TEM image of the same area as the optical image in (b). Inserted below in (a), (b) and (c) are schematic side views of the heterostructure (graphene/monolayer flake/graphene). (d) Diffraction pattern from the selected area indicated by the white circle in Figure 4.3(c). The two unlabelled black arrows point to two diffraction spots from the two different graphene layers.

The same monolayer flake was tracked through all the transfer process and re-found in TEM afterwards, as can be observed in the low magnification TEM image in Figure 4.3c. SAED patterns were recorded to verify the flake crystal structure. Thus, for example, the diffraction pattern in Figure 4.3d corresponds to the area enclosed in the white circle in Figure 4.3c. There are spots in the diffraction pattern corresponding to the TMD flake, as well as to each graphene layer between which the TMD was sandwiched. In the example in Figure 4.3c, the two graphene layers are rotated by a 12.9° twist angle relative to each.

4.3 Characterisation of $Mo_{1-x}W_xS_2$ crystals

Prior to specimen preparation for TEM, ARPES and polarisation resolved PL, the as-grown alloys crystals, taken directly from the broken ampoules, were analysed to determine their crystal structure and stoichiometry. As described below, optical spectroscopy measurements of these alloys were found to be consistent with the prior literature, confirming that the crystal quality is good and that they are representative of CVT grown alloy crystals.

4.3.1 Calibration of $Mo_{1-x}W_xS_2$ bulk crystals

MoS_2 and WS_2 have similar unit cells, belong to the same space group, with only a 0.3% difference in their lattice constant. Therefore, the crystal structure of the alloys is expected to be similar to the pure materials, with intermediate lattice constants. To investigate the crystal structures, XRD was applied to the bulk crystals of the different alloys.

Although during synthesis each element was added to the quartz ampoule stoichiometrically, the final composition of the crystals was found to vary from their nominal values. Since this research is focused on composition-dependent atomic and electronic structures, it was important to calibrate accurately the actual stoichiometry of the alloys. To do this, several complementary techniques were used to qualitatively *e.g.* Raman shifts, and quantitatively, *e.g.* X-ray photoelectron spectroscopy (XPS) and scanning electron microscopy energy dispersive X-ray spectroscopy (SEM-EDX), determine the stoichiometric proportion of W to (Mo + W).

4.3.1.1 Crystal structure

To determine the crystal structure, the as-grown crystals were crushed and analysed by powder XRD. As illustrated in Figure 4.4a, the diffraction patterns from all compositions show strong [*00l*] diffraction lines, indicating that both the pure WS_2 and alloy crystals possess layered hexagonal crystal structure. Compared to the [*00l*] reflections, the other diffraction lines are very weak, indicating that the crystal surfaces naturally lie in the crystallographic *ab*-plane. To identify the polytypes from the data in Figure 4.4a, the weaker peaks are shown with a magnified scale in figure 4.4b and compared to the experimental position and intensity of diffraction lines for the standard polytypes, $2H-WS_2$, $3R-WS_2$, $2H-MoS_2$ and $3R-MoS_2$[108,109,125,126].

For the pure WS_2, the peaks indicated with the pink triangle symbol in the red plot in Figure 4.4b are compared to standard patterns for the 2H- and $3R-WS_2$ phases. The peak positions are consistent with the 2H and not the 3R polytype, confirming that the bulk crystals grow exclusively as the 2H polytype. The prominent lines in the red plot are indexed with their (*hkl*) values; from these, the lattice parameters were calculated to be $a = b = (3.161 \pm 0.002)$ Å and $c = (12.357 \pm 0.005)$ Å. These values are consistent with the known standard values of pure WS_2 $a = b = (3.155 \pm 0.005)$ Å and $c = (12.350 \pm 0.013)$ Å[109].

The same type of analysis was carried out for each set of alloy crystals. The crystal structure of the W rich alloys were close to that of pure $2H-WS_2$; for example XRD data from $Mo_{0.29}W_{0.71}S_2$ is shown in Figure 4.4, giving calculated lattice constants of $a = b = (3.162 \pm 0.005)$ Å and $c = (12.319 \pm 0.008)$ Å as recorded in Table 4.1. The lattice parameters of Mo rich alloys were closer to the known values of $2H-MoS_2$ (3.160 ± 0.010) Å and (12.294 ± 0.008) Å[126]. For $Mo_{0.63}W_{0.37}S_2$ the lattice parameters are $a = b = (3.155 \pm 0.005)$ Å and $c = (12.303 \pm 0.009)$ Å. The most obvious change with composition is that the layer spacing, reflected by c, increases with increasing W content (i.e. x), giving a quick check for the stoichiometry of the bulk crystals.
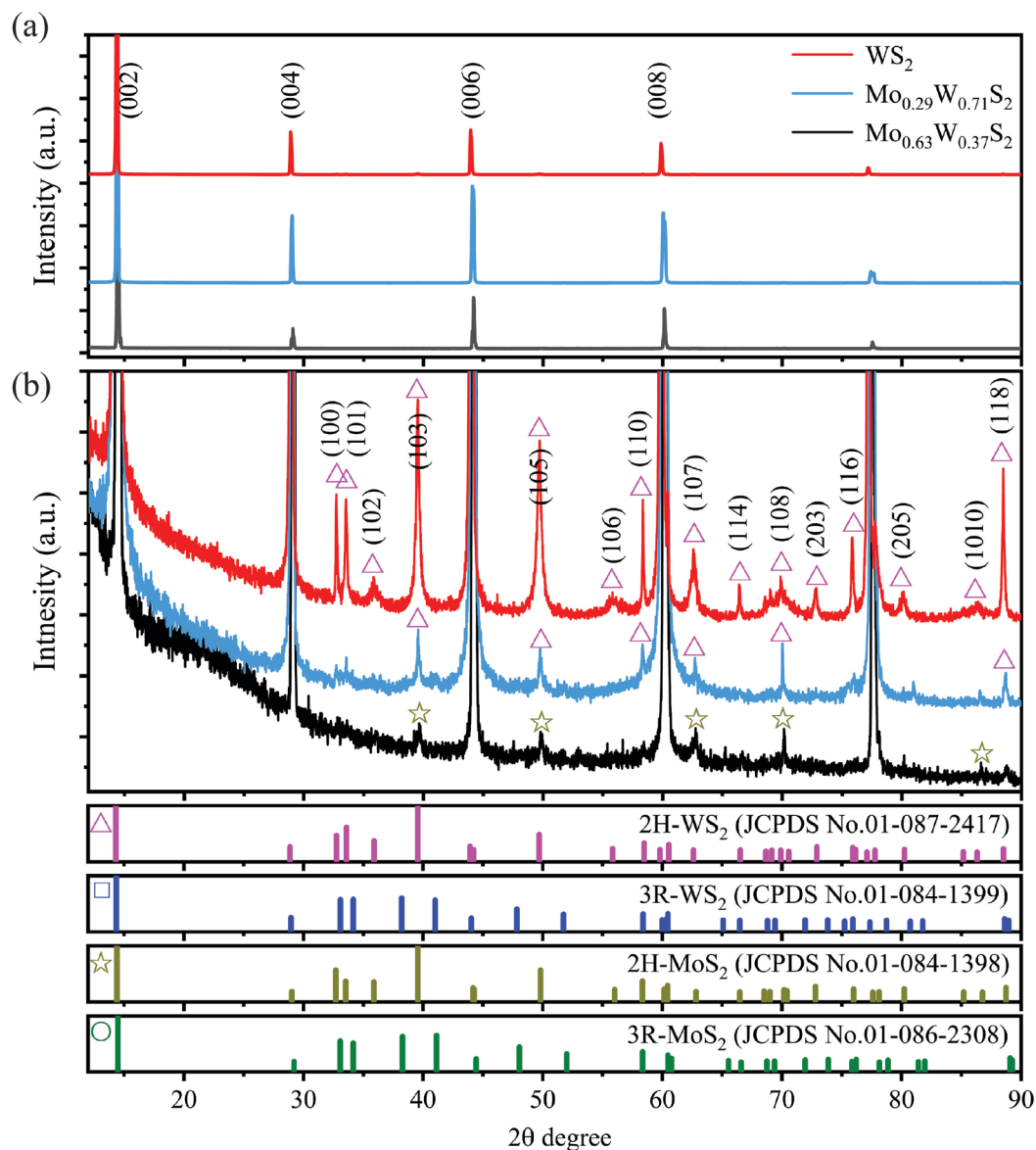
Figure 4.4. XRD patterns of as-grown $Mo_{1-x}W_xS_2$ single crystals compared with predicted XRD patterns from most common polytypes. (a) X-ray powder diffraction patterns of crushed $Mo_{1-x}W_xS_2$ bulk crystals (x=0.37, 0.71 and 1). (b) (upper) Magnified view of the weaker peaks in Figure a (lower) predicted powder diffraction patterns for the most common polytypes[108,109,125,126]. The symbols with different colours and shapes mark the peaks matched with those in the expected diffraction patterns, as labelled.

The XRD patterns showed that all the alloys have grown with the 2H polytype structure, and the sharp diffraction peaks suggest that the crystal quality of the alloys is comparable to that of the pure WS_2 crystals. However, it is difficult to identify whether they are single crystals or polycrystalline from the powder diffraction patterns.

Table 4.1. Lattice parameters of CVT-grown $Mo_{1-x}W_xS_2$ crystals calculated from XRD patterns.

Sample	a	b	c
Reported value WS_2[109]	(3.155 ± 0.005) Å	(3.155 ± 0.005) Å	(12.350 ± 0.013) Å
Sample WS_2	(3.161 ± 0.002) Å	(3.161 ± 0.002) Å	(12.357 ± 0.005) Å
Sample $Mo_{0.29}W_{0.71}S_2$	(3.162 ± 0.005) Å	(3.162 ± 0.005) Å	(12.319 ± 0.008) Å
Sample $Mo_{0.63}W_{0.37}S_2$	(3.155 ± 0.005) Å	(3.155 ± 0.005) Å	(12.303 ± 0.009) Å
Reported value MoS_2[126]	(3.160 ± 0.010) Å	(3.160 ± 0.010) Å	(12.294 ± 0.008) Å

For example, as shown in Figure 4.3, TEM SAED patterns were acquired from exfoliated flakes. A series of SAED patterns were taken across this exfoliated flake that is around 10 μm, the spots corresponding to $Mo_{0.78}W_{0.22}S_2$ stayed in the same orientation, while the graphene diffraction patterns rotated across the sample. Therefore, the CVD-grown graphene is polycrystalline, but this alloy flake is a single crystal. Then this method has been applied to the TEM samples with compositions $x = 0.22, 0.41, 0.51$ and 0.63, confirming these alloys are also single crystals.

4.3.1.2 Compositional analysis

a. Raman shifts

For bulk crystals, the Raman active modes are composition-dependent[127,128], therefore confocal Raman spectroscopy can be applied to probe the change in phonon modes with alloy compositions.
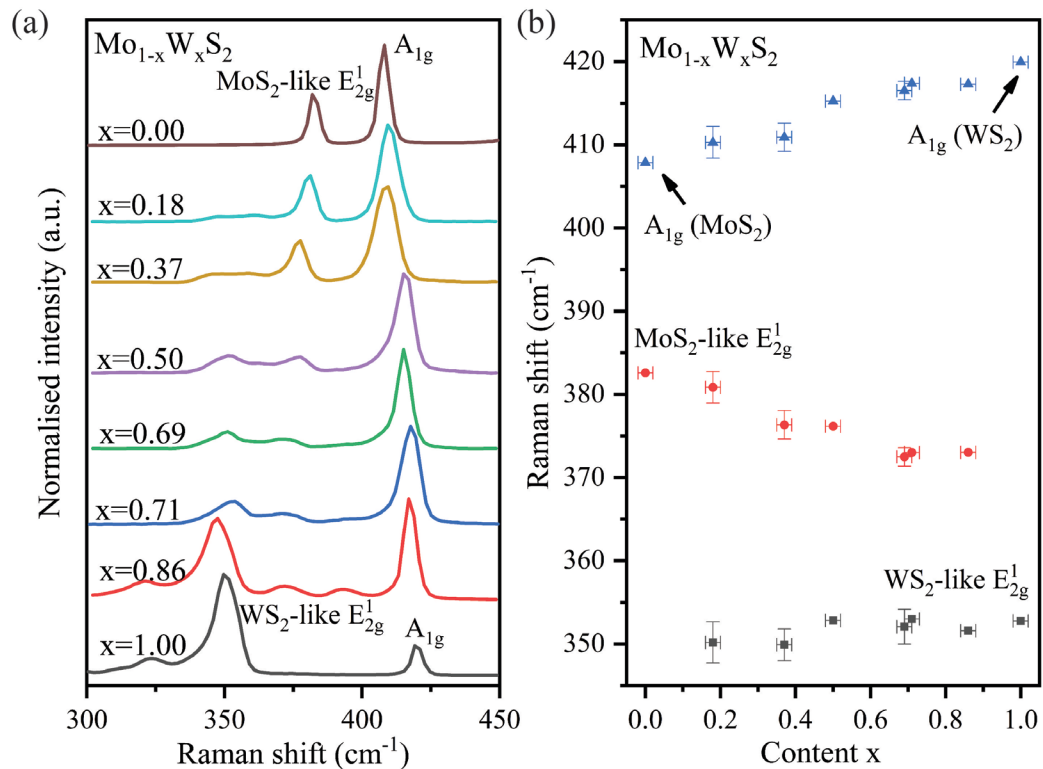
Figure 4.5. Raman spectra of 2H-$Mo_{1-x}W_xS_2$ single crystals. (a) Raman spectra from 2H-$Mo_{1-x}W_xS_2$ single crystals (at 532 nm excitation). (b) The variation of A_{1g} and E_{2g}^1 modes as a function of W content x.

Bulk MX_2 (M = Mo and W) possess D_{6h} point group symmetry; they have 12 modes of lattice vibrations at the Γ point in the BZ and four of them are first-order Raman-active, A_{1g}, E_{1g}, E_{2g}^1 and E_{2g}^2[79]. In back-scattering experiments on the surface perpendicular to the c-axis, A_{1g}, E_{2g}^1 and E_{2g}^2 are allowed[79]. Since E_{2g}^2 is in a low Raman shift range (between 32 and 27 cm^{-1})[128], it is simpler to measure A_{1g} and E_{2g}^1 to probe the stoichiometry, as shown in Figure 4.5.

Figure 4.5a shows Raman spectra from $Mo_{1-x}W_xS_2$ bulk crystals, in the range 300 to 450 cm^{-1}. In the pure materials, MoS_2 and WS_2, two main vibration modes are observed, the A_{1g} and E_{2g}^1. These modes correspond to out-of-plane and in-plane directions, respectively[79]. In contrast, three modes appear for ternary phases: one A_{1g} mode and two E_{2g}^1 (WS_2- and MoS_2-related) modes. For the A_{1g} mode, since it is related to sulphur atom vibrations perpendicular to the plane of the layers, the mixed alloy crystals only show one mode[128]. In contrast, the E_{2g}^1 modes can be attributed to metal and sulphur atoms vibrating in the ab-plane, therefore two modes are observed for alloys containing both metals[127,128].

Figure 4.5b summarises the evolution of the three composition-dependent Raman active modes as a function of W content from $x = 0$ to 1. As the W content increases, A_{1g} modes shift to higher wavenumber, from 408 cm^{-1} for MoS_2 to 420 cm^{-1} for WS_2. By contrast, MoS_2-like E_{2g}^1 modes shift to lower value and disappear in pure WS_2, while WS_2-like E_{2g}^1 modes appear from a small amount of W doping and upshift by a small value. These tendencies are in an agreement with the literature and again give a simple qualitative approach to quantifying the Mo and W compositions in random distributed solid solutions[79,127,128].

b. SEM-EDX and XPS

SEM-EDX was used to quantify the stoichiometry of the different alloys. However, since the K_α lines of S atoms overlap with the L_α lines of Mo atoms, it is difficult to deconvolute the two peaks precisely. Therefore, XPS was introduced as a complementary technique to compare and corroborate the SEM-EDX data. The composition for the different alloys obtained by SEM-EDX are summarised in Table 4.2, while XPS spectra from alloys and pure binary crystals are compared in Figure 4.6. As

XPS is surface sensitive and EDX is more bulk sensitive, the combination of both techniques gives a more robust compositional analysis.

For pure 2H-MoS$_2$ crystals, the Mo 3d$_{3/2}$ and Mo 3d$_{5/2}$ core levels are located at 232.0 eV and 228.9 eV, respectively, while for 2H-WS$_2$ crystals the W 4f$_{5/2}$ and W 4f$_{7/2}$ peaks are at 34.5 eV and 32.3 eV, respectively. These are in an agreement with the literature values[129,130]. Furthermore, there are additional doublet features at higher binding energies in the crystals that are associated with their higher oxidation states (Mo^{6+} and W^{6+} corresponding to Mo-O and W-O, respectively)[130].
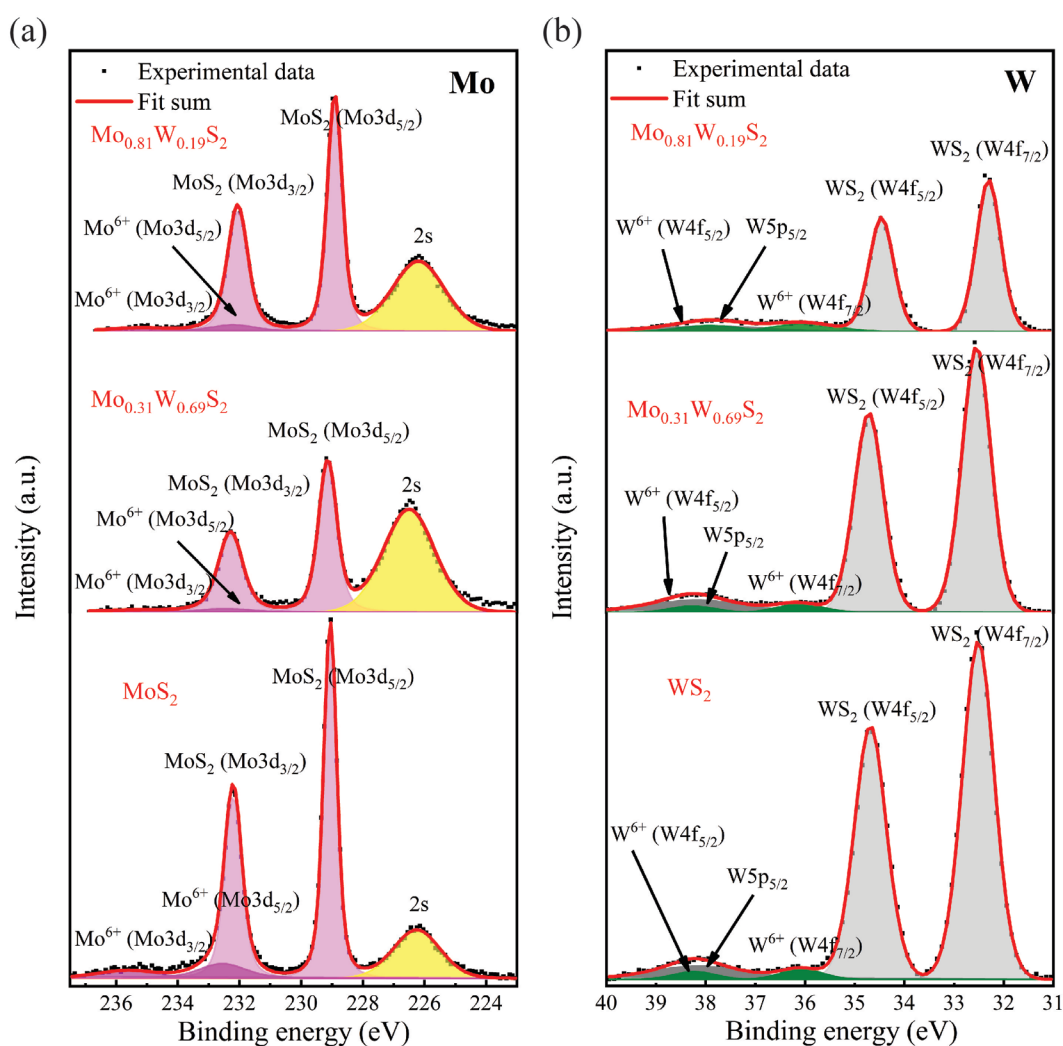
Figure 4.6. X-ray photoelectron spectroscopy on Mo$_{1-x}$W$_x$S$_2$ single crystals (x=0, 0.19, 0.69 and 1). Mo 3d and W 4f spectra with Gaussian-Lorentzian fitting of each peak.

Compared to the pure materials, in the pristine 2H-$Mo_{0.31}W_{0.69}S_2$, the Mo $3d_{5/2,3/2}$ peaks and oxidised states shift to lower binding energies, while shifts of the W $4f_{7/2,5/2}$ peaks of these states are very small. For the Mo rich end, both the Mo $3d_{5/2,3/2}$ and W $4f_{7/2,5/2}$ peaks shift to lower binding energy, compared to the W rich and pure W materials. These shifts in binding energies for the alloys are also in an agreement with prior work[129]. The stoichiometric ratio of W to (Mo + W) can be calculated by integrating the intensities of the Mo and W fitting peaks, applying standard sensitivity-factor corrections. The derived results are shown in Table 4.2 and compared to the SEM-EDX values.

In summary, it is clearly shown in Table 4.2 that the stoichiometric values from different characterisation techniques are in good agreement within their error bars, indicating our composition analysis is accurate and reliable. But the compositions differ from the nominal values (i.e. the amount of material added to the ampoules), showing the importance of measuring the composition to determine the actual stoichiometry of the bulk crystals.

4.3.2 Optical properties of $Mo_{1-x}W_xS_2$ monolayer flakes

The 2H single crystals were exfoliated onto SiO_2 wafer as described in chapter 3, and room temperature PL measurements were acquired.

Figure 4.7a shows PL spectra for all the compositions from MoS_2 to WS_2. The dependence of the photoemission peak energy on composition is shown in Figure 4.7b. The A exciton emission peak shifts continuously and nonlinearly from 1.855 eV at $x = 0$ to 1.981 eV at $x = 1$. The PL peak energy (E_{PL}) as a function of x is well described by the equation:

$$E_{PL}(x) = (1 - x)E_{PL}^{MoS_2} + xE_{PL}^{WS_2} - bx(1 - x) , \qquad 4.1$$

where b is the bowing parameter[40,56].

Table 4.2. Comparison between compositions determined by EDX and XPS from $Mo_{1-x}W_xS_2$ single crystals.

$Mo_{1-x}W_xS_2$ crystals	Nominal W content x	EDX	Error bar	XPS	Error bar
MoS_2	0	0	0.02	0	0.02
$Mo_{0.82}W_{0.18}S_2$	0.13	0.18	0.02	0.16	0.02
$Mo_{0.63}W_{0.37}S_2$	0.38	0.37	0.02	0.37	0.02
$Mo_{0.51}W_{0.49}S_2$	0.50	0.50	0.02	0.49	0.02
$Mo_{0.31}W_{0.69}S_2$	0.63	0.69	0.02	0.69	0.02
$Mo_{0.28}W_{0.72}S_2$	0.75	0.71	0.02	0.74	0.02
$Mo_{0.14}W_{0.86}S_2$	0.86	0.86	0.02	0.86	0.02
WS_2	1.00	1.00	0.02	1.00	0.02
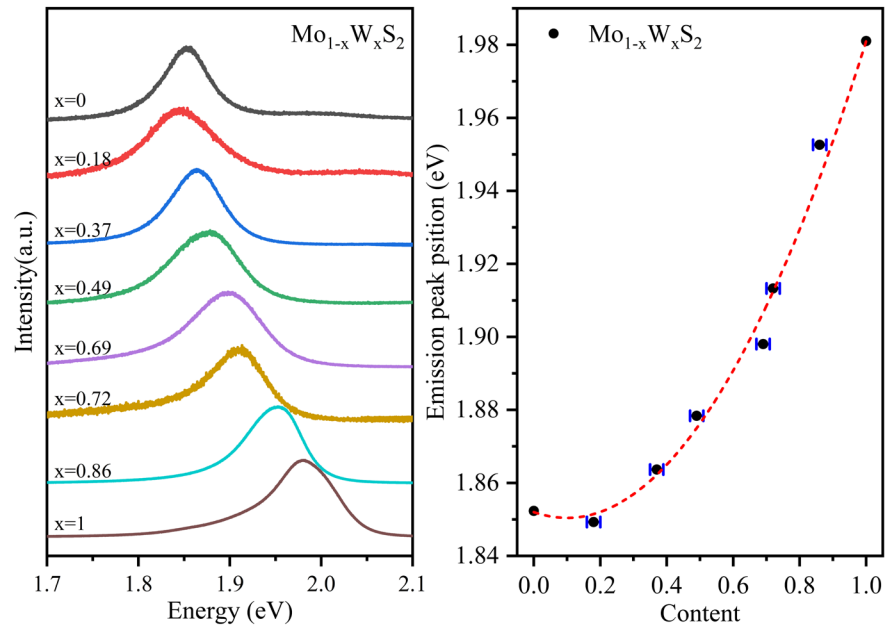
Figure 4.7. PL emission spectra from $Mo_{1-x}W_xS_2$ monolayers. (a) PL spectra of $Mo_{1-x}W_xS_2$ monolayers with 532 nm excitation. (b) Evolution of PL emission peaks with increasing W composition x (0 to 1).

The bowing parameter here is $b = (0.17 \pm 0.01)$ eV. This observed bowing is consistent with prior reports and is indicative of nonlinear changes in the band gap and/or exciton binding energies[56]. To further study the composition-dependence of the $Mo_{1-x}W_xS_2$ electronic structure, the dependence of the A exciton peak emission on composition will be compared to DFT calculations of the band gap later in section 4.5.2. From the optical spectroscopy data presented here, it is clear that the electronic structures of $Mo_{1-x}W_xS_2$ alloys can be tuned by varying the stoichiometry, however, due to the high exciton binding energy it is not possible to directly determine the electronic structure changes from the optical spectroscopy data.

4.4 Atomic structure

TEM is one of only a few direct methods in materials science capable of visualising the atomic structure of materials. Here, the ADF-STEM imaging technique was used to determine the atom coordinates in single-layer thick alloy flakes. Based on Z-contrast, Mo and W atoms are separately identified in these images. The aim was to determine whether the atomic distribution is ordered or random in the different $Mo_{1-x}W_xS_2$ alloys.

4.4.1 ADF-STEM images

A doubly corrected electron microscope with Schottky emitter (JEOL ARM200F) was operated at 80 kV in STEM mode to visualise the atomic structure of these $Mo_{1-x}W_xS_2$ alloys. A series of compositions (x = 0.22, 0.50 and 0.63) were imaged (Figure 4.8a to 4.8c respectively). As described in section 4.2, the flakes were exfoliated from bulk crystals, with the compositions of the bulk crystals previously confirmed via SEM-EDX and XPS, as discussed in section 4.3. Since the ADF images are sensitive to atomic number the brighter spots correspond to the heavier element, W (Z = 74) and the darker spots to the lighter element Mo (Z = 42) in the transition metal sublattice.

Two approaches, based Bloch wave propagation and the multi-slice principle, are used for simulations of high resolution CTEM and STEM images[84]. However, Bloch wave calculations require greater processing power, hence have more computing costs and are
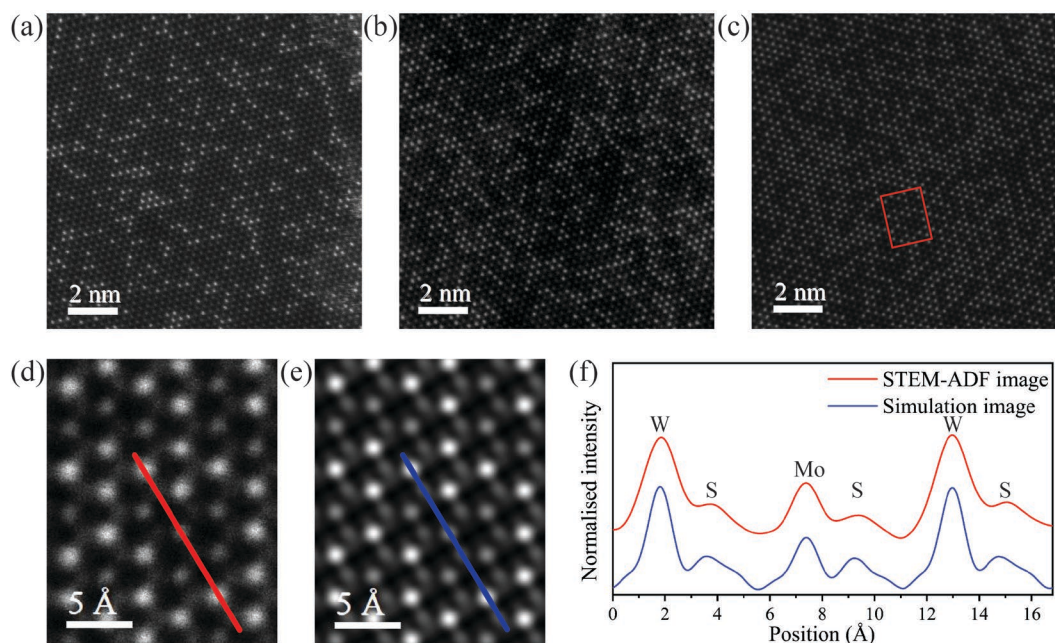
Figure 4.8. ADF-STEM images of $Mo_{1-x}W_xS_2$ single layers. (a-c) ADF-STEM images of $Mo_{1-x}W_xS_2$ single layers (x=0.22, 0.41 and 0.63). (d-e) At left magnified image of selected area as indicated in figure c (red box), at right simulated ADF image, respectively. (f) Intensity profiles along the red and blue line in experimental and simulated ADF images, respectively. The simulation was performed with clTEM (an OpenCL GPU-accelerated multi-slice program)[56] to compare with the experimental image, confirming the bright spots corresponds to W while dark ones to Mo.

less flexible compared to multi-slice programs[84]. Therefore, to confirm this identification based on the difference in contrast alone, quantitative simulation of the ADF images was performed using a multi-slice calculation with the clTEM software[131].

The atomic structure model used for the ADF image simulation is indicated by the light-yellow background in Figure 4.1a and the magnified image in Figure 4.9. The experimental ADF image, cropped from the red box in Figure 4.8c, is directly compared with the simulated image in Figures 4.8d and 4.8e, respectively. A close agreement between the experimental ADF profile (along the red line in Figure 4.8d) and the simulated data (blue line) is found (Figure 4.8f), confirming that the W and Mo atoms can be identified by their contrast alone, with the brighter dots corresponding to W and the darker to Mo.

Note that under these imaging conditions, the weaker intensity of the S chalcogen atoms is barely discernible in the experimental images. Nevertheless, the presence of S as well as Mo and W is confirmed from SEM-EDX results. Furthermore, from the XPS fitting the chemical environment of each element can be estimated giving, stoichiometric ratios of S to the sum of Mo and W are close to 2 in the bulk crystals. The ADF results are consistent with this XPS fitting, the W and Mo atoms share the metal sites, while the sulphur atoms are paired in the triangular lattice as expected.

4.4.2 Short-range order (SRO) analysis

Although by eye some of the images appear to show some ordering, determining whether this is significant requires detailed statistical analysis. To do this, the atom positions were determined by fitting and the intensity of metal atoms were clearly separated. Therefore, the Mo and W atoms were clearly identified as shown in Figure 4.10a and 4.10b. In this way, more than 100,000 atoms were analysed for several compositions. We concentrate here on the composition $Mo_{0.78}W_{0.22}S_2$, but the conclusions drawn from this analysis were equally valid in the other compositions studied.

Once the atom positions were determined, these were analysed to investigate the local ordering. Although previous studies have looked only at the nearest neighbour
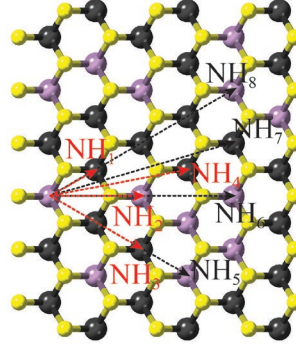
Figure 4.9. Define the nearest neighbours around a metal atom. Magnified image of the area in Figure 4.1 to explain how the 1st to 8th nearest neighbours/coordinate shells are counted.

distributions[56,60], ordering can extend beyond the nearest neighbour. Instead, following the approach developed by Warren and Cowley for the study of Cu_3Au[132,133], short-range order parameters were calculated as defined by:

$$P_{W-W,i} = m_W + m_{Mo}\alpha_i ,$$
4. 2

where $P_{W-W,i}$ is the probability that a W atom is found in the *ith* coordination shell from another W atom (see Figure 4.9), m_W and m_{Mo} are the concentration of W and Mo in the binary alloy, respectively, and α_i is the corresponding Warren-Cowley SRO parameter.

Rearranging equation (4.1), the SRO parameter can be calculated as follows:

$$\alpha_i = \frac{P_{W-W,i} - m_W}{m_{Mo}}.$$

$P_{W-W,i}$ was determined from the atom positions measured from the ADF-STEM images[123];

$$P_{W-W,i} = \frac{\sum_{j=0}^{6}(j \times N_{W-jW})}{6 \times N} \times \frac{1}{m_W} ,$$
4. 3

where N_{W-jW} are the number of W atoms surrounded by j W atoms (j = 0 to 6), and N is the total number of the transition metal atoms (Mo + W).

Figure 4.10c and 4.10d show examples of the calculation of $P_{W-W,i}$ for 1st and 2nd nearest neighbours, and the red numbers in the images are jW atoms around one W at 1st and 2nd nearest neighbours, respectively.

From the definition of the SRO parameters, when $\alpha_i \in (0,1)$ there is a tendency to form homo-atom ordering, while $\alpha_i \in (-1, 0)$ corresponds to a greater fraction of heteroatoms. When α_i is equal to or close to 0, the alloys are randomly distributed.

Taking Figure 4.10c and 4.10d as an example, Table 4.3 shows the analysis of the 1st and 2nd nearest neighbour distribution.
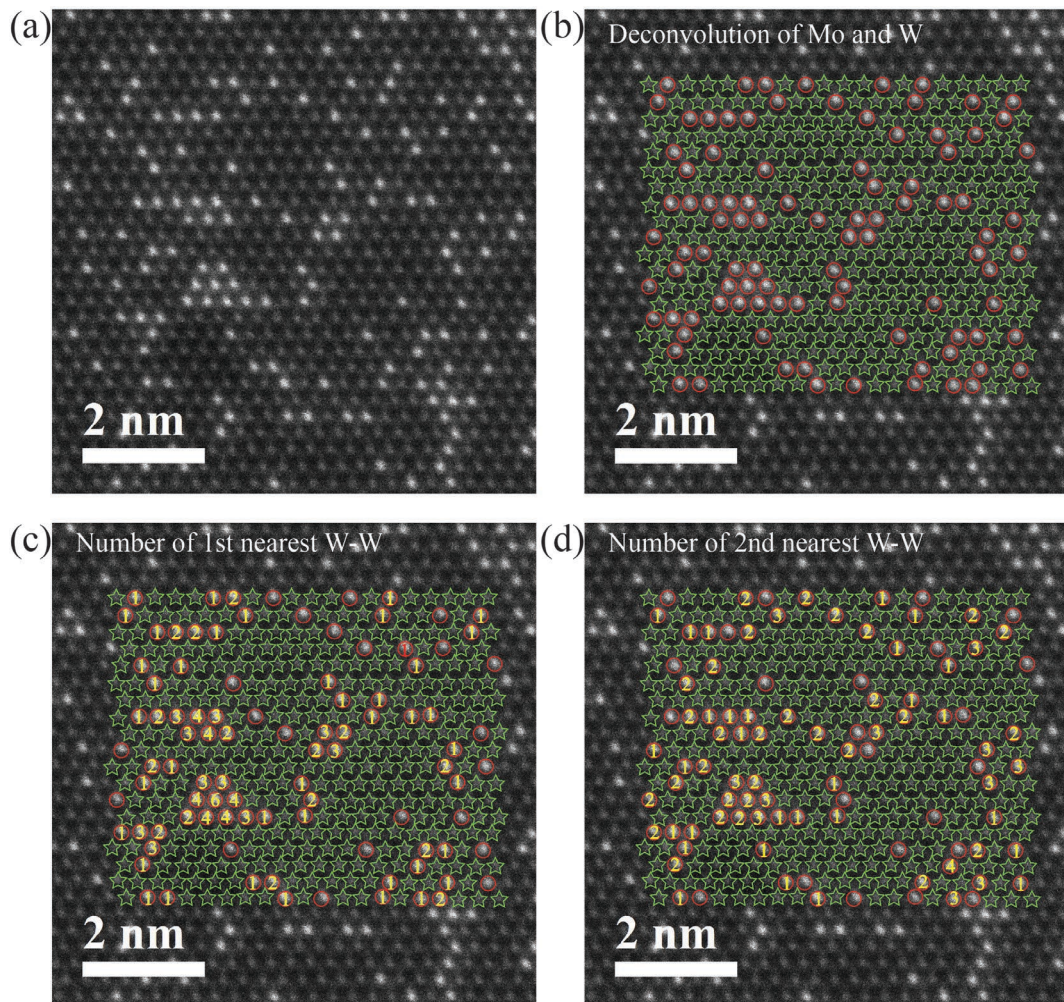
Figure 4.10. Schematic images show how to count the nearest neighbours. (a) ADF-STEM image of $Mo_{0.78}W_{0.22}S_2$ monolayer (part area of Figure 4.8a). (b) Image after deconvolution to assign W from Mo. (c - d) Schematic images to show how to count number of 1st and 2nd nearest W-W pairs, respectively.

From that analysis, $P_{W-W,1} = 0.26$ and $\alpha_1 = 0.05$. α_1 is close to 0, suggesting no segregation in the 1st shell. The same process was applied to calculate the other coordination shells, *e.g.* $P_{W-W,2} = 0.24$ and $\alpha_2 = 0.03$, *etc.*, these are shown later in Figure 4.12, along with a comparison to the results of theoretical models. To gain statistical significance, typically an area from the ADF-STEM images of order 120×120 metal atoms was analysed.

Table 4.3. Count of the 1st and 2nd nearest neighbour of a W atom surrounded by jW atoms.

W atoms surrounded by jW	Number of W atoms surrounded by jW	
	1st nearest neighbour ($i = 1$)	2nd nearest neighbour ($i = 2$)
N_{W-W}	41	29
N_{W-2W}	15	30
N_{W-3W}	10	10
N_{W-4W}	6	1
N_{W-5W}	0	0
N_{W-6W}	1	0

4.4.3 Monte Carlo Simulations

To gain insight into the significance of any ordering, or lack thereof, the group of Dr Nicholas Hine conducted Monte Carlo simulations. They constructed models consisting of 120×120 atoms in a single layer, with a random distribution of the W atoms in the Mo matrix (78% Mo matrix and 22% W atoms). Then, the growth process was simulated via Monte Carlo sampling of proposed site swaps to achieve an equilibrium of the system at a growth temperature of 800 K. The total energy of a given disordered configuration can be described as[134]

$$H(\sigma) = -\sum_{(i,j)} J_{i,j} \sigma_i \sigma_j , \qquad 4.4$$

in which $J_{i,j}$ is the pairwise interaction energy, and σ_i and σ_j are the energy of the configurations.

DFT calculations were used to estimate a realistic value for $J_{i,j}$ for the $Mo_{1-x}W_xS_2$ alloys. The formation energy can be calculated as[135]

$$E_F = E_T - E_T^{pure} + \sum_i m\mu_i ,$$ 4.5

where E_T is the total energy of a supercell, E_T^{pure} is the total energy of pure materials, μ_i is the chemical potential of dopants and m is the number of substituted cations.

The binding energy for an atomic configuration with m dopants, as shown in Figure 4.11a, can be calculated as[135]:

$$E_b = E_F(mW) - mE_F(1W)$$ 4.6

$$= E_T(mW) - mE_T(1W) - (m-1)E_T^{pure} .$$

Where $E_T(mW)$ is the total energy of a supercell with m substituted atoms in a desired configuration.
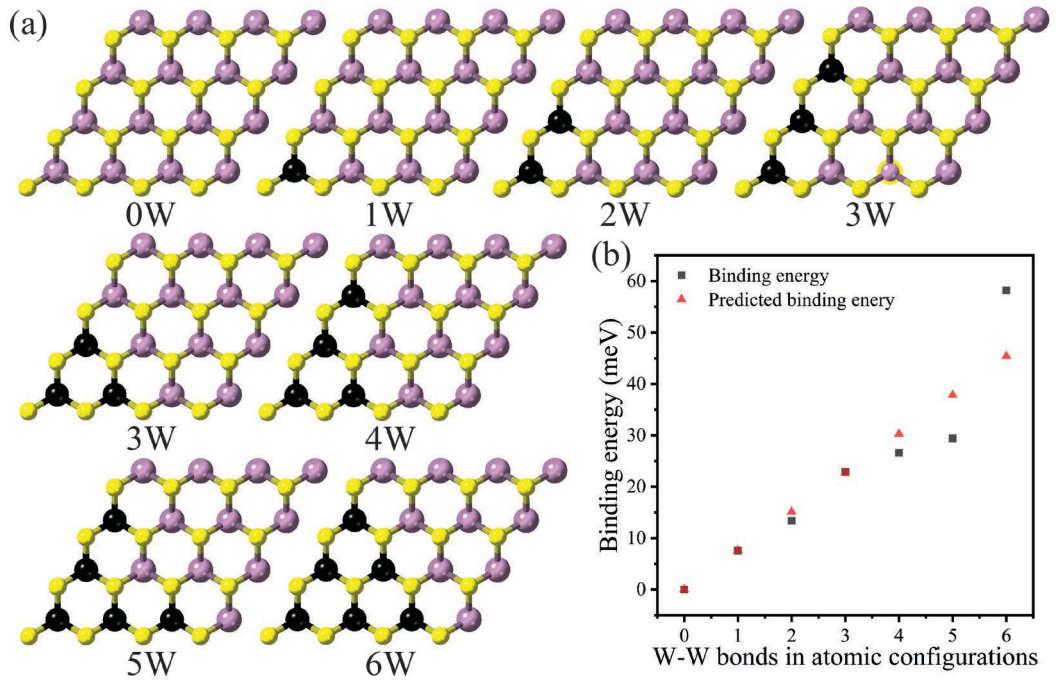
Figure 4.11. Atomic configuration selected for DFT calculations. (a) Different atomic configurations calculated/tested in DFT. (b) Comparison of DFT calculated and predicted binding energy using the average value.

Then the interaction energy for a pairwise interaction, J, can be estimated from the binding energy for a single W-W bond.

As shown in Figure 4.11b, various possible configurations of W atoms are reasonably well approximated by a 7.6 meV pairwise interaction. Note that this positive energy corresponds to an effective repulsion and so we expect clusters to be energetically unfavourable.

The Monte Carlo simulations allow the relationship between atomic interactions and atomic ordering to be probed. Figure 4.12 compares the Monte Carlo simulation images with varying interaction energies, J = -50, 7.6 and 50 meV, respectively, to the experimental ADF-STEM image. For the negative value of J, corresponding to an attraction, the Monte Carlo image in Figure 4.12a indicates the formation of W clusters while for the positive values, isolated individual W atoms are energetically favourable.
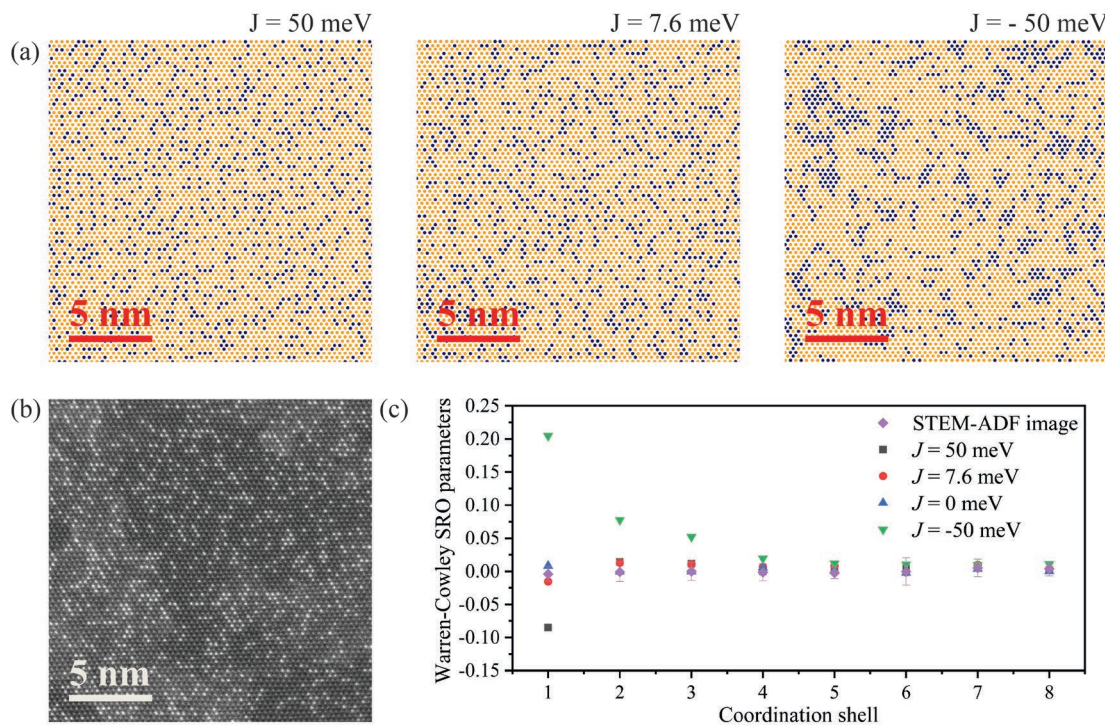
Figure 4.12. Comparison of SRO parameters of the Monte Carlo simulation and real ADF-STEM image. (a-c) Monte Carlo Simulations with binding energy J = -50, 7.6 and 50 meV, respectively. (d) ADF-STEM image of monolayer $Mo_{0.78}W_{0.22}S_2$. (e) Comparison of the Warren-Cowley SRO parameters calculated from the Monte Carlo simulations and from the experimental ADF-STEM image.

However, the atomic distribution of Monte Carlo image with interaction energy 7.6 meV in Figure 4.12b is visually similar to the experimental ADF-STEM image in Figure 4.12d.

To quantitatively analyse and compare the Monte Carlo simulations with the experimental ADF-STEM images, the SRO parameters from the 1st to 8th coordination shell were calculated and are shown in Figure 4.12e. For $J = - 50$ meV, the SRO parameters for the first few coordination shells α_1, α_2 and α_3 fall between $(0, 1)$ confirming the alloys tend to form segregations (homo-atom configurations) as expected from the visual observation. In contrast, the SRO parameter of the 1st coordination shell for $J = 50$ meV is between $(-1, 0)$ showing heteroatom distribution. The order parameters α_i for $J = 7.6$ meV, $J = 0$, and from analysis of the experimental images are all close to 0. This indicates that the W atoms are randomly distributed. The observed atomic configuration is thus indistinguishable from a random distribution and consistent with that expected for a system at thermal equilibrium.

The above analysis was carried out for the composition, $x = 0.22$. Similar processing was applied to all the alloy compositions and similar results were found. This analysis concludes that the W atoms are distributed randomly over the whole series of composition and the crystals are representative of thermodynamic equilibrium for this system under the chosen growth conditions.

4.5 Electronic structure

4.5.1 Valence band

To correlate the atomic and electronic structure, the VB structure was measured by ARPES. Data were acquired at the Spectromicroscopy beamline of the Elettra synchrotron (Italy) as described in Chapter 2. Since the measurements are surface sensitive, the as-grown bulk crystals were mounted flat onto a sample plate and cleaved in the ultrahigh vacuum (UHV) chamber immediately prior to analysis, to generate the clean surface required. Cleaving naturally results in exposure of the (002) planes to the beam, so that ARPES probes the electronic structure within the 2D layer direction.
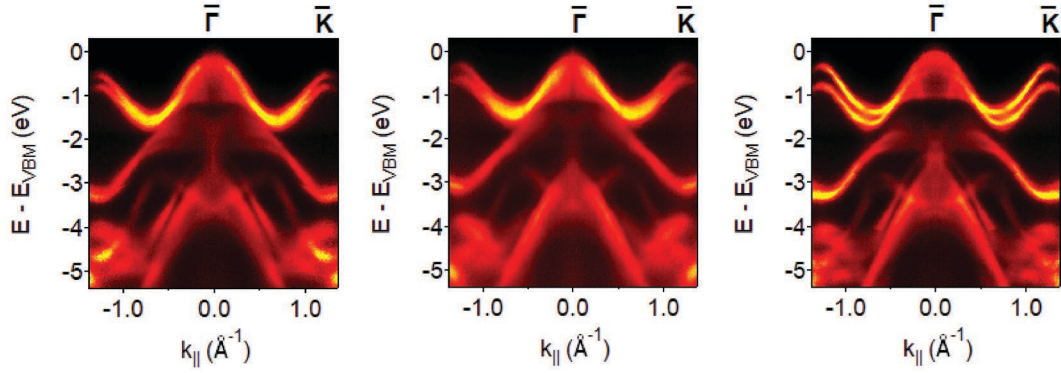
Figure 4.13. ARPES energy-momentum slices from bulk crystals of (from left to right) $Mo_{0.63}W_{0.37}S_2$, $Mo_{0.5}W_{0.5}S_2$ and $Mo_{0.29}W_{0.71}S_2$. The data are reflected around $\bar{\Gamma}$ for clarity.

Figure 4.13 shows an experimental energy-momentum slice of the valence bulk band dispersion along the $\bar{\Gamma}$ – $\bar{K}$ direction for three alloy compositions: $Mo_{0.63}W_{0.37}S_2$, $Mo_{0.5}W_{0.5}S_2$ and $Mo_{0.29}W_{0.71}S_2$. The slight broadening and intensity change of the bulk bands in Figure 4.13 can be attributed the k_z broadening effect[136]. Different from the case for monolayer, the final state of the excited photoelectron is intrinsically damped towards interior of the solid caused by the inelastic absorption and elastic reflection from the crystal potential in bulk crystals[136]. This confinement in the surface perpendicular coordinate is equivalent, by the uncertainty principle, to certain intrinsic broadening in k_z direction[136]. Then the state dispersion in the k_z direction will lead to an energy broadening of the bulk band[136].

As discussed in Chapter 2, it has been explained how the band parameters such as the SOC and bandwidth can be determined in the experimental ARPES, meanwhile the schematic in Figure 4.14 illustrates how band parameters can be determined from these dispersions. The effective mass was calculated by fitting a parabola to the dispersion near the corresponding band edge.

The qualitative trends are apparent by visual inspection of the ARPES spectra: as the W content increases, the splitting between the upper valence bands near K (VB SOC) become larger; the band width increases and effective mass decreases.

To quantitatively evaluate the evolution of the band structure with composition, measurements were performed on all the compositions (x = 0.22, 0.37, 0.49, 0.71, 0.87

and 1) and band parameters extracted quantitatively and directly by fitting the ARPES spectra. The derived parameters are between those previously measured for the pure materials MoS_2 and WS_2[137,138]. The data are presented in Figure 4.15, and compare to first principles calculations below.

4.5.2 Comparison of experimental data, DFT and VCA calculations

DFT calculations for a series of $Mo_{1-x}W_xS_2$ monolayer flakes were performed by the group of Dr Nicholas Hine.

Lattice constants of the pure materials MoS_2 and WS_2, were optimizing using the plane-wave DFT package CASTEP[139] with the generalized gradient approximation (GGA) of Perdew, Burke and Ernzerhof (PBE)[140] and a cut-off energy of 425 eV. The lattice constant of MoS_2 was found to be similar to that of WS_2 with less than 0.3% difference: this difference was neglected and a lattice constant of 3.18 Å was used for all subsequent simulations of $Mo_{1-x}W_xS_2$.

For the alloy calculations, the linear-scaling DFT package ONETEP[141] was employed. This uses a representation of the single-particle density matrix in terms of a minimal number of support functions, denoted non-orthogonal generalized Wannier functions (NGWFs). Here, a cut-off energy of 1200 eV and a cut-off radius of $10a_0$ were used (where a_0 is the lattice constant). The PBE functional was employed with projector-augmented wave (PAW)[142,143] potentials from the JTH library[144].

The electronic structure calculations were performed on an 8x8x1 supercell model constructed with random configurations of various dopant concentrations. Geometry optimization was performed for each structure, to a force tolerance of 0.1 eV/Å. Due to the large supercell, the band structure derived from these simulations above is heavily folded. Therefore, for direct comparison to the ARPES spectra, the effective band structure in a primitive cell was calculated. To do this, a spectral function unfolding method was used[56,145], the adaption of which to the NGWF representation is described in Ref. [146].

For comparison, electronic structure calculations were also made within the virtual crystal approximation (VCA)[147,148], where fractional atom compositions are considered

within the primitive cell of pure materials. PAW datasets representing the W and Mo potentials mixed in the appropriate ratio were constructed using the 'virtual' tool within the Quantum Espresso package[149,150].

Figure 4.14a shows a spectral function calculation for monolayer $Mo_{0.5}W_{0.5}S_2$. The dispersion is similar for the pure materials, with the upper VB being spin degenerate at a local maximum at **Γ** and dispersing to the spin-split and spin polarised VBM at **K**, as discussed in Chapter 1. The spin splitting at the CBM, also at **K**, is more complicated. As shown schematically in Figure 4.14b, the order of spin polarisation of the bands changes from MoS_2 to WS_2, effecting their optical properties such that the lowest energy exciton is dark for WS_2 and bright for MoS_2[124].

Figure 4.15 compares the band structure parameters measured from the experimental data to those calculated by ONETEP and VCA simulations. Figure 4.15a compares the evolution with W content of the PL emission peak energies to the predicted band gaps. As illustrated in Figure 4.7b and 4.15a, the dependence of PL peak energy on composition is non-linear, with a bowing effect in the evolution of the A exciton emission peak energies. The band gap calculated by ONETEP is qualitatively similar in that with
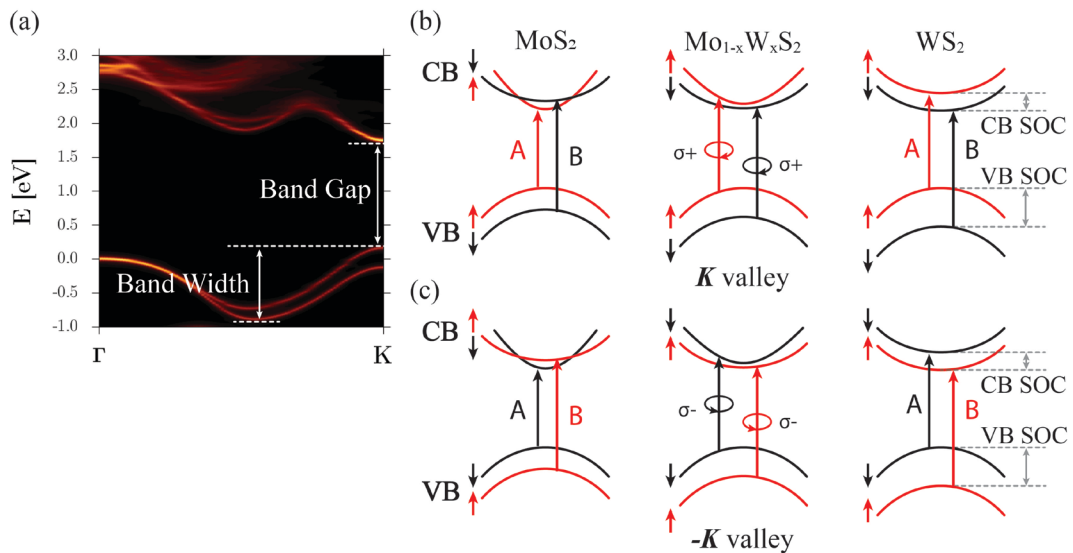
Figure 4.14. Schematic of the evolution of bands at **K** valley from MoS_2 to WS_2 monolayer flakes. (a) Spectral function calculation for $Mo_{0.5}W_{0.5}S_2$ monolayers, the relevant measurements for some of the band parameters are overlaid. Schematic diagram of the band-edge structure in the (b) **K** and (c) **-K** valley.

increasing x it first decreases and then increases, although the composition values for the PL minimum energy are different between the experimental and calculated one ($x = 0.20$ vs $x = 0.60$). The magnitude of the band gaps from VCA is similar to ONETEP calculations, but the VCA band gaps decrease monotonically with increasing x. The differences between the PL emissions and the predicted band gaps can be explained from the following aspects. Firstly, the predicted band gaps refer to electronic band gaps derived from the energy difference between the VBM and the CBM. However, the optical spectroscopy measurements are from excitons with high binding energy. The difference between the ONETEP and PL data suggests a consistent decrease in exciton binding energy as the W content increases. Secondly, some of the difference can be attributed to the change in order of the conduction bands, as shown schematically in Figure 4.14b. The PL emission is from the A exciton emission (bright exciton) in the **K** valley. For $x = 0$, i.e. MoS_2 this corresponds to the VBM and CBM states, but at $x = 1$, WS_2, the order has changed and the bright A exciton emission comes from the second-lowest lying CB, corresponding to the CB SOC greater in energy than CBM (for predicted values see Figure 4.15c). There, the difference can also be attributed to the spin polarisation and dispersion of SOC splits in their CB. Furthermore, compared to the experimentally determined electronic band gaps, the predicted values from DFT calculations are normally significantly underestimated[22].

ARPES provides a more direct and visual measurement of the VB dispersion, allowing easier comparison to calculated spectra than was possible by looking at A-B exciton emission. We use this here to directly study the changes in SOC with alloying. This direct measurement avoids controversies over the interpretation of the previously reported optical spectroscopy data (such as that the spin splitting in CB can be ignored and that the binding energies of A and B excitons are the same)[124]. Due to the weak k_z dispersion of the upper most VB at **K**, the key features of the spectra in that region are similar for bulk and monolayer samples as has been reported experimentally[97,105] and theoretically[97]. This was also confirmed by our measurements for these samples, the VB SOC splitting for monolayer WS_2 was found to be (450 ± 30) meV[151] while the value for bulk crystals is (458 ± 10) meV. Due to the difficulty of preparing monolayer TMD samples for ARPES, we concentrate instead on ARPES from cleaved crystals.
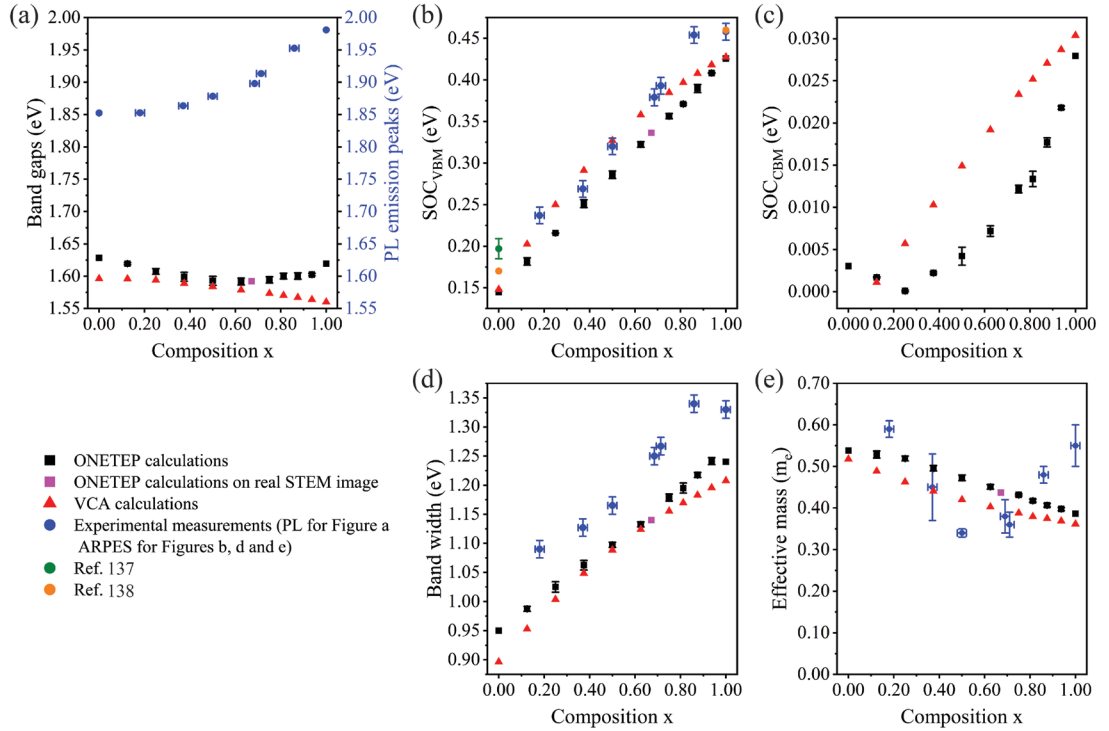
Figure 4.15. Comparison of experimental data and ONETEP calculations. Comparison of band structure parameters determined from experimental data and DFT calculations, as a function of the composition x in $Mo_{1-x}W_xS_2$: (a) the evolution of PL emission peak energy and band gaps with x; SOC at the valence band (VB) edge (b), and at the conduction band edge (c) at **K**; (d) band width; and (e) effective masses at the **K** point in the upmost VB.

The VBM SOC splitting of the $Mo_{1-x}W_xS_2$ single crystals measured by ARPES (blue data points) is compared to those calculated by ONETEP (black) and VCA (red) simulations in Figure 4.15b. Literature values for MoS_2 crystals, taken from Ref. 137 and 138, and WS_2[138] are also shown. For the WS_2, our measured value of (458 ± 10) meV is consistent with the literature within the error bar, indicating our values are reasonable. For our experimental results, it is clear that within the error bars the SOC splitting of the VB increase linearly as a function of the W content. For comparison, the VB splits calculated from ONETEP spectra from monolayer supercells with disordered atomic configurations are also shown in Figure 4.15b. The linear trend is in agreement with that of ARPES, however, the experimental values are consistently around 50 meV higher than that predicted by ONETEP. The SOC splitting of the VB calculated from the VCA simulation are also presented in Figure 4.15b. These are similar in magnitude to the experimental measurements but show a non-linear dependence on composition, with a

slight bowing. We note that a ONETEP simulation was also made using the atom positions determined from the STEM image in Figure 4.10. The band parameters for this simulation are shown as the purple data point in the graphs in Figure 4.15 and are consistent with the other ONETEP simulations. The band width (as indicated by white arrow in Figure 4.14a), Figure 4.15d, follows similar trends to the spin-orbit splitting of the VB: the agreement between the experimental data and the ONETEP data is excellent, other than a systematic offset between the two; and the VCA data shows a bowing that is not present in either the ONETEP or experimental data.

The ARPES spectra do not give information about the CB as they only probe the occupied states. However, the CB SOC can be extracted from the DFT spectral functions and this is plotted as a function of composition in Figure 4.15c. The magnitude is much lower than the VB SOC splitting. At small x, close to pure MoS_2, the order of the conduction bands change, see Figure 4.14b. Hence the SOC splitting initially decreases to zero and then increases with x. Although the data are very similar for the pure materials, the change in CB order occurs at different compositions in ONETEP and VCA calculations. The close agreement between the ONETEP and experimental data for the other band parameters gives confidence in the ONETEP CB predictions as well.

Figure 4.15e shows the comparison of the evolution of the VB effective mass calculated from ARPES spectra, the ONETEP and VCA calculations. It is difficult to accurately determine the effective mass from the ARPES spectra, the uncertainties are large and there are no clear trends. The DFT predictions are in fair agreement with the previous values of effective masses calculated by LDA[152] with small systematic differences between the ONETEP and VCA that are less than $0.05m_e$ (m_e is the electron mass). Moreover, the simulated effective masses in VBM for MoS_2 and WS_2 monolayer are $0.54m_e$ and $0.39m_e$ from ONETEP, while $0.52m_e$ and $0.36m_e$ from VCA, respectively. These are fairly in agreement with the results from Ref. 124 that the effective masses in VBM is $0.54m_e$ and $0.35m_e$ for MoS_2 and WS_2, respectively, indicating the DFT and VCA calculations are reasonable. From the DFT calculations it is clear that the effective mass decreases monotonically with x, consistent with the increasing curvature of the bands as demonstrated by the increasing band widths. This decrease in effective mass is also consistent with the decrease in exciton binding energy inferred from the difference between the PL and band gap trends.

4.6 Spin-valley locking

As explained in Chapter 1, inversion symmetry breaking leads to the valley-dependent optical selection rules for interband transitions at the **K** points for monolayer MX_2. While in the valley band, because of the large valley contrasting spin splits, valley and spin can only be flipped simultaneously to conserve energy[42,153]. Therefore, inversion symmetry breaking together with strong spin-orbit splitting leads to the spin-valley locking effect in monolayer MX_2. This theoretical prediction has been confirmed experimentally by circularly polarized PL measurements on monolayer MoS_2[41]. For these alloy samples, the spin-orbit splitting in the CB is reduced to less than the disorder potential across the alloy, suggesting the spin-valley locking could be lost.

Optical spectroscopy measurements on an exfoliated heterostructure was performed to test whether spin-valley locking was retained. An optical image, and schematic, of the
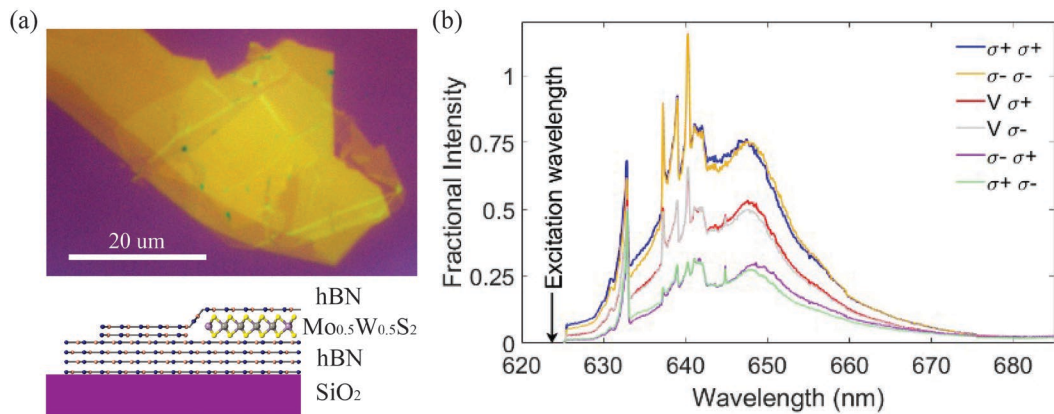
Figure 4.16. Polarization resolved PL spectra of a hBN encapsulated $Mo_{0.5}W_{0.5}S_2$ monolayer sample. (a) Top, optical image of hBN encapsulated $Mo_{0.5}W_{0.5}S_2$ monolayer flake. Bottom, schematic cross-section of the sample (Dark blue and pastel red atoms represent nitrogen and boron, respectively). (b) Polarization resolved PL spectra of the encapsulated sample taken at 4 K. σ+ and σ- correspond to light with spin parallel and antiparallel to the direction of the incoming beam. V corresponds to vertical linear polarization i.e. has spin $((σ+ + σ-))/\sqrt{2}$. The pairs of spectra with the same incident polarization have been scaled by the sum of their intensities at 646 nm to provide an indication of the fraction of the intensity in each polarization. No significant variation in the sum of the intensities was observed. Optical spectroscopy was performed by Professor David Smith's group in Southampton, the sample was fabricated in Warwick.

sample is shown in Figure 4.16a. A monolayer flake of $Mo_{0.5}W_{0.5}S_2$ was encapsulated in hBN, to improve the quality of the spectroscopy data. Professor David Smith's group, at the University of Southampton, then performed low-temperature PL spectroscopy. The measurements were performed in backscattering geometry with a 625 nm laser and a sample in vacuum at 4 K. A quarter wave plate (Thorlabs AQWP05M-600) was placed before the objective lens so that in the rest of the optical system the input and output polarisations corresponded to vertical and horizontal linear polarisations, respectively. The output polarisation was determined using a linear polariser (Thorlabs LPVIS100) and a half wave plate (AHWP05M-600) used to ensure a constant input polarisation for the spectrometer. The spectrometer used was a Princeton Instruments TriVista 555 with a liquid nitrogen cooled CCD.

Figure 4.16b shows the polarization-resolved PL spectra on the stack of hBN/$Mo_{0.5}W_{0.5}S_2$/hBN. The PL spectra in Figure 4.16b show clear circular dichroism: that is, the σ+ light with spin parallel to the direction of the incoming beam corresponds to the interband transitions at the **K** valley as explained in Figure 4.14, while the σ- beam with opposite helicity couples to the transitions at the **-K** valley. The PL spectra are plotted with normalised intensity to give a direct comparison of the excitations with different polarisations. The degree of circular polarisation can be quantified via P = (I(σ+) - I(σ-))/(I(σ+) + I(σ-)), where I(σ±) is the intensity[41]. From Figure 4.16b, the polarisation degree is around P = 0.47 under σ+ excitation, while P = -0.47 under σ- excitation. Moreover, Figure 4.16b also shows that excitation with vertical linear polarisation (spin $(\sigma+ + \sigma-)/\sqrt{2}$) has an equal amount of σ+ and σ- circular components, i.e. the PL for excitation with vertical linear polarisation shows the same intensity for the transitions at the **K** and **-K** valleys. The results are fully consistent with the predictions/expectations from the optical selection rule, showing that the spin-valley locking effect is retained for the monolayer alloys, even though the DFT calculations indicate that at intermediate compositions the SOC in the CBM is less than the disorder potential in the alloys. This suggests that locally, over the lengthscale of the exciton, the spin texture is retained and hence alloying for engineering the band gap and SOC is possible.

4.7 Conclusions

In summary, we have visualised the atomic structure of $Mo_{1-x}W_xS_2$ alloys with atomic resolution STEM images and quantitatively analysed their elemental distributions. By comparison with Monte Carlo simulations and first principles calculations, we find that the distributions are quantitatively similar to these expected by thermodynamic considerations – i.e., essentially random. Band structure measurements and calculations were undertaken for the same set of alloys, and compared to PL spectra. Band parameters were extracted and compared for both the theoretical and experimental results. The comparison showed that alloying can be used for band structure engineering, tuning the band gap, effective mass, SOC and even the order of the bands across the alloy compositions. A close match was found between the experimental results and the ONETEP calculations, which used large supercell sizes. This resolved an ambiguity from previous reports, showing that the VB SOC changes linearly with composition without bowing, and demonstrates the importance of careful simulations. Optical spectroscopy of an exfoliated monolayer heterostructure showed that spin-valley locking is retained even when the CB SOC is apparently less than the disorder potential. Combined, these results demonstrate the potential of alloying for spin-orbit engineering of 2D semiconductors for valleytronic and spintronic applications.

Chapter 5: Atomic and Electronic Structure of Ordered Alloys

5.1 Introduction

As described in Chapter 4, it has been confirmed that alloying MX_2 (M = Mo, W, Nb and Ta; while X = S and Se) can provide additional freedom to tune the band structure, giving flexible control over the bandgap and spin-orbit splitting[39,56,106,154,155]. In contrast with the random alloy systems that have been studied most so far, ordered alloying would present opportunities for a more refined band engineering[39]. Although recently a group has reported ordering in small grains of polycrystalline $Mo_{1-x}W_xS_2$ mono-flakes synthesised via CVD[60], ordering over large scale in these alloys has been rarely observed.

This chapter will focus on Nb-containing alloys, synthesised via CVT, the same growth technique used for the random alloys $Mo_{1-x}W_xS_2$ presented in Chapter 4. ADF-STEM images of the $Nb_{0.1}W_{0.9}S_2$ demonstrate the formation of an alloy ordered along certain crystallographic directions in monolayer crystal flakes, contradicting previous reports[60]. Linear scaling DFT calculations performed by our collaborators for the $Nb_{0.1}W_{0.9}S_2$ system reveal that it is energetically favourable to form ordered uniformly
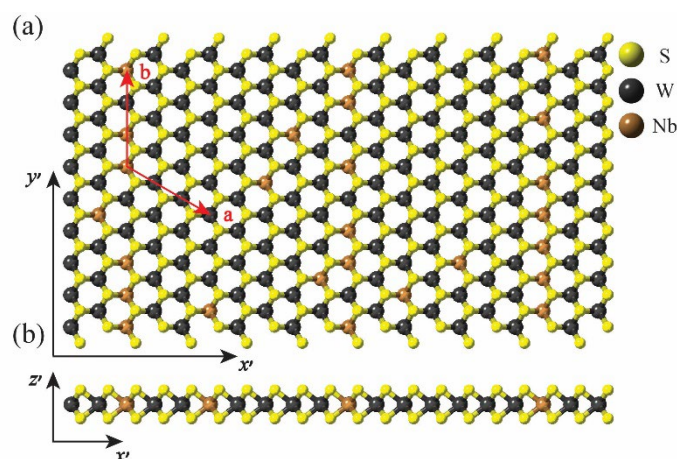
Figure 5.1. Atomic structure of a $Nb_{0.1}W_{0.9}S_2$ monolayer. (a) Top view of a $Nb_{0.1}W_{0.9}S_2$ monolayer. Brown, dark grey and yellow atoms represent niobium, tungsten and sulphur, respectively. (b) Side view of the $Nb_{0.1}W_{0.9}S_2$ monolayer.

113

spaced lines of Nb atoms at the growing fronts of the flakes. Since the ordering occurs along distinct crystallographic directions, ARPRS was used to analyse the anisotropic optical properties of this material. To directly study the electronic structure, ARPES measurements were carried out on Nb-containing MX_2 alloys. The presence/absence of optical band gaps in these Nb-containing alloys was investigated by PL. Further investigations into the local electronic structure were carried out using highly spatially resolved EELS in the low loss region.

5.2 Synthesis of the single crystals and calibrations

$Nb_{0.1}W_{0.9}S_2$ and $Nb_{0.17}W_{0.83}Se_2$ single crystals were synthesised via CVT. As described in Chapter 3, the synthesis process for both alloys was similar, with slight differences in the growth parameters (*e.g.* source temperature, growth temperature and transport agent, *etc.*)[106,114]. For $Nb_{0.1}W_{0.9}S_2$ single crystals, the temperature of the source zone and growth zone were slowly heated to 1050°C and 950°C respectively with 70°C/h rate first, then these temperatures were maintained for 20 days. Iodine was used as the transport agent with a flux of 5 g/cm^3. The source and growth temperatures of $Nb_{0.17}W_{0.83}Se_2$ single crystals were set to 1000°C and 900°C[114,156], respectively, with these temperatures again maintained for 20 days. The flux of iodine was 3 g/cm^3 for this growth.

The $Nb_{0.1}W_{0.9}S_2$ and $Nb_{0.17}W_{0.83}Se_2$ single crystals grown by PVT are small and thin. An optical image of a typical 0.6×0.4 mm $Nb_{0.1}W_{0.9}S_2$ single crystal is presented in Figure 5.2. SEM-EDX analysis was used to quantify the stoichiometry of the alloys and calibrate their compositions. Figure 5.2 compares the Nb-containing WS_2 alloy EDX spectrum with pure WS_2 single crystals, with the atomic percentages listed in the table. The spectra comparison in Figure 5.2 shows the same S K_α line peak intensities whilst the W M line peak is slightly lower for $Nb_{0.1}W_{0.9}S_2$ and WS_2. An additional small peak around 2.16 eV is present in the $Nb_{0.1}W_{0.9}S_2$ (see magnified area of the spectra in Figure 5.2), that can be attributed to the Nb L_α line. Therefore, the as-grown crystals contain

Atomic percentage						
Spectrum	W	Error	Nb	Error	S	Error
WS_2	0.67	0.01	0	0	0.33	0.01
$Nb_{0.1}W_{0.9}S_2$	0.60	0.01	0.07	0.03	0.33	0.01
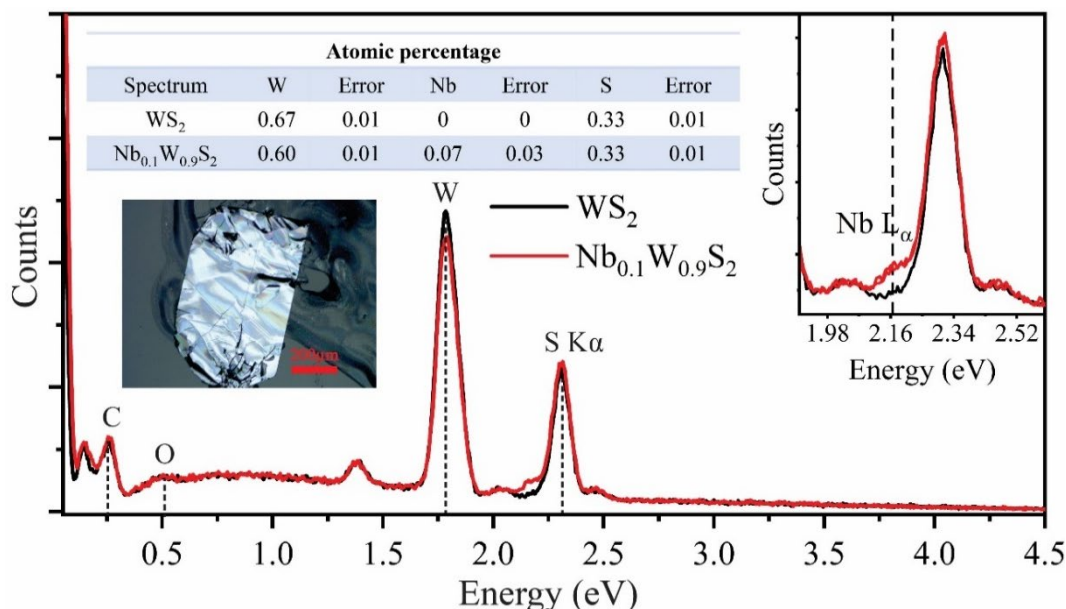
Figure 5.2. SEM-EDX spectra on $Nb_{0.1}W_{0.9}S_2$ (red) and WS_2 (black) single crystals. Insert: magnified region of the EDX spectra revealing the presence of Nb in the alloy sample. The table displays the composition (atomic percentage) determined from each spectrum. The optical image shows the morphology of the as-grown $Nb_{0.1}W_{0.9}S_2$ single crystals.

around 10% Nb – this is consistent with the compositions determined from atomic resolution imaging below.

5.3 Atomic structure

ADF-STEM images were used to visualise the atomic structure of $Nb_{0.1}W_{0.9}S_2$ and $Nb_{0.17}W_{0.83}Se_2$ monolayers. Since this type of image is sensitive to the atomic number (Z), the Nb and W atoms are easily identified. ADF-STEM image analysis allows direct visualisation of the Nb/W atomic distribution in the alloys. Once the atom positions are determined, a more detailed analysis of the ordering/randomness can be performed by statistical Warren-Cowley SRO analysis, to quantitatively determine the ordering parameter in the atomic structure of these alloys.

5.3.1 STEM images

5.3.1.1 ADF-STEM images of $Nb_{0.1}W_{0.9}S_2$ monolayer

ADF-STEM images were recorded to visualise the $Nb_{0.1}W_{0.9}S_2$ monolayer atomic structure. An example of these images is shown in Figure 5.3a. The transition metal sublattice contains two different type of atoms. In this sublattice the brighter dots correspond to the heavier element, W ($Z = 74$), and the darker to the lighter element, Nb ($Z = 41$). Notice that the S sublattice is barely visible under these imaging conditions. The images show a visible order (vertical dark lines) in the $Nb_{0.1}W_{0.9}S_2$. The ordering is clearly detectable by eye in this alloy in the electron microscopy images. Nevertheless, likewise to Chapter 3, to confirm the identification by contrast, the intensity profiles of the ADF images were simulated quantitatively via the clTEM software[131] using the input atomic structure model presented in Figure 5.3b (middle). This model contains Nb atoms in a vertical line in the corresponding transition metal sublattice (brown atoms in the model). The simulated image is presented on the right hand side of Figure 5.3b. Experimental and simulated images are very similar at first glance. Further quantitative comparison was carried out by comparing the intensity profiles along the blue and red lines in experimental and simulated ADF images respectively (Figure 5.3c). The two
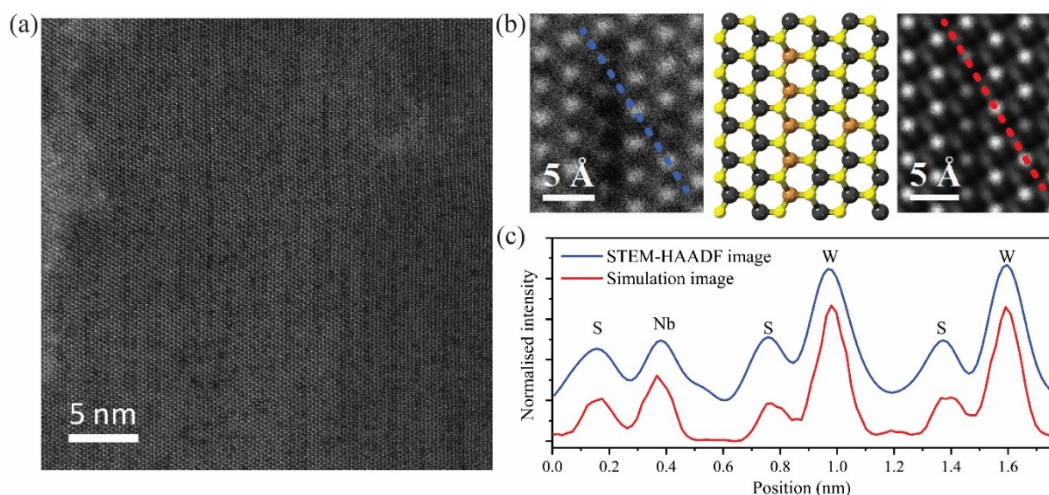
Figure 5.3. ADF-STEM images of a $Nb_{0.1}W_{0.9}S_2$ monolayer. (a) ADF-STEM images of a $Nb_{0.1}W_{0.9}S_2$ monolayer over a large area. (b) (left) magnified image of a selected area in (a), (middle) atomic model of the selected area, (right) simulated ADF image. (c) Intensity profiles along the red and blue lines in experimental and simulated ADF images in (b), respectively.

intensity profiles are in close agreement. Since the difference in intensity between W and Nb is large, it is reasonable to use the contrast alone for identifications.

Based on the experimental observations from ADF-STEM imaging of $Nb_{0.1}W_{0.9}S_2$ monolayers (Figure 5.3a), it is obvious that the Nb atoms distribution within the W matrix is not random.

1. The Nb atoms tend to form atomic lines. Different lengths of Nb ordered atomic lines were observed, ranging from 3 to 6 atoms.
2. The majority of the Nb atomic lines occur along one of the three equivalent crystallographic directions ([100], [010] and [110]).
3. Nb ordered atomic lines tend to be separated by several unit cells of WS_2.

5.3.1.2 ADF-STEM images of $Nb_{0.17}W_{0.83}Se_2$ monolayer

Similarly, a $Nb_{0.17}W_{0.83}Se_2$ monolayer was analysed following the procedure described above. Figure 5.4a shows an ADF-STEM image of the $Nb_{0.17}W_{0.83}Se_2$ alloy. Note that the Se has a higher atomic number than S (34 vs 16), therefore all the atoms
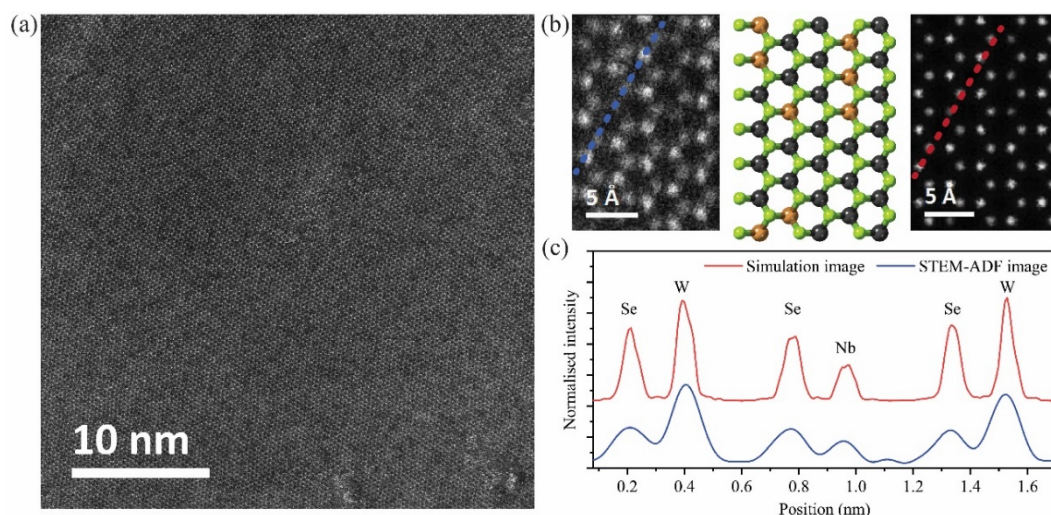
Figure 5.4. ADF-STEM images of a $Nb_{0.17}W_{0.83}Se_2$ monolayer. (a) ADF-STEM images of a $Nb_{0.17}W_{0.83}Se_2$ monolayer over a large area. (b) (left) magnified image of a selected area in (a), (middle) atomic model of the selected area, (right) simulated ADF image. (c) Intensity profiles along the red and blue lines in experimental and simulated ADF in (b), respectively.

are visible in this sample, but the same identification method could be applied to separately identify the Nb and W atoms in $Nb_{0.17}W_{0.83}Se_2$.

5.3.2 Warren-Cowley SRO parameters analysis

Although at first glance there is a clear difference in the atomic distribution between the $Nb_{0.1}W_{0.9}S_2$ and $Nb_{0.17}W_{0.83}Se_2$, with local Nb-ordering observed in the former, the significance of this feature requires detailed statistical analysis. Here, a similar SRO analysis approach is followed to the one described in section 4.4.2. Thus, according to the equation 4.2 and 4.3, the Warren-Cowley SRO parameters, i.e. $P_{W-W,i}$ and α_i can be calculated. The structure model shown in Figure 5.5a, schematically indicates with arrows the 1st to 8th nearest neighbours around a metal atom. Figure 5.5b shows a quantitative comparison of the α_i for $Nb_{0.1}W_{0.9}S_2$ and $Nb_{0.17}W_{0.83}Se_2$ monolayers from their 1st to 8th coordination shells. For $Nb_{0.17}W_{0.83}Se_2$ all the coordination shells (α_1 to α_8) show negligible SRO parameters, $\alpha_i \sim 0$, indicating that the Nb is randomly distributed in these shells. On the other hand, for the $Nb_{0.1}W_{0.9}S_2$ monolayer, there are two main groups of SRO parameters:

(i) 1st, 3rd, 5th and 8th coordination shells (α_1, α_3, α_5 and α_8) fall between $0 < \alpha_i < 1$, indicating Nb atoms at these shells tend to form homo-atoms (segregations).
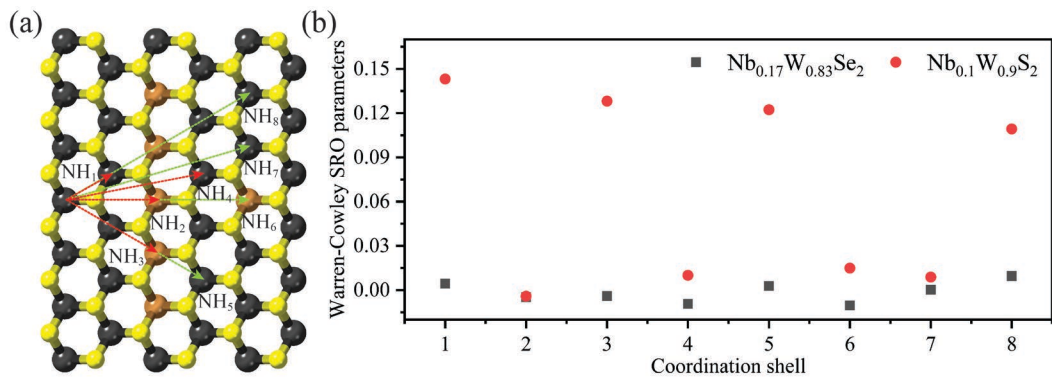
Figure 5.5. Statistical short-range order (SRO) analysis of the $Nb_{0.1}W_{0.9}S_2$ structure. (a) Modelled $Nb_{0.1}W_{0.9}S_2$ structure with arrows schematically indicating 1st to 8th nearest neighbours around a metal atom. (b) Comparison of the Warren-Cowley SRO parameters calculated from the $Nb_{0.1}W_{0.9}S_2$ and $Nb_{0.17}W_{0.83}Se_2$ monolayers shown in Figure 5.3 and 5.4, respectively.

(ii) 2nd, 4th, 6th and 7th coordination shell (α_2, α_4, α_6 and α_7) are close to 0, indicating Nb atoms distribute randomly at these shells.

However, the result of this SRO analysis differs from the visual observations of the $Nb_{0.1}W_{0.9}S_2$ STEM image which clearly shows single atomic lines along just one of the equivalent directions.

To quantitatively analyse the structure precisely, a vector pair correlation $\boldsymbol{\alpha} = (\alpha_{i,1}, \alpha_{i,2}, \alpha_{i,3})$ based on its hexagonal structure was introduced. This allows the short-order range to be analysed along principal crystallographic directions[60,132]. $\alpha_{i,1}$ is along [100] and [$\bar{1}$00]; $\alpha_{i,2}$ is along [010] and [0$\bar{1}$0]; $\alpha_{i,3}$ is along [110] and [$\bar{1}\bar{1}$0]. Thus, the Warren and Cowley SRO parameters can be rearranged and expressed as follows,

$$\alpha_{i,d} = \frac{P_{Nb-Nb,i,d} - m_{Nb}}{m_W} \qquad 5.1$$

where $P_{Nb-Nb,i,d}$ is the probability that a Nb atom is found in the *ith* nearest neighbour along direction d (d = 1, 2 and 3 based on its hexagonal structure). The Warren-Cowley SRO parameters were determined along the [100], [010] and [110] directions from the 1st to 8th nearest neighbours ($\alpha_{i,1}$, $\alpha_{i,2}$ and $\alpha_{i,3}$) as schematically indicated in Figure 5.6a. The probability $P_{Nb-Nb,i,d}$ is defined by the following expression:

$$P_{Nb-Nb,i,1} = \frac{\sum_{j=0}^{2}(j \times N_{Nb-jNb,1})}{2 \times N} \times \frac{1}{m_{Nb}} \qquad 5.2$$

where $N_{Nb-jNb,1}$ are the number of Nb atoms surrounded by j Nb atoms (j = 0 to 2) along [100] and [$\bar{1}$00], N is the total number of the metal atoms.

These Warren-Cowley SRO parameters along the equivalent crystallographic directions were determined for both $Nb_{0.1}W_{0.9}S_2$ and $Nb_{0.17}W_{0.83}Se_2$ alloys from ADF-STEM images, providing a quantitative analysis and comparison. Here again, by the definition of the SRO parameters, when $0 < \alpha_{i,d} < 1$ there is a large fraction of homo-atoms (segregations), while if $-1 < \alpha_{i,d} < 0$ the Nb atoms tend to separate from one another. When $\alpha_{i,d}$ is close to 0, the Nb atoms are randomly distributed in the alloys. For the defined vector of SRO parameters, $\boldsymbol{\alpha} = (\alpha_{i,1}, \alpha_{i,2}, \alpha_{i,3})$, when $\alpha_{i,1}$, $\alpha_{i,2}$ and $\alpha_{i,3}$ are

all close to 0, the alloys are random distributed. When one of the three components falls between 0 and 1, there is tendency to form segregations in that direction.

For $Nb_{0.1}W_{0.9}S_2$ monolayers, the ADF-STEM image in Figure 5.3a visually shows atomic lines along one of the equivalent directions [100], [010] and [110]; the SRO analysis is in agreement with this observation. Figure 5.6b shows the Warren-Cowley SRO parameters from the 1st to 8th nearest neighbours in the three non-equivalent directions: $\alpha_{i,1}$, $\alpha_{i,2}$ and $\alpha_{i,3}$. Along [010] (and $[0\bar{1}0]$), all the SRO parameters fall between (0, 1) confirming the Nb atoms tend to form line segregations along this direction. Furthermore, the parameters decrease from the 1st to 8th nearest neighbour along $\alpha_{i,1}$ direction indicating short segregations are more favourable than long ones. However, along $\alpha_{i,2}$ and $\alpha_{i,3}$ direction, the order parameters of the 1st to 8th nearest neighbours are all close to 0, therefore the Nb atoms are randomly distributed in these two directions. This is consistent with the visual observations listed in section 5.3.1.a.
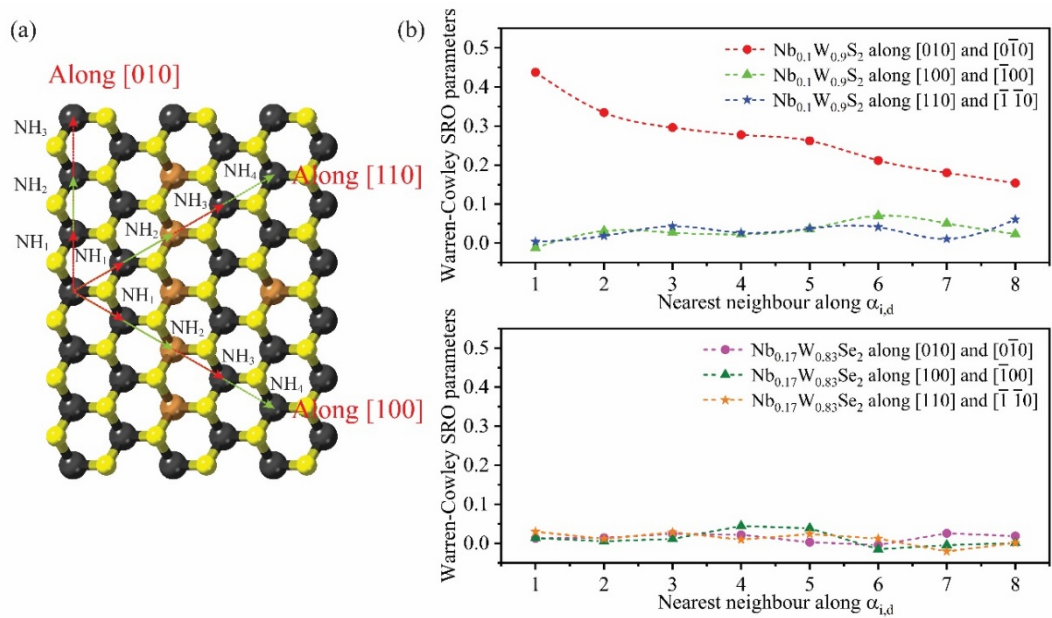
Figure 5.6. Statistical SRO analysis. (a) The Warren-Cowley SRO parameters can be further described via a vector pair correlation $\alpha = (\alpha_{i,1}, \alpha_{i,2}, \alpha_{i,3})$ based on hexagonal structure. Modelled $Nb_{0.1}W_{0.9}S_2$ structure with arrows schematically indicating 1st to 4th nearest neighbours around a metal atom along [100], [010] and [110]. (b) Comparison of the Warren-Cowley SRO parameters along $\alpha_{i,1}$, $\alpha_{i,2}$, and $\alpha_{i,3}$ calculated for the $Nb_{0.1}W_{0.9}S_2$ and $Nb_{0.17}W_{0.83}Se_2$ monolayers shown in Figure 5.3 and 5.4, respectively.

For monolayer $Nb_{0.17}W_{0.83}Se_2$, the SRO parameters from the 1st to 8th nearest neighbour along different directions are shown in Figure 5.6b. As can be observed, all the SRO parameters are close to 0, indicating that Nb atoms tend to distribute randomly in the $Nb_{0.17}W_{0.83}Se_2$ monolayer, in agreement with the conclusions drawn from visual inspection of the ADF-STEM imaging of this alloy in Figure 5.4a.

5.3.3 DFT calculations

To gain insight into the cause of the SRO in $Nb_{0.1}W_{0.9}S_2$, the group of Dr Nicholas Hine performed DFT calculations of this system. As described in section 4.4.3, the formation energy can be calculated as[135]

$$E_F = E_T - E_T^{pure} + \sum_i m\mu_i$$

where E_T is the total energy of a supercell, E_T^{pure} is the total energy of pure materials, μ_i is the chemical potential and m the number of substituted cations.
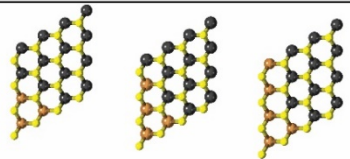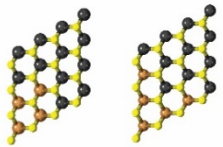
The binding energy, E_b, for an atomic configuration with m doped atoms can be calculated as follows[135]:

$$E_b = E_F(mNb) - mE_F(1Nb)$$

$$= E_T(mNb) - mE_T(1Nb) - (m-1)\,E_T^{pure}$$

where $E_T(mNb)$ is the total energy of a supercell with m substituted cations in a desired configuration. Therefore, the binding energy (E_b) is defined as the difference of the formation energies between isolated and segregated Nb atoms in supercells at the same concentration.
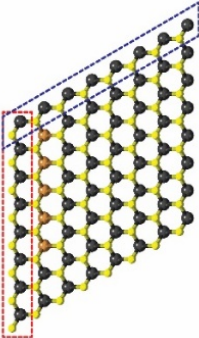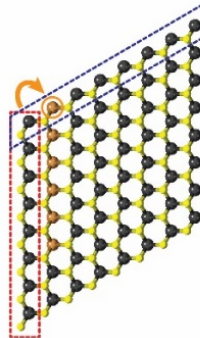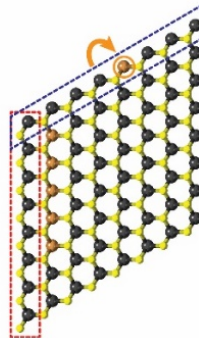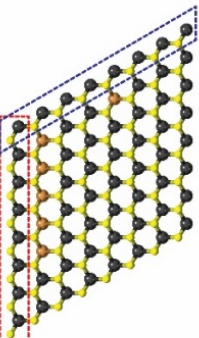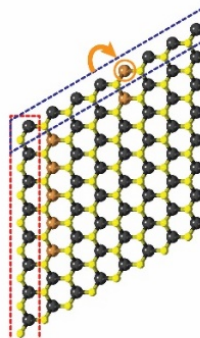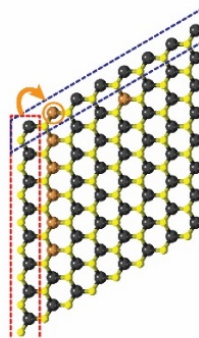
The binding energies for given atomic configurations, depending on the number of Nb-Nb bonds, are presented in Table 5.1. The binding energy for two adjacent Nb atoms in a supercell is found to be -125.80 meV, increasing with the number of Nb atoms in the supercell (binding energy more negative). This is a substantial binding energy, much

Table 5.1. Calculated binding energies of atomic configurations selected from the STEM image of $Nb_{0.1}W_{0.9}S_2$ monolayers.

Atomic configurations					
Binding energy (meV)	0	0	-125.79 meV	-253.79 meV	-420.78 meV
Number of Nb-Nb bonds	0	0	1	2	3

Atomic configurations			
Binding energy (meV)	-373.69 meV	-480.02 meV	-676.46 meV
Number of Nb-Nb bonds	3	4	5

Atomic configurations		
Binding energy (meV)	-474.86 meV	-594.95 meV
Number of Nb-Nb bonds	5	5

larger than that found for $Mo_{1-x}W_xS_2$ in the previous chapter, justifying why ordering is observed here. These results indicate that Nb atoms tend to form segregations, with larger segregations more energetic favourable than small ones. Moreover, at thermal equilibrium, segregations with L shapes are more energetically favourable than line, triangle or square shapes when there are 4 or 5 Nb atoms in a supercell (see corresponding binding energies in Table 5.1). This last fact is clearly different from the visual observations from the atomic-resolution imaging of $Nb_{0.1}W_{0.9}S_2$ monolayers where lines are observed rather than L segregations. This indicates that the atomic distribution in this alloy cannot be explained just by thermodynamics, kinetic effects must also play an important role during growth. One possible explanation is the much lower Nb than W concentration at the growing front. Since the growing front of a single flake moves forward row-by-row[60,157,158], the Nb atoms at the front are segregated to Nb atoms in the previous row, forming line configurations. Although clusters are energetically preferred, if the Nb concentration is too low, before a Nb atom can diffuse to minimise the energy, it is possible that the growing front has already moved forward, and the resultant line-

Table 5.2. Calculated binding energies of selected atomic configurations in an 8×8 supercell.

Atomic configurations			
Binding energy (meV)	-577.69 meV	-768.85 meV	-738.38 meV
Number of Nb-Nb bonds	4	5	4
Atomic configurations			
Binding energy (meV)	-717.53 meV	-938.34 meV	-924.22 meV
Number of Nb-Nb bonds	4	5	5

structure is frozen kinetically. This explains the prevalence of atomic line configurations of Nb atoms as observed in the CVT grown monolayers.

The binding energy continues to increase as the line of Nb atoms extends, indicating that ordering should persist beyond pairs of atoms into lines. The experimental observations of $Nb_{0.1}W_{0.9}S_2$ monolayers are thus consistent with a combination of kinetic and thermodynamic considerations. The spacing of several unit cells between lines of Nb atoms indicates that the Nb atoms must diffuse at least that length scale along the edge of the growing front. The continuous decrease of $\alpha_{i,1}$ with i, despite the binding energy increasing with increasing length of line, indicates that at these low Nb concentrations there is a significant probability that the growth front advances, ending the segment of Nb line, before a Nb atom diffuses along the growing front to join the end of the existing Nb line. This low concentration and short diffusion length also explain why Nb lines are formed rather than L shapes.

5.3.3 Multi-layer $Nb_{0.1}W_{0.9}S_2$

As discussed in the previous sections, in $Nb_{0.1}W_{0.9}S_2$ monolayers lines of Nb atoms are observed along one of the three equivalent crystallographic directions ([100], [010] and [110]), with a few unit cells of WS_2 between the lines. These monolayers are exfoliated from a bulk single crystal grown by CVT. So, an obvious question is whether the lines of Nb atoms are aligned across the layers of the bulk crystals.

To analyse this, ADF-STEM images were taken in areas of $Nb_{0.1}W_{0.9}S_2$ crystals containing both monolayers and bilayers. Figure 5.7a shows both monolayer and bilayer regions; there is a small section of bilayer on the right hand side of the image (brighter). Here it seems that Nb atoms form the same pattern in the monolayer and bilayer of the $Nb_{0.1}W_{0.9}S_2$ crystals. Figure 5.7b shows a bilayer $Nb_{0.1}W_{0.9}S_2$ with a hole, in which the bottom layer is exposed; in this section the Nb atoms are still ordered into lines and the atomic lines in each layer lie along the same crystallographic direction. Figure 5.7c reveals a large area of $Nb_{0.1}W_{0.9}S_2$ bilayer flake. Here, the Nb lines occur along different crystallographic directions, pointing at 60°/120° (as expected on its hexagonal structure) with respect to each other. From analysis of multiple regions, it seems there is no correlation (or anti-correlation) of the direction of ordering in one-layer relative to the next. This is consistent with the formation of the lines being related to the growth fronts.
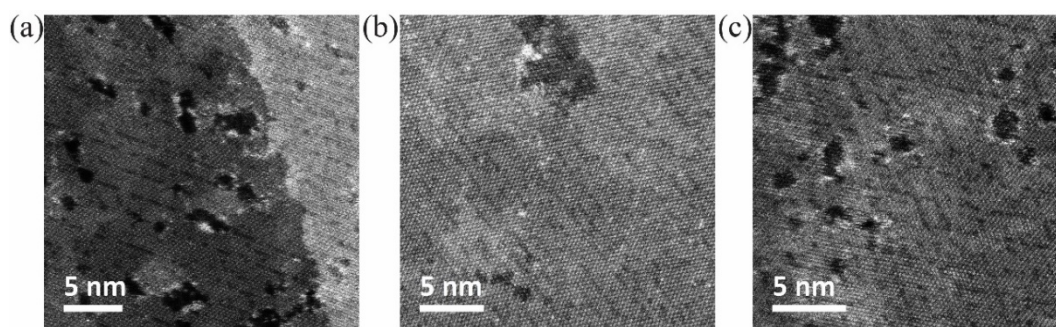
Figure 5.7. ADF-STEM images of bilayer $Nb_{0.1}W_{0.9}S_2$. (a) An ADF image of a $Nb_{0.1}W_{0.9}S_2$ flake with monolayer and bilayer regions at its edge shows the line segregations stack along the same crystallographic direction. (b) An ADF image of bilayer $Nb_{0.1}W_{0.9}S_2$ with the Nb atomic lines in each layer lying parallel to one another. (c) An ADF image of a bilayer $Nb_{0.1}W_{0.9}S_2$ flake with the Nb atomic lines in each layer lying along different crystallographic directions.

5.4 Optical properties of short-range ordered $Nb_{0.1}W_{0.9}S_2$ monolayers

As described in Chapter 2, ARPRS can be used to investigate anisotropy in a material's optical properties[24,159–161]. For example, ARPRS has been used to rapidly identify the crystal orientation of BP and $1T'$ $MoTe_2$[77,162,163]. Here, the ordered atomic lines of Nb, which span the whole monolayer flakes, break the six-fold rotational symmetry of the crystal lattice. This may lead to anisotropic Raman response along, or perpendicular to, the direction of the Nb lines which could be expected to support NbS_2-like phonon modes. Therefore, we applied ARPRS measurements to investigate whether an in-plane anisotropic Raman response could be used as a rapid and simple signature of this atomic-scale ordering.

5.4.1 In-plane polarisation Raman spectra

As introduced in Chapter 2, there are two common arrangements for ARPRS; the Horiba system used for this work relies on a half-wave plate, as shown in Figure 5.8a. The laser travels through polariser I and a half-wave plate to the sample, from which it is reflected to a spectrometer, after passing polariser II. The polarisation state is controlled by the half-wave plate. By rotating the fast axis of the half-wave plate by angle $\alpha/2$, the incident laser was linearly polarised and rotated α with respect to X axis of the laboratory coordinates. Figure 5.8b and 5.8c show two typical configurations used in the following measurements. The laboratory coordinates (X, Y, Z) are represented by red arrows, while the crystal coordinates (x', y', z') are in black short dash arrows. The orientation of the monolayer flake with respect to laboratory coordinates is unknown (defined as θ). In parallel configuration, polariser II is parallel to the x axis of laboratory coordinates, however it is aligned parallel to Y axis of laboratory coordinates in cross configuration.
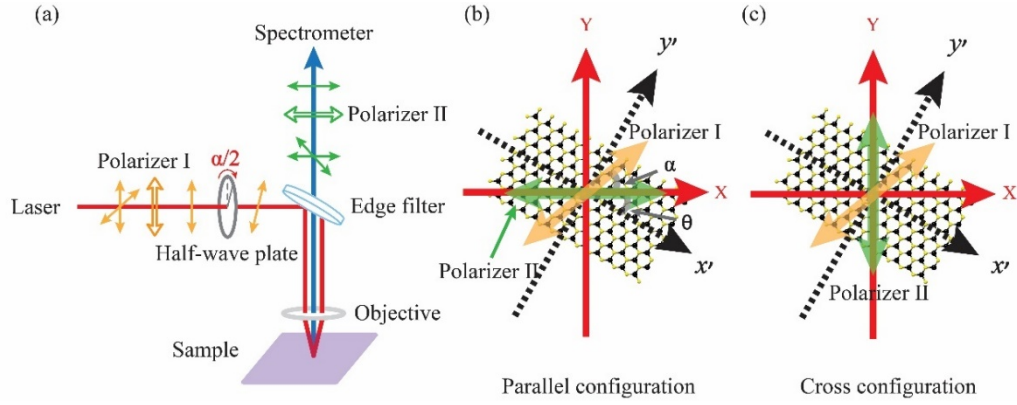
Figure 5.8. Schematic diagrams of ARPRS. (a) Polarized Raman spectra were observed via the schematic setup. The laser is linearly polarized after travelling through a half-wave plate and propagates along z axis. Two configurations (parallel and cross) are shown in (b) and (c), respectively. The red arrows represent the laboratory coordinate (X, Y, Z) and the black dash arrows correspond to the crystal coordinate (x', y', z'), respectively. θ is the angle between the laboratory and crystal coordinates. The orange and light green double arrows indicate the incident beam and the scattered beam detected by the spectrometer, respectively. α is the rotation angle of the incident beam controlled via a half-wave plate shown in Figure (a).

Raman tensors of the Raman active modes A_{1g}, E_{1g} and $2E_{2g}$ (E_{2g}^1 and E_{2g}^2) for monolayer MX_2 (M = Mo, W, Nb and Ta; while X = S and Se) are shown as below [24,159,164,165],

$$A_{1g}: \begin{pmatrix} a & 0 & 0 \\ 0 & a & 0 \\ 0 & 0 & b \end{pmatrix};$$

$$E_{2g}: \begin{pmatrix} 0 & d & 0 \\ d & 0 & 0 \\ 0 & 0 & 0 \end{pmatrix}, \begin{pmatrix} d & 0 & 0 \\ 0 & -d & 0 \\ 0 & 0 & 0 \end{pmatrix};$$

$$E_{1g}: \begin{pmatrix} 0 & 0 & 0 \\ 0 & 0 & c \\ 0 & c & 0 \end{pmatrix}, \begin{pmatrix} 0 & 0 & -c \\ 0 & 0 & 0 \\ -c & 0 & 0 \end{pmatrix}. \tag{5.3}$$

In the back-scattering Raman configuration (within XY plane), E_{1g} is absent due to its Raman tensor[79]. The E_{2g}^2 is expected around 33.5 cm^{-1}, out of the detection range of this experiment. Therefore, in this chapter we focus on analysis of the A_{1g} and E_{2g}^1 modes.

The Raman intensity of a phonon mode in classical formula has been introduced in Chapter 2[24],

$$I \propto |\boldsymbol{e}_i \cdot \widetilde{\boldsymbol{R}} \cdot \boldsymbol{e}_s|^2 \,,$$

where $\boldsymbol{e}_i$ and $\boldsymbol{e}_s$ are the incident and scattered beam, respectively, and $\widetilde{\boldsymbol{R}}$ is the Raman tensor. A phonon mode can only be detected when $I \neq 0$[24].

For the parallel configuration shown in Figure 5.8b, the Raman intensity for the A_{1g} mode can be calculated via

$$I_{A_{1g}} \propto \left| [\cos(\alpha + \theta),\ \sin(\alpha + \theta),\ 0] \begin{pmatrix} a & 0 & 0 \\ 0 & a & 0 \\ 0 & 0 & b \end{pmatrix} \begin{pmatrix} \cos\theta \\ \sin\theta \\ 0 \end{pmatrix} \right|^2.$$

To simplify, $I_{A_{1g}} \propto a^2 cos^2\alpha$. Therefore, the intensity of the A_{1g} mode depends on the angle of the half-wave plate.

Meanwhile the in-plane E_{2g}^1 mode is double-degenerate and there are two Raman tensors, R_x and R_y, vibrating along the a and b axis, respectively[165,166]. Therefore, the Raman intensity of E_{2g}^1 mode can be calculated via[165]:

$$I_{E_{2g}^1} = I_{E_{2g}^1-x} + I_{E_{2g}^1-y} = |\boldsymbol{e}_i \cdot \boldsymbol{R}_x \cdot \boldsymbol{e}_s|^2 + |\boldsymbol{e}_i \cdot \boldsymbol{R}_y \cdot \boldsymbol{e}_s|^2 \,. \qquad 5.4$$

For the two components:

$$I_{E_{2g}^1-x} \propto \left| [\cos(\alpha + \theta), \sin(\alpha + \theta),\ 0] \begin{pmatrix} 0 & d & 0 \\ d & 0 & 0 \\ 0 & 0 & 0 \end{pmatrix} \begin{pmatrix} \cos\theta \\ \sin\theta \\ 0 \end{pmatrix} \right|^2$$

$$= d^2 (\cos\alpha \sin 2\theta + \sin\alpha \cos 2\theta)^2,$$

$$I_{E_{2g}^1-y} \propto \left| [\cos(\alpha + \theta), \sin(\alpha + \theta),\ 0] \begin{pmatrix} d & 0 & 0 \\ 0 & -d & 0 \\ 0 & 0 & 0 \end{pmatrix} \begin{pmatrix} \cos\theta \\ \sin\theta \\ 0 \end{pmatrix} \right|^2$$

$$= d^2 (\cos\alpha \cos 2\theta - \sin\alpha \sin 2\theta)^2.$$

For the E_{2g}^1 mode,

$$I_{E_{2g}^1} = I_{E_{2g}^1 - x} + I_{E_{2g}^1 - y}$$

$$\propto d^2[(\cos\alpha \sin 2\theta + \sin\alpha \cos 2\theta)^2 + (\cos\alpha \cos 2\theta - \sin\alpha \sin 2\theta)^2] = d^2.$$

Therefore, for the parallel configuration, the E_{2g}^1 mode is a constant as a function of the angle of the incident light. It should be polarisation independent.

For the cross configuration, the scattered light detected by the spectrometer is $\boldsymbol{e}_s = \begin{pmatrix} -\sin\theta \\ \cos\theta \\ 0 \end{pmatrix}$, therefore the intensity of the two Raman modes can be calculated via similar operations giving $I_{A_{1g}} \propto a^2 \sin^2\alpha$ and $I_{E_{2g}^1} = I_{E_{2g}^1 - x} + I_{E_{2g}^1 - y} \propto d^2$. Thus, the intensity of A_{1g} mode is proportional to $a^2 \sin^2\alpha$ in the cross configuration, while the E_{2g}^1 mode is independent of α.

5.4.1.1 Polarised Raman spectra

For pure materials, an optical image of exfoliated WS_2 flakes on a SiO_2 substrate is shown in Figure 5.9a. The Raman spectra are shown in Figure 5.9c for $Z(XX)\bar{Z}$ and $Z(XY)\bar{Z}$ polarisation configurations. The directions of the laboratory coordinate and incident laser (polariser I) are indicated via solid arrows. The Raman peaks located at 351.5, 356.0 and 415.3 cm⁻¹ corresponding to 2LA (**M**), E_{2g}^1 (**Γ**) and A_{1g} (**Γ**) optical modes, respectively, are consistent with the literature values for excitation with the same laser wavelength (488 nm)[167]. For pure NbS_2 monolayers on a SiO_2 substrate, the reported Raman active modes E_{2g}^1 (**Γ**) and A_{1g} (**Γ**) are at 303.0 and 379.0 cm⁻¹, respectively[168,169].

The Raman spectra of $Nb_{0.1}W_{0.9}S_2$ monolayers for $Z(XX)\bar{Z}$ and $Z(XY)\bar{Z}$ polarisation configurations are shown in Figure 5.9d and compared to the pure materials. The Raman peaks of the WS_2-like E_{2g}^1 (**Γ**) and A_{1g} (**Γ**) optical modes are at 357.7 and 416.2 cm⁻¹, while the NbS_2-like E_{2g}^1 (**Γ**) and A_{1g} (**Γ**) modes are around 310 and 389 cm⁻¹, respectively. Compared to the pure materials, the modes shift to higher wavenumber, consistent with the expected p-type doping. While the second order Raman mode 2LA(**M**) that is the longitudinal acoustic mode around the **M** point of the BZ shifts to
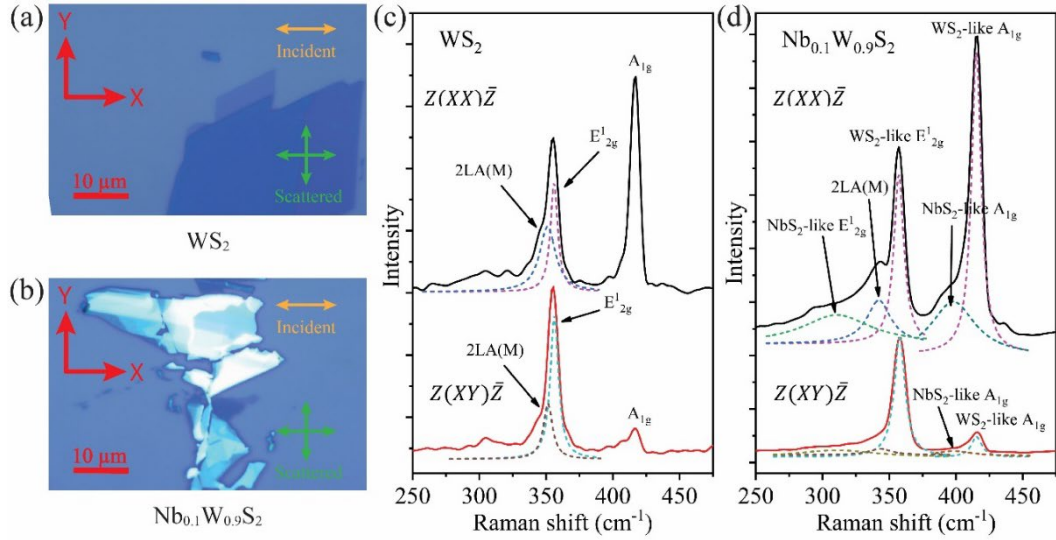
Figure 5.9. Polarized Raman spectra of a WS$_2$ and a Nb$_{0.1}$W$_{0.9}$S$_2$ monolayer. (a) Optical image of the WS$_2$ flake, the directions of the incident and scattered laser have been shown in orange and green, respectively. The laboratory coordinates are shown in red arrows. (b) Optical image of Nb$_{0.1}$W$_{0.9}$S$_2$ flake. Comparison of (c) WS$_2$ and (d) Nb$_{0.1}$W$_{0.9}$S$_2$ spectra in the range of 250 to 475 cm^{-1} for $Z(XX)\bar{Z}$ and $Z(XY)\bar{Z}$ polarisation configurations.

lower wavenumber, that can be attributed to the change of electronic structure caused by the alloying.

5.4.1.2 Angle-resolved polarised Raman spectroscopy (ARPRS) of WS$_2$ monolayers

The Raman intensity of A$_{1g}$ modes is expected to be proportional to $a^2 cos^2\alpha$ and $a^2 sin^2\alpha$ in parallel and cross configurations, respectively, where α is the angle controlled by the half-wave plate, independent of the sample. By contrast, the Raman intensity of the E$_{2g}^1$ mode is expected to be constant ($I_{E_{2g}^1} \propto d^2$), independent of the angles of polarisation.

Figure 5.10 shows the Raman spectra as a function of the polarisation angle, along with the corresponding polar plots for E$_{2g}^1$ and A$_{1g}$ modes of pure WS$_2$ monolayer in the parallel configuration. The normalised polar plot of the A$_{1g}$ mode at the top of Figure 5.10b shows the Raman intensity as a function of the polarisation angle: it has a maximum value at 0° and minimum at 90°, consistent with the predictions derived before
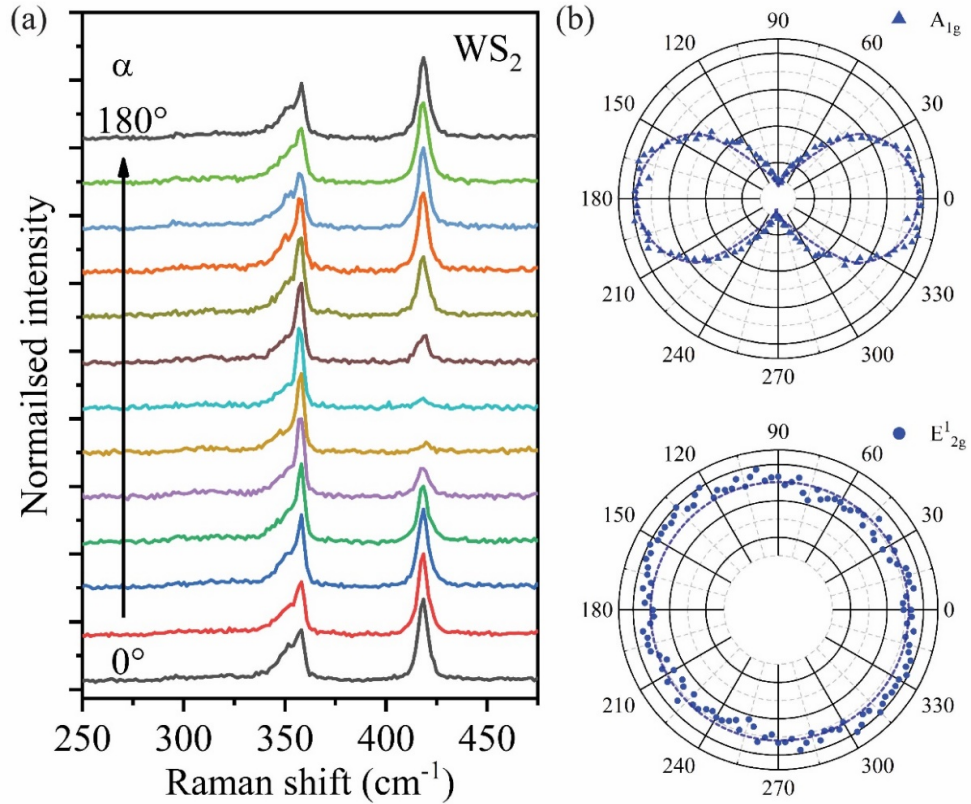
Figure 5.10. Polarization dependence of the intensity of the Raman modes in the parallel configuration. (a) Polarization dependent Raman spectra of WS_2 monolayer as a function of polarization angle α. (b) Normalised polar plots of the Raman modes in (a), for the A_{1g} mode at the top and E_{2g}^1 mode at the bottom.

$(I_{A_{1g}} \propto a^2 cos^2\alpha)$. The polar plot for the Raman active E_{2g}^1 mode for pure WS_2 is shown at the bottom of Figure 5.10b. It is close to a circle, constant independent of the angle of polarisation, in agreement with the predictions $(I_{E_{2g}^1} \propto d^2)$.

5.4.1.3 Polarization dependent measurements of $Nb_{0.1}W_{0.9}S_2$ monolayer

There are two clear features around 355 and 415 cm^{-1} in the Raman spectra of monolayer $Nb_{0.1}W_{0.9}S_2$ in the range of 175 - 475 cm^{-1} for both parallel and cross configurations, as shown in Figure 5.11a and 5.11b respectively. As discussed in section 5.4.1.1, the peaks around 310 and 358 cm^{-1} correspond to the NbS_2-like E_{2g}^1 and WS_2-like E_{2g}^1 modes, respectively, while the peak around 415 cm^{-1} originates from the WS_2-like A_{1g} mode. The integrated intensity of each peak has been plotted as a function of the polarisation angle (the angle of the half-wave plate a) in Figure 5.11c – 5.11h.
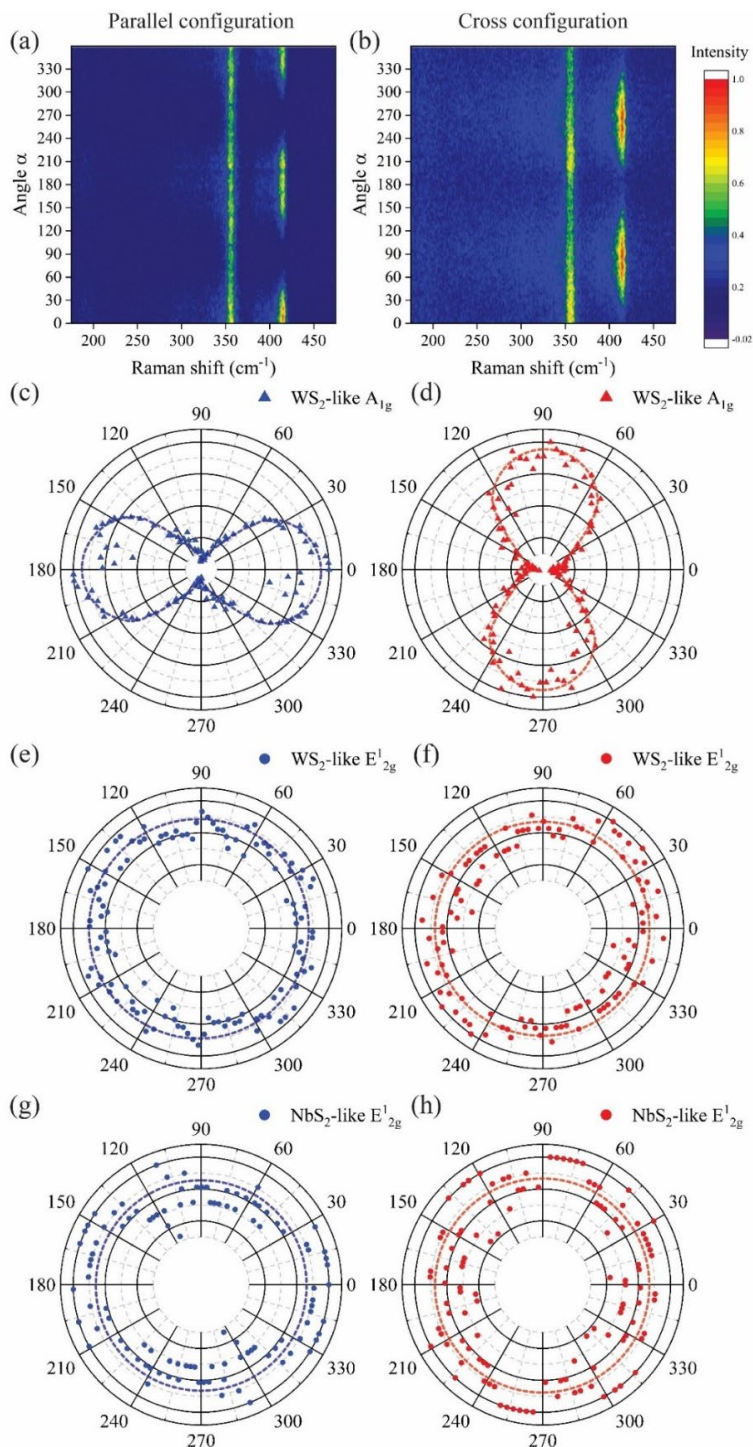
Figure 5.11. Polarization-dependent Raman spectra of a monolayer $Nb_{0.1}W_{0.9}S_2$ in parallel and cross configuration. The sample is shown in Figure 5.9b. Polarization-dependent Raman spectra in range of 175 to 475 cm^{-1}, in (a) parallel and (b) cross configuration, respectively. Normalised polar plots of WS_2-like A_{1g} mode in (c) parallel and (d) cross configuration. Normalised polar plots of WS_2-like E^1_{2g} mode in (e) parallel and (f) cross configuration. Normalised polar plots of NbS_2-like E^1_{2g} mode in (g) parallel and (h) cross configuration.

For the WS_2-like A_{1g} mode, the polar plots for parallel and cross configurations are shown in Figure 5.11c and 5.11d, respectively. The intensity of A_{1g} mode for parallel configuration in figure 5.11c has its maximum value at 0° and minimum value at 90°, consistent with the prediction in section 5.4.1 that $I_{A_{1g}} \propto a^2 cos^2\alpha$. For cross configuration, the minimum intensity is at 0° with the maximum at 90°, again as predicted in section 5.4.1.1 ($I_{A_{1g}} \propto a^2 sin^2\alpha$).

For the WS_2-like E_{2g}^1 mode in parallel and cross configuration, Figure 5.11e and 5.11f shows constant intensity that is independent of the polarisation angle of the incident laser, again in agreement with the predictions $I_{E_{2g}^1} \propto d^2$ in section 5.4.1. While for the NbS_2-like E_{2g}^1 mode, the Raman intensity of Figure 5.11g and 5.11h are constant in parallel and cross configurations as well.

The Raman tensors used to predict the Raman intensities only depend on the symmetry of the vibrational mode and the point groups, independent of the specific materials[24,159]. For example, hexagonal $1H$-$MoTe_2$ shows Raman intensity independent of the polarisation angle while the monoclinic $1T'$-$MoTe_2$ shows anisotropic properties[163]. Although the Nb atomic lines are lying along one direction over the whole monolayer single crystal, they are not periodic or continuous and the overall symmetry is retained on optical length scales (the crystallographic point group). Hence, the polar plots of the Raman active modes for $Nb_{0.1}W_{0.9}S_2$ monolayer are similar to those of the pure materials. This demonstrates that ARPRS is not a sensitive probe for ordering in MX_2 alloys and atomic resolution imaging is required.

5.4.2 PL measurements on $Nb_{0.1}W_{0.9}S_2$ monolayers

Both elemental analysis and atomic resolution imaging show significant concentrations of Nb (around 10%) which should act as a p-type dopant in WS_2, since Nb has one less valence electron than W. At this concentration, the flakes should be degenerately doped or metallic, with the chemical potential deep in the VB. This makes it intriguing to look for a PL response in monolayers of this material. Figure 5.12a shows PL spectra of $Nb_{0.1}W_{0.9}S_2$ and WS_2 monolayers. The PL peak of pure WS_2 monolayer is at 1.97 eV and can be attributed to A exciton emission[106,107,170]. The PL peak of Nb-containing WS_2 becomes broader and is red-shifted, however, the main peak around 1.76
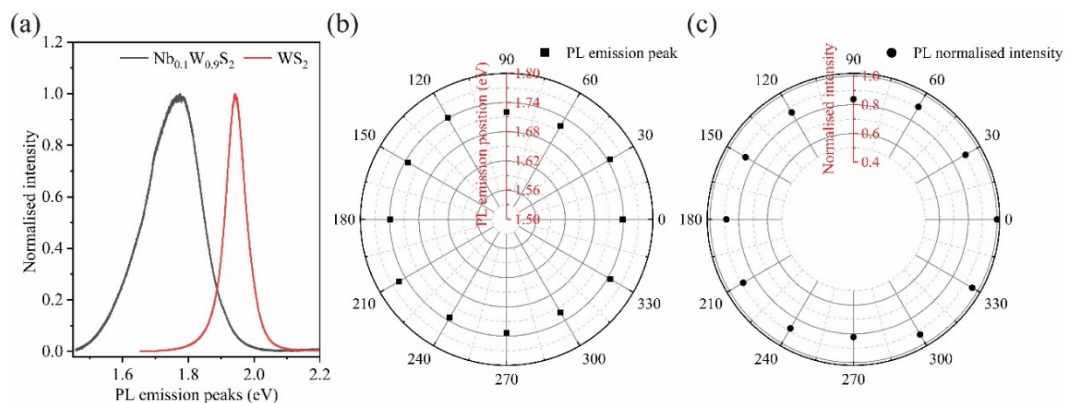
Figure 5.12. PL measurements on a $Nb_{0.1}W_{0.9}S_2$ and a WS_2 single layer. (a) PL spectra of the exfoliated $Nb_{0.1}W_{0.9}S_2$ and WS_2 flakes shown in Figure 5.9a and 5.9b, respectively. (b) PL emission peak positions of $Nb_{0.1}W_{0.9}S_2$ monolayers as a function of polarisation angle of the incident laser beam. (c) Normalised intensity of $Nb_{0.1}W_{0.9}S_2$ PL peaks as the half-wave plate is rotated from 0 to 90°.

eV can still be assigned to A exciton emission. In addition to the A exciton emission peak, there are new peaks at 1.65-1.75 eV that can be deconvoluted from the $Nb_{0.1}W_{0.9}S_2$ spectrum. These peaks may be assigned to emissions from the localised excitons that have been trapped in the potential caused by the impurity atoms.

Similarly, to investigate the effect of the atomic lines on the properties of $Nb_{0.1}W_{0.9}S_2$, we performed polarised PL measurements in the Horiba system. As seen in Figure 5.12b, both the intensity and energy of the PL emission are independent of the polarisation angle of the incident laser beam.

5.5 Optical and electronic measurements on random $Nb_{0.17}W_{0.83}Se_2$ alloys

5.5.1 Optical measurements

Figure 5.13a shows the Raman spectrum of $Nb_{0.17}W_{0.83}Se_2$ monolayer under 488 nm laser excitation. For a pure WSe_2 monolayer, the A_{1g} and E^1_{2g} modes are located at 251 cm^{-1} and 248 cm^{-1}, respectively[67], while for pure $NbSe_2$, the A_{1g} and E^1_{2g} modes are at 228.7 cm^{-1} and 237.5 cm^{-1}, respectively under an excitation of 532 nm[164]. The peak around 245 cm^{-1} can be assigned to the WSe_2-like A_{1g} and E^1_{2g} modes, while the shoulder
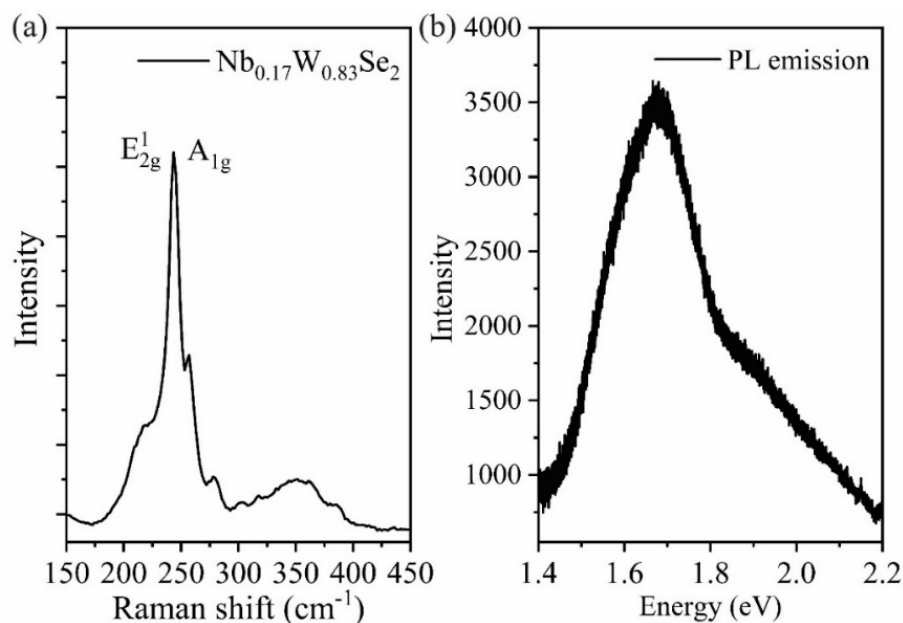
Figure 5.13. Optical measurements on an exfoliated $Nb_{0.17}W_{0.83}Se_2$ monolayer. (a) Raman spectrum with a range of 150 - 450 cm^{-1}. (b) PL spectrum of the $Nb_{0.17}W_{0.83}Se_2$ monolayer.

around 225 cm^{-1} can be attributed to the A_{1g} mode of $NbSe_2$, this is consistent with the literature[171]. The PL spectrum of the $Nb_{0.17}W_{0.83}Se_2$ monolayer is shown in Figure 5.13b, it is slightly blue-shifted to 1.68 eV, compared to 1.65 eV for pure monolayer WSe_2 monolayer under 488 nm excitation[172]. Furthermore, because the $Nb_{0.17}W_{0.83}Se_2$ monolayer shows random distributions, and it shows the similar atomic structure as pure WSe_2, there is no further polarisation measurements taken.

5.5.2 ARPES measurements

ARPES measurements were performed at the Spectromicroscopy beamline of the Elettra synchrotron in Trieste. Data analysis and DFT calculations were performed by Dr. Nick Hine. A flake of $Nb_{0.17}W_{0.83}Se_2$ was exfoliated, transferred to hBN, and measured. Energy-momentum slices along the $\boldsymbol{\Gamma}$ to $\mathbf{K}$ direction for monolayer, bilayer and bulk regions of $Nb_{0.17}W_{0.83}Se_2$ are shown in Figure 5.14. The bands near the $\mathbf{K}$ valley are similar from monolayer to bulk, because of their in-plane orbital character[35]. However, there are strong hybridization effects on the bands near $\boldsymbol{\Gamma}$ because of the out-of-plane orbital character. The VB splits at $\boldsymbol{\Gamma}$ for the bilayer and bulk alloy, as expected for pure WSe_2[35], with the band edge moving to lower binding energy. As a result, the VBM changes from $\boldsymbol{\Gamma}$ to $\mathbf{K}$ as it is reduced from bulk to monolayer and the bandgap
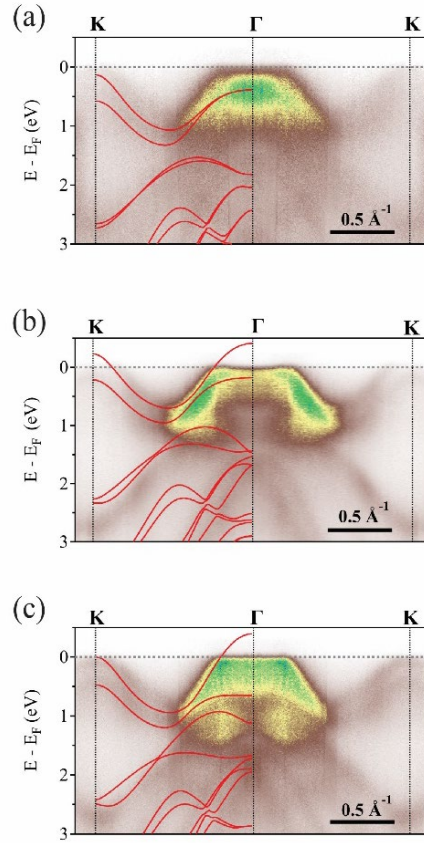
Figure 5.14. ARPES measurements for $Nb_{0.17}W_{0.83}Se_2$ flake with different thickness. Energy-momentum slices along the $\mathbf{\Gamma}$ to $\mathbf{K}$ direction of (a) monolayer $Nb_{0.17}W_{0.83}Se_2$, (b) bilayer $Nb_{0.17}W_{0.83}Se_2$ and (c) bulk $Nb_{0.17}W_{0.83}Se_2$ with DFT predictions overlaid on each, aligned with the lower VB at $\mathbf{K}$.

evolves from indirect to direct. However, unlike pure WSe_2 where the chemical potential is near the centre of the band gap, the chemical potential is clearly in the VB indicating strong p-type doping.

The spectra for bilayer $Nb_{0.17}W_{0.83}Se_2$ and bilayer WSe_2 are compared in Figure 5.15, with DFT predictions for bilayer WSe_2 overlaid. Compared with pure bilayer WSe_2, the bands upshift, with the band edges higher than the Fermi level at both $\mathbf{K}$ and $\mathbf{\Gamma}$. The energy of the band edges is found by comparison of the ARPES to the DFT spectra, giving $E_{\mathbf{\Gamma}} = 0.41$ eV and $E_{\mathbf{K1}} = 0.23$ eV. From this, the carrier concentration can be estimated using[173]:
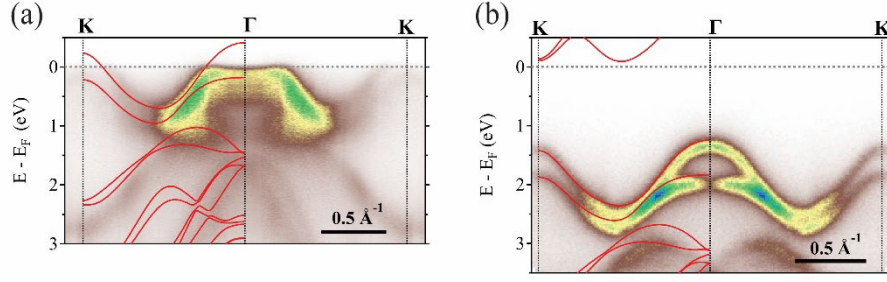
Figure 5.15. Comparison of ARPES measurements on the $Nb_{0.17}W_{0.83}Se_2$ alloy and pure material. Energy-momentum slices along the Γ to K direction of (a) bilayer $Nb_{0.17}W_{0.83}Se_2$ and (b) bilayer WSe_2 [32] with DFT predictions overlaid on each, aligned with the lower VB at K.

$$p = \int_{-\infty}^{E_{K1}} g_{V_{K1}}(1 - f(E)) \, dE + \int_{-\infty}^{E_{\Gamma}} g_{V_{\Gamma}}(1 - f(E)) \, dE, \qquad 5.5$$

where $g(E)$ is the density of energy states, $g_{V_{K1}} = \frac{(2)(2)m^*_{K1}}{\pi \hbar^2}$ and $g_{V_{\Gamma}} = \frac{(2)(1)m^*_{\Gamma}}{\pi \hbar^2}$, and $f(E) = exp\left(\frac{E_F - E}{k_B T}\right)$ is the statistical distribution function describing the occupation of these states[173]. The effective mass can be obtained from DFT predictions $m^*_{\Gamma} = 0.96$ m_o[174], while $m^*_{K1} = 0.42 \, m_o$[175]. Using these predictions, we demonstrated a value for $p = 4.9 \times 10^{14}$ cm^{-2}. This corresponds to 0.42 holes per unit cell for a bilayer, consistent (within expected levels of uncertainty for this estimation) with the composition of $Nb_{0.17}W_{0.83}Se_2$ determined by atomic-resolution imaging.

It is thus clear that the $Nb_{0.17}W_{0.83}Se_2$ flakes are heavily doped to the extent that they should be metallic in nature. For the PL measurements of the $Nb_{0.1}W_{0.9}S_2$ and $Nb_{0.17}W_{0.83}Se_2$ monolayer, the optical emission peaks corresponding to A excitons are similar to those of the corresponding pure materials. It is difficult to reconcile this optical response with the significant change to the electronic structure. Since the Nb atoms form atomic segregations (Å) within the W matrix, this could be attributed to localised excitons on similar length scales behaving differently to the area-averaged band structure. Therefore, it is interesting to study whether there are local changes in the electronic structure due to the Nb ordering. LL-STEM-EELS is a promising technique for achieving this due to its subwavelength resolution and ability to probe the local density of the optical states for thin materials[91,92,176].

5.6 STEM plasmon spectroscopy

LL-STEM-EELS analysis was carried out on a monolayer $Nb_{0.1}W_{0.9}S_2$ flake encapsulated in graphene for stability. An integrated spectrum of the region is presented in Figure 5.16 where the ZLP has been deconvoluted and subtracted. Here, the $\pi + \sigma$ bulk plasmon around 22 eV is observed. Note that the intensity in the $\pi + \sigma$ bulk plasmon is very large due to the hydrocarbon contribution present in the specimen. Shoulder 16 eV can be also observed in the figure, which are consistent with the surface plasmon energy (E_s):

$$E_s = \frac{E_p}{\sqrt{2}},$$

5. 6

with E_p is the bulk plasmon energy.

The ADF-STEM image (Figure 5.17a) shows the region of interest (ROI) where the data was acquired. The spectra in Figure 5.17b, from 2 eV to 18 eV, correspond to the area enclosed in the red and blue boxes, i.e. pure WS_2 and Nb-containing areas, respectively. In the spectra at room temperature two features (marked i and ii) can be distinguished at 3.0 eV and 8.5 eV, respectively.

Previous works (LL-STEM-EELS) on MoS_2 flakes assigned the peak around 3.0 - 3.5 eV to the C-exciton[177] that is inconsistent with its optical measurements (absorption and reflectance spectra)[178,179]. While there are no features around 3.0 eV in the reported LL-EELS of graphite, independent of the number of layers[180,181]. Therefore, we assign the
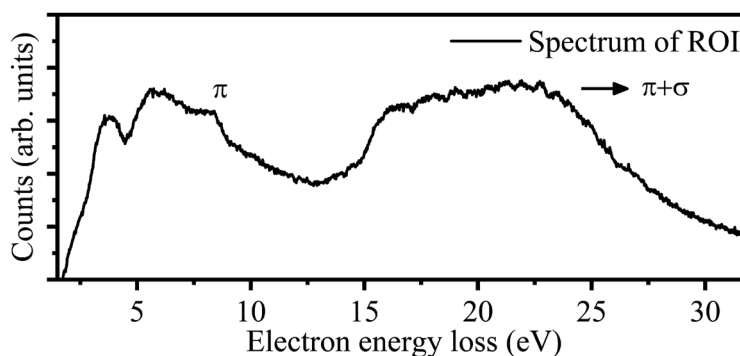
Figure 5.16. Low loss STEM-EELS of the region of interest (ROI) on a monolayer $Nb_{0.1}W_{0.9}S_2$ encapsulated with graphene.
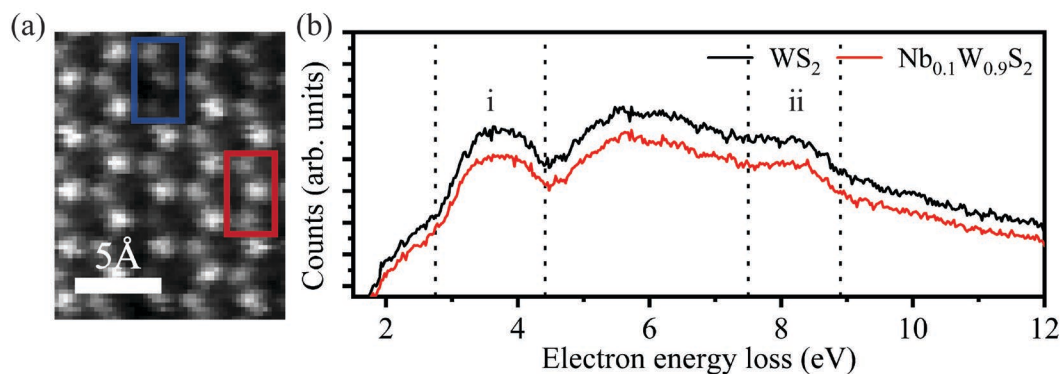
Figure 5.17. Low loss STEM-EELS of monolayer $Nb_{0.1}W_{0.9}S_2$. (a) ADF-STEM image of a monolayer $Nb_{0.1}W_{0.9}S_2$ sandwiched by a top and bottom layer graphene. (b) Low loss EELS spectra integrated from a $Nb_{0.1}W_{0.9}S_2$ and WS_2 region as indicated in a blue and red box, respectively, on the same flake. Small features are found around 3.5 eV and 8.2 eV.

peak at around 3.0 eV to excitons of the 2D alloys. When the MoS_2 or WS_2 flake is stacked with graphene, there are two possibilities, renormalisation of band structure occurs or not[178,182]. In the case of renormalisation, there will be shifts for the energy of C-excitons, but this shift is small in range of 0.1 eV[182]. Hence although the sample is graphene encapsulated, it is still reasonable to assign the peak at this range to excitons.

Furthermore, peak ii around 8.5 eV can be assigned to π-bulk plasmon of the $Nb_{0.1}W_{0.9}S_2$ flakes. In MoS_2 the π-bulk plasmon can be observed at 8.3 eV[177]. Shoulder/intensity at 6 eV correspond to the π surface plasmon energy. However, the broad background peak from 2.0 to 12.0 eV is attributed to graphene [180,181].

No clear differences are observed between the pure WS_2 and Nb-containing layer. The features distinguished in the EELS spectra appear to be uniform in intensity and position across the alloy, despite the atomic ordering, offering no clarification for the apparently contradictory findings from PL and ARPES measurements. It would be interesting to extend the low loss EELS to lower energy, to investigate whether the low energy excitations vary at the nanometre scale along with the atomic ordering.

5.7 Conclusions

In summary, we have found a short-range ordered TMD alloy using ADF-STEM imaging to directly reveal the inhomogeneous distribution of Nb atoms. The visual

observations from the images have been validated by quantitative statistical analysis using the Warren-Cowley SRO parameters. DFT calculations applied to the common atomic configurations selected from the real images shows that segregation of the Nb atoms would be expected. The observation of lines of Nb atoms thus indicates that both thermodynamics and kinetics are important to create this ordering during growth. ARPRS was used to investigate anisotropic optical properties, but no influence of the ordered oriented atomic lines was found. Since the ordering is short range, rather than periodic uniform lines, it shows few polarisation features. ARPES measurements directly demonstrate that the chemical potential is deep in the VB, such that the alloy flakes should be metallic, however, PL emission is observed from their monolayers with peak emission positions similar to those of the pure material. The local electronic structure of the monolayer $Nb_{0.1}W_{0.9}S_2$ was probed by LL-STEM-EELS with atomic-resolution, to try to reconcile the optical activity (due to excitons localised at the nanoscale) to the measured band structure (averaged at the micrometre scale). Although evidence for exciton peaks were found in the low loss spectra, these were found to be homogeneous over the length scales of the ordering. Further investigations would be required to resolve this behaviour.

Chapter 6: Conclusions and Future Works

6.1 Conclusions of this thesis

This thesis makes contributions to our understanding of 2D semiconductor alloys, focussing on determining the atomic structure and correlating this to the resultant electronic structure. The synthesis by CVT of single crystals of pure TMDs and TMD alloys (including $Mo_{1-x}W_xS_2$, $Nb_{0.1}W_{0.9}S_2$, $Nb_{0.17}W_{0.83}Se_2$, WSeS and WSe_2) has been presented, and various fabrication techniques developed to exfoliate monolayer flakes from these crystals and build them into van der Waals solids with artificial sequences. Detailed studies on two kinds of alloys are discussed: $Mo_{1-x}W_xS_2$ was found to have random transition metal distributions, whilst short-range ordering was observed in $Nb_{0.1}W_{0.9}S_2$. The evolution of the electronic structure of $Mo_{1-x}W_xS_2$ has been investigated in detail through comparison between ARPES measurements and first principles calculations. Meanwhile, the effect of the ordered atomic lines in $Nb_{0.1}W_{0.9}S_2$ on the lattice vibrations and electronic structure has been studied.

For synthesis of TMD alloys, previous reports have shown that CVT results in more homogeneous synthesis than CVD. The growth conditions *e.g.* source temperature, growth temperature, the growth time and transport agents, *etc.* can have a significant influence on the synthesis process and the resultant material. For CVT, appropriate parameters have been found for the growth of $Mo_{1-x}W_xS_2$ and $Nb_{0.1}W_{0.9}S_2$ alloys, successfully growing single crystals up to a few centimetres across.

Fabrication techniques for the assembly of van der Waals stacks have been developed, including a dry transfer system, and optimised for the sample designs required for this thesis. PDMS and PMMA based transfers have proved effective for the fabrication of different types of samples. Moreover, a novel transfer method was developed to prepare graphene encapsulated TMD flakes for HRTEM analysis.

The atomic structure of $Mo_{1-x}W_xS_2$ alloys has been visualised by atomic resolution STEM images. Their elemental distributions have been quantitatively analysed by comparison with Monte Carlo simulations parameterised by first principles calculations. Statistical analysis of the distribution of W atoms is consistent with an essentially random distribution, as expected due to the small energy associated with placing W atoms next to one another and the high growth temperature.

Electronic structure measurements and calculations were applied to the $Mo_{1-x}W_xS_2$ alloys. Band parameters were extracted and compared for both the theoretical and experimental results. It is clear that alloying can be used for band structure engineering, continuously tuning the band structure parameters, such as the band gap, effective mass, SOC and even the order of the bands, across the alloy compositions. It is found that the VB SOC changes linearly with composition without bowing, resolving a conflict in the literature between prior optical spectroscopy measurements of $Mo_{1-x}W_xSe_2$ alloys which showed bowing in the energy difference between A and B excitons compared to first principles calculations which predicted a linear dependence of VB SOC on composition. Moreover, even though for intermediate compositions the CB SOC is less than the disorder potential due to alloying, spin-valley locking is still retained as shown by optical spectroscopy. These results demonstrate that alloying TMDs is an effective approach for spin-orbit engineering of 2D semiconductors and hence realising their potential for valleytronic and spintronic applications.

In contrast to the $Mo_{1-x}W_xS_2$ alloys, short-range ordering has been observed in ADF-STEM images of the TMD alloy $Nb_{0.1}W_{0.9}S_2$. This is apparent from visual inspection of the images and has also been confirmed by quantitative statistical analysis through determination of the Warren-Cowley SRO parameters. DFT calculations, on selected atomic configurations from the real ADF-STEM images, have shown that it is energetically favourable for Nb atoms to segregate. This on its own does not explain the observation of lines, rather than clusters. The atomic lines are observed to align across a monolayer, but in subsequent layers the orientation of the lines can change. This indicates that the directional ordering is not due to symmetry breaking by a macroscopic variable, such as gas flow or temperature gradient. Rather it is likely that the atomic lines of Nb atoms are due to a combination of thermodynamics and kinetic considerations, with the lines indicating the direction of the growth front.

ARPRS was used to study the influence of the ordered oriented atomic lines on their optical properties. Since the ordering is short-range, rather than periodic uniform lines, the Raman spectra show few anisotropic features. This demonstrates the importance of the atomic-resolution structure analysis: microscopic probes, such as Raman spectroscopy, are not always sensitive to this scale of atomic ordering. For comparison. ARPES measurements were taken on Nb-containing WSe_2 alloys. The chemical potential was found to be deep in the VB, such that the alloy flakes should be degenerately p-type doped and exhibit metallic behaviour. However, PL emission was observed from their monolayers, albeit with emission peaks shifted relative to the pure materials. To resolve the conflict between the electronic structure and the optical behaviour, which could have been due to localised semiconducting regions, LL-STEM-EELS with atomic-resolution was applied to explore the local electronic structure of monolayer $Nb_{0.1}W_{0.9}S_2$. However, the flake showed homogeneous properties over the micrometre scale of the ordering. Therefore, further investigations are required to resolve the conflict between the atomic, electronic and optical properties of these Nb doped alloys.

6.2 Future work

Although the LL-STEM-EELS has been applied to monolayer $Nb_{0.1}W_{0.9}S_2$ to probe the local electronic structure and the spectra show homogeneous properties over the micrometre scale, the experiments can still be improved. Firstly, the width of the intense ZLP in the EELS spectrum could be further reduced to a few hundreds of meV by using an aberration-corrected STEM with a monochromator. This would make it possible to resolve exciton features, such as the A and B excitons[91,92]. Secondly, isolated TMD samples without encapsulations are better for probing the local electronic structures, therefore the sample design could be improved.

Monolayer WS_2 is semiconducting while monolayer NbS_2 is metallic. Therefore, it is reasonable to assume that in ordered alloys of $Nb_{0.1}W_{0.9}S_2$, highly anisotropic electron transport should be expected, oriented to the Nb atomic lines. Although there have been many reports on the electron transport properties of TMDs, anisotropic transport is rare[183]. Hence, a further extension of this thesis would be electron transport measurements along each equivalent crystallographic direction of the hexagonal lattice. Continuing in this direction, at low temperatures monolayer NbS_2 is superconducting

[184,185]: hence it would be interesting to study the (possibly anisotropic) low-temperature magneto-transport properties of the $Nb_{1-x}W_xS_2$ alloys.

References

1. Moore, G. E. No exponential is forever: But 'forever' can be delayed! *Dig. Tech. Pap. - IEEE Int. Solid-State Circuits Conf.* 19–25 (2003).

2. Chau, R., Doyle, B., Datta, S., Kavalieros, J. & Zhang, K. Integrated nanoelectronics for the future. *Nat. Mater.* **6**, 810–812 (2007).

3. Novoselov, K. S., Fal'Ko, V. I., Colombo, L., Gellert, P. R., Schwab, M. G. & Kim, K. A roadmap for graphene. *Nature* **490**, 192–200 (2012).

4. Schwierz, F. Graphene transistors. *Nat. Nanotechnol.* **5**, 487–496 (2010).

5. Geim, A. K. & Grigorieva, I. V. Van der Waals heterostructures. *Nature* **499**, 419–425 (2013).

6. Novoselov, K. S., Mishchenko, A., Carvalho, A. & Castro Neto, A. H. 2D materials and van der Waals heterostructures. *Science (80-.).* **353**, (2016).

7. K. S. Novoselov, A. K. Geim, S. V. Morozov, D. Jiang, Y. Zhang, S. V. Dubonos, I. V. G. and A. A. F. Electric Field Effect in Atomically Thin Carbon Films. *Science (80-.).* **306**, 666–669 (2016).

8. Geim, A. & Novoselov, K. The Nobel Prize in Physics 2010. *NobelPrize.org.* (2010). Available at: https://www.nobelprize.org/prizes/physics/2010/summary/.

9. The graphene times. *Nat. Nanotechnol.* **14**, 903 (2019).

10. Geim, A. K. Nobel Lecture: Random walk to graphene. *Rev. Mod. Phys.* **83**, 851–862 (2011).

11. Kolobov, A. V & Tominaga, J. *Two-Dimensional Dichalcogenides*. (Springer International Publishing AG Switzerland, 2016).

References

12.   Liu, Y., Weiss, N. O., Duan, X., Cheng, H. C., Huang, Y. & Duan, X. Van der Waals heterostructures and devices. *Nat. Rev. Mater.* **1**, (2016).

13.   Georgiou, T., Jalil, R., Belle, B. D., Britnell, L., Gorbachev, R. V., Morozov, S. V., *et al.* Vertical field-effect transistor based on graphene-WS$_2$ heterostructures for flexible and transparent electronics. *Nat. Nanotechnol.* **8**, 100–103 (2013).

14.   Concerning, D., New, T., Crew, H., Salvio, A. De, Jackman, T. R., Larson, A., *et al.* Field-Effect Tunneling Transistor Based on Vertical Graphene Heterostructures. *Science (80-.).* **335**, 947–951 (2012).

15.   Fang, H., Battaglia, C., Carraro, C., Nemsak, S., Ozdol, B., Kang, J. S., *et al.* Strong interlayer coupling in van der Waals heterostructures built from single-layer chalcogenides. *Proc. Natl. Acad. Sci. U. S. A.* **111**, 6198–6202 (2014).

16.   Wang, F., Wang, Z., Xu, K., Wang, F., Wang, Q., Huang, Y., *et al.* Tunable GaTe-MoS$_2$ van der Waals p-n Junctions with Novel Optoelectronic Performance. *Nano Lett.* **15**, 7558–7566 (2015).

17.   Cheng, R., Li, D., Zhou, H., Wang, C., Yin, A., Jiang, S., *et al.* Electroluminescence and photocurrent generation from atomically sharp WSe$_2$/MoS$_2$ heterojunction p-n diodes. *Nano Lett.* **14**, 5590–5597 (2014).

18.   Frisenda, R., Navarro-Moratalla, E., Gant, P., Pérez De Lara, D., Jarillo-Herrero, P., Gorbachev, R. V. & Castellanos-Gomez, A. Recent progress in the assembly of nanodevices and van der Waals heterostructures by deterministic placement of 2D materials. *Chem. Soc. Rev.* **47**, 53–68 (2018).

19.   Shi, Y., Li, H. & Li, L. J. Recent advances in controlled synthesis of two-dimensional transition metal dichalcogenides via vapour deposition techniques. *Chem. Soc. Rev.* **44**, 2744–2756 (2015).

20.   Choi, W., Choudhary, N., Han, G. H., Park, J., Akinwande, D. & Lee, Y. H. Recent development of two-dimensional transition metal dichalcogenides and their applications. *Mater. Today* **20**, 116–130 (2017).

References

21. Chhowalla, M., Shin, H. S., Eda, G., Li, L. J., Loh, K. P. & Zhang, H. The chemistry of two-dimensional layered transition metal dichalcogenide nanosheets. *Nat. Chem.* **5**, 263–275 (2013).

22. Liu, G.-B., Xiao, D., Yao, Y., Xu, X. & Yao, W. Electronic structures and theoretical modelling of two-dimensional group-VIB transition metal dichalcogenides. *Chem. Soc. Rev.* **44**, 2643–2663 (2015).

23. Wang, Q. H., Kalantar-Zadeh, K., Kis, A., Coleman, J. N. & Strano, M. S. Electronics and optoelectronics of two-dimensional transition metal dichalcogenides. *Nat. Nanotechnol.* **7**, 699–712 (2012).

24. Tan, P. *Raman Spectroscopy of Two- Dimensional Materials*. (Springer Nature Singapore Pte Ltd., 2019). doi:https://doi.org/10.1007/978-981-13-1828-3_12

25. Suzuki, R., Sakano, M., Zhang, Y. J., Akashi, R., Morikawa, D., Harasawa, A., *et al.* Valley-dependent spin polarization in bulk MoS_2 with broken inversion symmetry. *Nat. Nanotechnol.* **9**, 611 (2014).

26. Ribeiro-Soares, J., Almeida, R. M., Barros, E. B., Araujo, P. T., Dresselhaus, M. S., Cançado, L. G. & Jorio, A. Group theory analysis of phonons in two-dimensional transition metal dichalcogenides. *Phys. Rev. B - Condens. Matter Mater. Phys.* **90**, (2014).

27. Hofmann, P. & Jensen, E. *Surface Physics: An Introduction. Springer Handbooks* (Philip Hofmann, 2013, 2006). doi:10.1007/978-0-387-26308-3_89

28. Yazyev, O. V. & Kis, A. MoS_2 and semiconductors in the flatland. *Mater. Today* **18**, 20–30 (2015).

29. Mak, K. F., Lee, C., Hone, J., Shan, J. & Heinz, T. F. Atomically thin MoS_2: A new direct-gap semiconductor. *Phys. Rev. Lett.* **105**, 2–5 (2010).

30. Splendiani, A., Sun, L., Zhang, Y., Li, T., Kim, J., Chim, C. Y., *et al.* Emerging photoluminescence in monolayer MoS_2. *Nano Lett.* **10**, 1271–1275 (2010).

31. Tongay, S., Zhou, J., Ataca, C., Lo, K., Matthews, T. S., Li, J., *et al.* Thermally

driven crossover from indirect toward direct bandgap in 2D Semiconductors: MoSe$_2$ versus MoS$_2$. *Nano Lett.* **12**, 5576–5580 (2012).

32.   Zhao, W., Ghorannevis, Z., Chu, L., Toh, M., Kloc, C., Tan, P. H. & Eda, G. Evolution of electronic structure in atomically thin sheets of WS$_2$ and WSe$_2$. *ACS Nano* **7**, 791–797 (2013).

33.   Huang, Y. L., Chen, Y., Zhang, W., Quek, S. Y., Chen, C. H., Li, L. J., *et al.* Bandgap tunability at single-layer molybdenum disulphide grain boundaries. *Nat. Commun.* **6**, (2015).

34.   Bradley, A. J., Ugeda, M. M., Da Jornada, F. H., Qiu, D. Y., Ruan, W., Zhang, Y., *et al.* Probing the Role of Interlayer Coupling and Coulomb Interactions on Electronic Structure in Few-Layer MoSe$_2$ Nanostructures. *Nano Lett.* **15**, 2594–2599 (2015).

35.   Wilson, N. R., Nguyen, P. V., Seyler, K., Rivera, P., Marsden, A. J., Laker, Z. P. L., *et al.* Determination of band offsets, hybridization, and exciton binding in 2D semiconductor heterostructures. *Sci. Adv.* **3**, 1–8 (2017).

36.   Picasso, L. E. *Lectures in Quantum Mechanics*. **3**, (Springer International Publishing AG Switzerland, 2010).

37.   Hosmane, N. S. Chapter 1 – Electronic Structure: Quantum Theory Revisited. in *Advanced Inorganic Chemistry* 3–13 (Academic Press, 2017). doi:10.1016/B978-0-12-801982-5.00001-1

38.   Zhu, Z. Y., Cheng, Y. C. & Schwingenschlögl, U. Giant spin-orbit-induced spin splitting in two-dimensional transition-metal dichalcogenide semiconductors. *Phys. Rev. B - Condens. Matter Mater. Phys.* **84**, 1–5 (2011).

39.   Wang, G., Robert, C., Suslu, A., Chen, B., Yang, S., Alamdari, S., *et al.* Spin-orbit engineering in transition metal dichalcogenide alloy monolayers. *Nat. Commun.* **6**, 1–7 (2015).

40.   Feng, Q., Zhu, Y., Hong, J., Zhang, M., Duan, W., Mao, N., *et al.* Growth of

References

large-area 2D $MoS_{2(1-x)}Se_{2x}$ semiconductor alloys. *Adv. Mater.* **26**, 2648–2653 (2014).

41.   Zhu, B., Zeng, H., Dai, J., Gong, Z. & Cui, X. Anomalously robust valley polarization and valley coherence in bilayer WS_2. *Proc. Natl. Acad. Sci. U. S. A.* **111**, 11606–11611 (2014).

42.   Xiao, D., Liu, G.-B., Feng, W., Xu, X. & Yao, W. Coupled Spin and Valley Physics in Monolayers of MoS_2 and Other Group-VI Dichalcogenides. *Phys. Rev. Lett.* **108**, 196802 (2012).

43.   Xu, X., Yao, W., Xiao, D. & Heinz, T. F. Spin and pseudospins in layered transition metal dichalcogenides. *Nat. Phys.* **10**, 343–350 (2014).

44.   Cao, T., Wang, G., Han, W., Ye, H., Zhu, C., Shi, J., *et al.* Valley-selective circular dichroism of monolayer molybdenum disulphide. *Nat. Commun.* **3**, (2012).

45.   Green, M. A., Ho-Baillie, A. & Snaith, H. J. The emergence of perovskite solar cells. *Nat. Photonics* **8**, 506–514 (2014).

46.   Choi, W., Cho, M. Y., Konar, A., Lee, J. H., Cha, G. B., Hong, S. C., *et al.* High-detectivity multilayer MoS_2 phototransistors with spectral response from ultraviolet to infrared. *Adv. Mater.* **24**, 5832–5836 (2012).

47.   Radisavljevic, B., Radenovic, A., Brivio, J., Giacometti, V. & Kis, A. Single-layer MoS_2 transistors. *Nat. Nanotechnol.* **6**, 147–150 (2011).

48.   Yu, W. J., Liu, Y., Zhou, H., Yin, A., Li, Z., Huang, Y. & Duan, X. Highly efficient gate-tunable photocurrent generation in vertical heterostructures of layered materials. *Nat. Nanotechnol.* **8**, 952–958 (2013).

49.   Wang, J., Fang, H., Wang, X., Chen, X., Lu, W. & Hu, W. Recent Progress on Localized Field Enhanced Two-dimensional Material Photodetectors from Ultraviolet—Visible to Infrared. *Small* **13**, 1–17 (2017).

50.   Lee, C. H., Lee, G. H., Van Der Zande, A. M., Chen, W., Li, Y., Han, M., *et al.*

Atomically thin p-n junctions with van der Waals heterointerfaces. *Nat. Nanotechnol.* **9**, 676–681 (2014).

51.   Long, M., Gao, A., Wang, P., Xia, H., Ott, C., Pan, C., *et al.* Room temperature high-detectivity mid-infrared photodetectors based on black arsenic phosphorus. *Sci. Adv.* **3**, 1–8 (2017).

52.   Liu, B., Köpf, M., Abbas, A. N., Wang, X., Guo, Q., Jia, Y., *et al.* Black Arsenic-Phosphorus: Layered Anisotropic Infrared Semiconductors with Highly Tunable Compositions and Properties. *Adv. Mater.* **27**, 4423–4429 (2015).

53.   Jin, Y., Keum, D. H., An, S. J., Kim, J., Lee, H. S. & Lee, Y. H. A Van der Waals Homojunction: Ideal p-n Diode Behavior in $MoSe_2$. *Adv. Mater.* **27**, 5534–5540 (2015).

54.   Zhang, M., Wu, J., Zhu, Y., Dumcenco, D. O., Hong, J., Mao, N., *et al.* Two-dimensional molybdenum tungsten diselenide alloys: Photoluminescence, Raman scattering, and electrical transport. *ACS Nano* **8**, 7130–7137 (2014).

55.   Zheng, S., Sun, L., Yin, T., Dubrovkin, A. M., Liu, F., Liu, Z., *et al.* Monolayers of $W_xMo_{1-x}S_2$ alloy heterostructure with in-plane composition variations. *Appl. Phys. Lett.* **106**, (2015).

56.   Chen, Y., Xi, J., Dumcenco, D. O., Liu, Z., Suenaga, K., Wang, D., *et al.* Tunable Band Gap Photoluminescence from Atomically Thin Transition-Metal Dichalcogenide Alloys. *ACS Nano* **7**, 4610–4616 (2013).

57.   Tongay, S., Narang, D. S., Kang, J., Fan, W., Ko, C., Luce, A. V., *et al.* Two-dimensional semiconductor alloys: Monolayer $Mo_{1-x}W_xSe_2$. *Appl. Phys. Lett.* **104**, (2014).

58.   Li, H., Duan, X., Wu, X., Zhuang, X., Zhou, H., Zhang, Q., *et al.* Growth of alloy $MoS_{2x}Se_{2(1-x)}$ nanosheets with fully tunable chemical compositions and optical properties. *J. Am. Chem. Soc.* **136**, 3756–3759 (2014).

59.   Feng, L. P., Jiang, W. Z., Su, J., Zhou, L. Q. & Liu, Z. T. Performance of field-

effect transistors based on $Nb_xW_{1-x}S_2$ monolayers. *Nanoscale* **8**, 6507–6513 (2016).

60. Azizi, A., Wang, Y., Lin, Z., Wang, K., Elias, A. L., Terrones, M., *et al.* Spontaneous Formation of Atomically Thin Stripes in Transition Metal Dichalcogenide Monolayers. *Nano Lett.* **16**, 6982–6987 (2016).

61. Isshiki, M. & Wang, J. Wide-Bandgap II-VI Semiconductors: Growth and Properties BT - Springer Handbook of Electronic and Photonic Materials. in *Springer Handbook of Electronic and Photonic Materials* (eds. Ruda, H. E. & Matsuura, N.) 1 (Springer International Publishing, 2017). doi:10.1007/978-3-319-48933-9_16

62. Lieth, R. M. A. *Preparation and Crystal Growth of Materials with Layered Structures*. (Springer Netherlands, 1977). doi:10.1007/978-94-017-2750-1

63. Lenz, M. & Gruehn, R. Developments in Measuring and Calculating Chemical Vapor Transport Phenomena Demonstrated on Cr, Mo, W, and Their Compounds. *Chem. Rev.* **2665**, (1997).

64. Duan, X., Wang, C., Fan, Z., Hao, G., Kou, L., Halim, U., *et al.* Synthesis of $WS_{2x}Se_{2-2x}$ Alloy Nanosheets with Composition-Tunable Electronic Properties. *Nano Lett.* **16**, 264–269 (2016).

65. Niu, Y., Gonzalez-Abad, S., Frisenda, R., Marauhn, P., Drüppel, M., Gant, P., *et al.* Thickness-dependent differential reflectance spectra of monolayer and few-layer MoS_2, $MoSe_2$, WS_2 and WSe_2. *Nanomaterials* **8**, (2018).

66. Kim, J. G., Yun, W. S., Jo, S., Lee, J. & Cho, C. H. Effect of interlayer interactions on exciton luminescence in atomic-layered MoS_2 crystals. *Sci. Rep.* **6**, 1–7 (2016).

67. Zeng, H., Liu, G. Bin, Dai, J., Yan, Y., Zhu, B., He, R., *et al.* Optical signature of symmetry variations and spin-valley coupling in atomically thin tungsten dichalcogenides. *Sci. Rep.* **3**, 2–6 (2013).

68.   Xu, H., Zhu, J., Zou, G., Liu, W., Li, X., Li, C., *et al.* Spatially Bandgap-Graded $MoS_{2(1-x)}Se_{2x}$ Homojunctions for Self-Powered Visible Near-Infrared Phototransistors. *Nano-Micro Lett.* **12**, 1–14 (2020).

69.   Blake, P., Hill, E. W., Castro Neto, A. H., Novoselov, K. S., Jiang, D., Yang, R., *et al.* Making graphene visible. *Appl. Phys. Lett.* **91**, (2007).

70.   Velický, M., Donnelly, G. E., Hendren, W. R., McFarland, S., Scullion, D., Debenedetti, W. J. I., *et al.* Mechanism of Gold-Assisted Exfoliation of Centimeter-Sized Transition-Metal Dichalcogenide Monolayers. *ACS Nano* **12**, 10463–10472 (2018).

71.   Huang, Y., Sutter, E., Shi, N. N., Zheng, J., Yang, T., Englund, D., *et al.* Reliable Exfoliation of Large-Area High-Quality Flakes of Graphene and Other Two-Dimensional Materials. *ACS Nano* **9**, 10612–10620 (2015).

72.   Powell, R. C. *Symmetry , Group Theory , and the Physical Properties of Crystals*. (Springer Science+Business Media, 2010). doi:10.1007/978-1-4419-7598-0

73.   Toporski, J., Dieing, T. & Hollricher, O. *Confocal Raman Microscopy*. *Confocal Raman Microscopy* **66**, (Springer International Publishing AG, 2018).

74.   Wolverson, D. *Raman Spectroscopy*. *Characterization of Semiconductor Heterostructures and Nanostructures* (Elsevier B.V., 2013). doi:10.1016/B978-0-444-59551-5.00017-0

75.   Long, D. A. *The Raman effect*. *The Raman Effect: A Unified Treatment of the Theory of Raman Scattering by Molecules.* **8**, (John Wiley & Sons Ltd, 2002).

76.   Ferraro, J. R., Nakamoto, K. & Brown, C. W. Basic theory. in *Introductory Raman Spectroscopy* 1–73 (Elsevier Science USA, 2003). doi:10.4324/9780203405970-2

77.   Wu, J., Mao, N., Xie, L., Xu, H. & Zhang, J. Identifying the crystalline orientation of black phosphorus using angle-resolved polarized Raman

spectroscopy. *Angew. Chemie - Int. Ed.* **54**, 2366–2369 (2015).

78.   Yang, S., Yang, Y., Wu, M., Hu, C., Shen, W., Gong, Y., *et al.* Highly In-Plane Optical and Electrical Anisotropy of 2D Germanium Arsenide. *Adv. Funct. Mater.* **28**, 1–10 (2018).

79.   Zhang, X., Qiao, X.-F., Shi, W., Wu, J.-B., Jiang, D.-S. & Tan, P.-H. Phonon and Raman scattering of two-dimensional transition metal dichalcogenides from monolayer, multilayer to bulk material. *Chem. Soc. Rev.* **44**, 2757–2785 (2015).

80.   Lee, C., Yan, H., Brus, L. E., Heinz, T. F., Hone, J. & Ryu, S. Anomalous lattice vibrations of single- and few-layer MoS_2. *ACS Nano* **4**, 2695–2700 (2010).

81.   Loudon, R. The Raman effect in crystals. *Adv. Phys.* **50**, 813–864 (2001).

82.   Williams, D. B. & Carter, B. C. *Transmission Electron Microscopy: A Textbook for Materials Science*. (Springer US, 2009). doi:https://doi.org/10.1007/978-0-387-76501-3

83.   Inkson, B. J. *Scanning Electron Microscopy (SEM) and Transmission Electron Microscopy (TEM) for Materials Characterization. Materials Characterization Using Nondestructive Evaluation (NDE) Methods* (Elsevier Ltd, 2016). doi:10.1016/B978-0-08-100040-3.00002-X

84.   Goodhew, P. J. General Introduction to Transmission Electron Microscopy. in *Aberration-Corrected Analytical Transmission Electron Microscopy* (ed. Brydson, R.) 1–19 (John Wiley & Sons, Ltd., 2011). doi:10.1002/9781119978848.ch1

85.   Wang, Z. L. Transmission electron microscopy of shape-controlled nanocrystals and their assemblies. *J. Phys. Chem. B* **104**, 1153–1175 (2000).

86.   Egerton, R. F. *Physical Principles of Electron Microscopy*. (Springer Science+Business Media, Inc., 2005).

87.   Correction, L. A. D. and. Lens Aberrations: Diagnosis and Correction. in *Aberration-Corrected Analytical Transmission Electron Microscopy* (ed.

Brydson, R.) 55–87 (John Wiley & Sons, Ltd., 2003).

88. Krivanek, O. L., Dellby, N. & Lupini, A. R. Towards sub-Å electron beams. *Ultramicroscopy* **78**, 1–11 (1999).

89. Tatlock, G. Introduction to Electron Optics Gordon. in *Aberration-Corrected Analytical Transmission Electron Microscopy* (ed. Brydson, R.) 21–38 (John Wiley & Sons, Ltd. Published, 2011).

90. Zemlin, F., Weiss, K., Schiske, P., Kunath, W. & Herrmann, K. H. Coma-free alignment of high resolution electron microscopes with the aid of optical diffractograms. *Ultramicroscopy* **3**, 49–60 (1978).

91. Tizei, L. H. G., Lin, Y. C., Lu, A. Y., Li, L. J. & Suenaga, K. Electron energy loss spectroscopy of excitons in two-dimensional-semiconductors as a function of temperature. *Appl. Phys. Lett.* **108**, (2016).

92. Tizei, L. H. G., Lin, Y. C., Mukai, M., Sawada, H., Lu, A. Y., Li, L. J., *et al.* Exciton Mapping at Subwavelength Scales in Two-Dimensional Materials. *Phys. Rev. Lett.* **114**, 1–5 (2015).

93. Egerton, R. F., Li, P. & Malac, M. Radiation damage in the TEM and SEM. *Micron* **35**, 399–409 (2004).

94. Egerton, R. F. Control of radiation damage in the TEM. *Ultramicroscopy* **127**, 100–108 (2013).

95. Lv, B., Qian, T. & Ding, H. Angle-resolved photoemission spectroscopy and its application to topological materials. *Nat. Rev. Phys.* **1**, 609–626 (2019).

96. Damascelli, A., Hussain, Z. & Shen, Z. X. Angle-resolved photoemission studies of the cuprate superconductors. *Rev. Mod. Phys.* **75**, 473–541 (2003).

97. Kim, B. S., Rhim, J. W., Kim, B., Kim, C. & Park, S. R. Determination of the band parameters of bulk 2H-MX_2 (M = Mo, W; X = S, Se) by angle-resolved photoemission spectroscopy. *Sci. Rep.* **6**, 36389 (2016).

98. Zhang, Y., Chang, T. R., Zhou, B., Cui, Y. T., Yan, H., Liu, Z., *et al.* Direct observation of the transition from indirect to direct bandgap in atomically thin epitaxial MoSe$_2$. *Nat. Nanotechnol.* **9**, 111–115 (2014).

99. Sallen, G., Bouet, L., Marie, X., Wang, G., Zhu, C. R., Han, W. P., *et al.* Robust optical emission polarization in MoS$_2$ monolayers through selective valley excitation. *Phys. Rev. B - Condens. Matter Mater. Phys.* **86**, 3–6 (2012).

100. Lopez-Sanchez, O., Lembke, D., Kayci, M., Radenovic, A. & Kis, A. Ultrasensitive photodetectors based on monolayer MoS$_2$. *Nat. Nanotechnol.* **8**, 497–501 (2013).

101. Mak, K. F., McGill, K. L., Park, J. & McEuen, P. L. Valleytronics. The valley Hall effect in MoS$_2$ transistors. *Science (80-.).* **344**, 1489–1492 (2014).

102. Haigh, D. G., Soin, R. S. & J.Wood. *Strained Silicon Heterostructures: materials and devices*. *Strained Silicon Heterostructures: materials and devices* (2001). doi:10.1049/pbcs012e

103. Material Science BT - Silicon Quantum Integrated Circuits: Silicon-Germanium Heterostructure Devices: Basics and Realisations. in (eds. Kasper, E. & Paul, D. J.) 13–47 (Springer Berlin Heidelberg, 2005). doi:10.1007/3-540-26382-9_2

104. Wang, G., Robert, C., Suslu, A., Chen, B., Yang, S., Alamdari, S., *et al.* Spin-orbit engineering in transition metal dichalcogenide alloy monolayers. *Nat. Commun.* **6**, 10110 (2015).

105. Riley, J. M., Mazzola, F., Dendzik, M., Michiardi, M., Takayama, T., Bawden, L., *et al.* Direct observation of spin-polarized bulk bands in an inversion-symmetric semiconductor. *Nat. Phys.* **10**, 835 (2014).

106. Sasaki, S., Kobayashi, Y., Liu, Z., Suenaga, K., Maniwa, Y., Miyauchi, Y. & Miyata, Y. Growth and optical properties of Nb-doped WS$_2$ monolayers. *Appl. Phys. Express* **9**, 071201 (2016).

107. Pam, M. E., Hu, J., Ang, Y. S., Huang, S., Kong, D., Shi, Y., *et al.* High-

Concentration Niobium-Substituted WS_2 Basal Domains with Reconfigured Electronics Band Structure for Hydrogen Evolution Reaction. *ACS Appl. Mater. Interfaces* acsami.9b08232 (2019). doi:10.1021/acsami.9b08232

108. Kalikhman, V. L. Features of crystal structure, electrophysical properties and spectrum model of valence bands of MoS_2 type laminated compounds. *Izv Akad Nauk SSSR, Neorg Mater* **19**, 1060–1065 (1983).

109. Schutte, W. J., De Boer, J. L. & Jellinek, F. Crystal structures of tungsten disulfide and diselenide. *J. Solid State Chem.* **70**, 207–209 (1987).

110. Scherrer, P. Bestimmung der inneren Struktur und der Größe von Kolloidteilchen mittels Röntgenstrahlen BT - Kolloidchemie Ein Lehrbuch. in (ed. Zsigmondy, R.) 387–409 (Springer Berlin Heidelberg, 1912). doi:10.1007/978-3-662-33915-2_7

111. Langford, J. I. & Wilson, A. J. C. Scherrer after sixty years: A survey and some new results in the determination of crystallite size. *J. Appl. Crystallogr.* **11**, 102–113 (1978).

112. Klug, H. P. & Alexander, L. E. *X-Ray Diffraction Procedures for Polycrystalline and Amorphous Materials*. (John Wiley & Sons, 1974).

113. Bish, D. L. & Post, J. E. *Modern Powder Diffraction*. (Mineralogical Society of America, 1989).

114. Romanenko, A. I., Yakovleva, G. E., Fedorov, V. E., Ledneva, A. Y., Kuznetsov, V. A., Sotnikov, A. V., *et al.* Electron transport properties of thermoelectrics based on layered substituted transition metal dichalcogenides. *J. Struct. Chem.* **58**, 893–900 (2017).

115. Baglio, J., Kamieniecki, E., Decola, N., Struck, C., Marzik, J., Dwight, K. & Wold, A. Growth and Characterization Single Crystals and Niobium-Doped p-WS_2 single crystals. *J. Solid State Chem.* **49**, 166–179 (1983).

116. Legma, J. B., Vacquier, G. & Casalot, A. Chemical vapour transport of

molybdenum and tungsten diselenides by various transport agents. *J. Cryst. Growth* **130**, 253–258 (1993).

117. Physics, A. & Hills, P. The growth and thermodynamical feasibility of tungsten diselenide single crystals using chemical vapour transport technique. *Bull. Mater. SCi* **20**, 231–238 (1997).

118. Pizzocchero, F., Gammelgaard, L., Jessen, B. S., Caridad, J. M., Wang, L., Hone, J., *et al.* The hot pick-up technique for batch assembly of van der Waals heterostructures. *Nat. Commun.* **7**, (2016).

119. Dean, C. R., Young, A. F., Meric, I., Lee, C., Wang, L., Sorgenfrei, S., *et al.* Boron nitride substrates for high-quality graphene electronics. *Nat. Nanotechnol.* **5**, 722–726 (2010).

120. Zan, R., Ramasse, Q. M., Jalil, R., Georgiou, T., Bangert, U. & Novoselov, K. S. Control of radiation damage in MoS_2 by graphene encapsulation. *ACS Nano* **7**, 10167–10174 (2013).

121. Algara-Siller, G., Kurasch, S., Sedighi, M., Lehtinen, O. & Kaiser, U. The pristine atomic structure of MoS_2 monolayer protected from electron radiation damage by graphene. *Appl. Phys. Lett.* **103**, (2013).

122. Wilson, N. R., Marsden, A. J., Saghir, M., Bromley, C. J., Schaub, R., Costantini, G., *et al.* Weak mismatch epitaxy and structural Feedback in graphene growth on copper foil. *Nano Res.* **6**, 99–112 (2013).

123. Dumcenco, D. O., Kobayashi, H., Liu, Z., Huang, Y. & Suenaga, K. Visualization and quantification of transition metal atomic mixing in $Mo_{1-x}W_xS_2$ single layers. *Nat. Commun.* **4**, 1351 (2013).

124. Kormányos, A., Burkard, G., Gmitra, M., Fabian, J., Zólyomi, V., Drummond, N. D. & Fal'Ko, V. K.p theory for two-dimensional transition metal dichalcogenide semiconductors. *2D Mater.* **2**, 022001 (2015).

125. Traill, R. J. A rhombohedral polytype of molybdenite. *Can. Mineral.* **7**, 524–526

(1963).

126. Bronsema, K. D., De Boer, J. L. & Jellinek, F. On the structure of molybdenum diselenide and disulfide. *J. Inorg. Gen. Chem.* **540**, 15–17 (1986).

127. Dumcenco, D. O., Chen, K. Y., Wang, Y. P., Huang, Y. S. & Tiong, K. K. Raman study of 2H-$Mo_{1-x}W_xS_2$ layered mixed crystals. *J. Alloys Compd.* **506**, 940–943 (2010).

128. Chen, Y., Dumcenco, D. O., Zhu, Y., Zhang, X., Mao, N., Feng, Q., *et al.* Composition-dependent Raman modes of $Mo_{1-x}W_xS_2$ monolayer alloys. *Nanoscale* **6**, 2833–2839 (2014).

129. Wang, Z., Liu, P., Ito, Y., Ning, S., Tan, Y., Fujita, T., *et al.* Chemical Vapor Deposition of Monolayer $Mo_{1-x}W_xS_2$ Crystals with Tunable Band Gaps. *Sci. Rep.* **6**, 21536 (2016).

130. Gao, J., Li, B., Tan, J., Chow, P., Lu, T. & Koratkar, N. Aging of Transition Metal Dichalcogenide. *ACS Nano* (2016). doi:10.1021/acsnano.5b07677

131. Dyson, M. A. Advances in computational methods for transmission electron microscopy simulation and image processing. *PhD thesis, University of Warwick.* (2014). Available at: https://jjppeters.github.io/clTEM/.

132. J. M. Cowley. Short- and Long-Range Order Parameters in Disordered Solid Solutions. *Phys. Rev.* **120**, 1648 (1960).

133. Cowley, J. M. X-Ray Measurement of Order in Single Crystals of Cu_3Au. *J. Appl. Phys.* **21**, 24 (1964).

134. Ising, E. Beitrag zur Theorie des Ferromagnetismus. *Zeitschrift für Phys.* **31**, 253–258 (1925).

135. Zhang, S. B. & Northrup, J. E. Chemical Potential Dependence of Defect Formation Energies in GaAs: Application to Ga Self-Diffusion. *Phys. Rev. Lett.* **67**, 2339–2342 (1991).

136. Strocov, V. N. Intrinsic accuracy in 3-dimensional photoemission band mapping. *J. Electron Spectros. Relat. Phenomena* **130**, 65–78 (2003).

137. Eknapakul, T., King, P. D. C., Asakawa, M., Buaphet, P., He, R.-H., Mo, S.-K., *et al.* Electronic Structure of a Quasi-Freestanding MoS_2 Monolayer. *Nano Lett.* **14**, 1312–1316 (2014).

138. Kang, M., Kim, B., Ryu, S. H., Jung, S. W., Kim, J., Moreschini, L., *et al.* Universal Mechanism of Band-Gap Engineering in Transition-Metal Dichalcogenides. *Nano Lett.* **17**, 1610–1615 (2017).

139. Clark, S. J., Segall, M. D., Pickard, C. J., Hasnip, P. J., Probert, M. J., Refson, K. & Payne, M. C. First principles methods using CASTEP. *Zeitschrift für Krist.* **220**, 567–570 (2005).

140. Perdew, J. P., Burke, K. & Ernzerhof, M. Generalized Gradient Approximation Made Simple. *Phys. Rev. Lett.* **77**, 3865–3868 (1996).

141. Chris-Kriton Skylaris, Haynes, P. D., Mostof, A. A. & Payne, M. C. Introducing ONETEP : Linear-scaling density functional simulations on parallel computers. *J. Chem. Phys.* **122**, 084119 (2005).

142. Blöchl, P. E. Projector augmented-wave method. *Phys. Rev. B* **50**, 17953 (1994).

143. Kresse, G. & Joubert, D. From ultrasoft pseudopotentials to the projector augmented-wave method. *Phys. Rev. B* **59**, 1758–1775 (1999).

144. Jollet, F., Torrent, M. & Holzwarth, N. Generation of Projector Augmented-Wave atomic data: A 71 element validated table in the XML format. *Comput. Phys. Commun.* **185**, 1246–1254 (2014).

145. Popescu, V. & Zunger, A. Extracting E versus k effective band structure from supercell calculations on alloys and impurities (a) periodic compound. *Phys. Rev. B* **85**, 085201 (2012).

146. Constantinescu, G. C. & Hine, N. D. M. Energy landscape and band-structure tuning in realistic MoS_2/$MoSe_2$ heterostructures. *Phys. Rev. B* **91**, 195416

(2015).

147. Nordheim, L. Zur Elektronentheorie der Metalle. I. *Ann. Phys.* **401**, 607–640 (1931).

148. Muto, T. On the electronic structure of alloys. *Sci. Pap. Inst. Phys. Chem. Res.* **34**, 37 (1938).

149. Giannozzi, P., Baroni, S., Bonini, N., Calandra, M., Car, R., Cavazzoni, C., *et al.* QUANTUM ESPRESSO : a modular and open-source software project for quantum simulations of materials. *J. Phys. Condens. Matter* **21**, 395502 (2009).

150. Giannozzi, P., Andreussi, O., Brumme, T., Bunau, O., Buongiorno Nardelli, M., Calandra, M., *et al.* Advanced capabilities for materials modelling with Quantum ESPRESSO. *J. Phys. Condens. Matter* **29**, 465901 (2017).

151. Nguyen, P. V., Teutsch, N. C., Wilson, N. P., Kahn, J., Xia, X., Graham, A. J., *et al.* Visualizing electrostatic gating effects in two-dimensional heterostructures. *Nature* **572**, 220–223 (2019).

152. Xi, J., Zhao, T., Wang, D. & Shuai, Z. Tunable Electronic Properties of Two-Dimensional Transition Metal Dichalcogenide Alloys: A First-Principles Prediction. *J. Phys. Chem. Lett.* **5**, 285–291 (2014).

153. Yao, W., Xiao, D. & Niu, Q. Valley-dependent optoelectronics from inversion symmetry breaking. *Phys. Rev. B* **77**, 235406 (2008).

154. Jin, Y., Zeng, Z., Xu, Z., Lin, Y. C., Bi, K., Shao, G., *et al.* Synthesis and Transport Properties of Degenerate P-Type Nb-Doped WS_2 Monolayers. *Chem. Mater.* **31**, 3534–3541 (2019).

155. Tongay, S., Narang, D. S., Kang, J., Fan, W., Ko, C., Luce, A. V, *et al.* Two-dimensional semiconductor alloys: Monolayer $Mo_{1-x}W_xSe_2$. *Appl. Phys. Lett.* **104**, 12101 (2014).

156. Bougouma, M., Guel1, B., Segato, T., Legma, J. B. & Ogletree, M.-P. D. The Structure of Niobium-Doped $MoSe_2$ and WSe_2. *Bull. Chem. Soc. Ethiop.* **22**,

225–236 (2008).

157. Chen, S., Bharathi, M. S., Gao, J., Zhang, G. & Zhang, Y. Etching mechanisms , kinetics, and pattern formation in multilayered. *Mater. Today Adv.* **7**, 100075 (2020).

158. Zhu, D., Shu, H., Jiang, F. & Lv, D. Capture the growth kinetics of CVD growth of two-dimensional MoS$_2$. *npj 2D Mater. Appl.* 1–7 (2017). doi:10.1038/s41699-017-0010-x

159. Malgrange, C., Ricolleau, C. & Schlenker, M. *Symmetry and Physical Properties of Crystals*. (Springer Dordrecht Heidelberg, 2011). doi:10.1007/978-94-017-8993-6

160. Chenet, D. A., Aslan, O. B., Huang, P. Y., Fan, C., Van Der Zande, A. M., Heinz, T. F. & Hone, J. C. In-Plane Anisotropy in Mono- and Few-Layer ReS$_2$ Probed by Raman Spectroscopy and Scanning Transmission Electron Microscopy. *Nano Lett.* **15**, 5667–5672 (2015).

161. Yang, Y., Liu, S. C., Wang, Y., Long, M., Dai, C. M., Chen, S., *et al.* In-Plane Optical Anisotropy of Low-Symmetry 2D GeSe. *Adv. Opt. Mater.* **7**, 1–8 (2019).

162. Ribeiro, H. B., Pimenta, M. A., De Matos, C. J. S., Moreira, R. L., Rodin, A. S., Zapata, J. D., *et al.* Unusual angular dependence of the Raman response in black phosphorus. *ACS Nano* **9**, 4270–4276 (2015).

163. Song, Q., Wang, H., Pan, X., Xu, X., Wang, Y. & Li, Y. Anomalous in-plane anisotropic Raman response of monoclinic semimetal 1 T′-MoTe$_2$. *Sci. Rep.* **1**, 1758 (2017).

164. Zhang, X., Tan, Q.-H., Wu, J.-B., Shi, W. & Tan, P.-H. Review on the Raman spectroscopy of different types of layered materials. *Nanoscale* **8**, 6435–6450 (2016).

165. Saito, R., Tatsumi, Y., Huang, S., Ling, X. & Dresselhaus, M. S. Raman spectroscopy of transition metal dichalcogenides. *J. Phys. Condens. Matter* **28**,

(2016).

166. Online, V. A., Liang, L. & Meunier, V. First-principles Raman spectra of MoS_2, WS_2 and their heterostructures. *Nanoscale* **6**, 5394–5401 (2014).

167. Berkdemir, A., Gutiérrez, H. R., Botello-Méndez, A. R., Perea-López, N., Elías, A. L., Chia, C.-I., *et al.* Identification of individual and few layers of WS_2 using Raman Spectroscopy. *Sci. Rep.* **3**, 1755 (2013).

168. Nakashima, S., Tokuda, Y., Mitsuishi, A., Aoki, R. & Hamaue, Y. Raman scattering from $2H-NbS_2$ and intercalated NbS_2. *Solid State Commun.* **42**, 601–604 (1982).

169. Wang, X., Lin, J., Zhu, Y., Luo, C., Suenaga, K., Cai, C. & Xie, L. Chemical vapor deposition of trigonal prismatic NbS_2 monolayers and 3R-polytype few-layers. *Nanoscale* **9**, 16607–16611 (2017).

170. Gao, J., Kim, Y. D., Liang, L., Idrobo, J. C., Chow, P., Tan, J., *et al.* Transition-Metal Substitution Doping in Synthetic Atomically Thin Semiconductors. *Adv. Mater.* **28**, 9735–9743 (2016).

171. Kim, A. R., Kim, Y., Nam, J., Chung, H., Kim, D. J., Kwon, J., *et al.* Alloyed 2D Metal − Semiconductor Atomic Layer Junctions. *Nano Lett.* 10–15 (2016). doi:10.1021/acs.nanolett.5b05036

172. Terrones, H., Corro, E. Del, Feng, S., Poumirol, J. M., Rhodes, D., Smirnov, D., *et al.* New First Order Raman-active Modes in Few Layered Transition Metal. *Sci. Rep.* **22**, 1–9 (2014).

173. Böer, K. W. & Pohl, U. W. *Semiconductor Physics*. (Springer International Publishing, 2018). doi:10.1007/978-3-319-69150-3

174. Xin, Z., Zeng, L., Wang, Y., Wei, K., Du, G., Kang, J. & Liu, X. Strain affected electronic properties of bilayer tungsten disulfide. *Jpn. J. Appl. Phys.* **53**, 2–7 (2014).

175. Jin, Z., Li, X., Mullen, J. T. & Kim, K. W. Intrinsic transport properties of

electrons and holes in monolayer transition-metal dichalcogenides. *Phys. Rev. B* **045422**, 1–7 (2014).

176. Krivanek, O. L., Lovejoy, T. C., Dellby, N., Aoki, T., Carpenter, R. W., Rez, P., *et al.* Vibrational spectroscopy in the electron microscope. *Nature* **514**, 209–212 (2014).

177. Moynihan, E., Rost, S., O'connell, E., Ramasse, Q., Friedrich, C. & Bangert, U. Plasmons in MoS_2 studied via experimental and theoretical correlation of energy loss spectra. *J. Microsc.* **279**, 256–264 (2020).

178. Wang, L., Wang, Z., Wang, H. Y., Grinblat, G., Huang, Y. L., Wang, D., *et al.* Slow cooling and efficient extraction of C-exciton hot carriers in MoS_2 monolayer. *Nat. Commun.* **8**, (2017).

179. Kozawa, D., Kumar, R., Carvalho, A., Kumar Amara, K., Zhao, W., Wang, S., *et al.* Photocarrier relaxation pathway in two-dimensional semiconducting transition metal dichalcogenides. *Nat. Commun.* **5**, 1–7 (2014).

180. Bangert, U., Eberlein, T., Nair, R. R., Jones, R., Gass, M., Bleloch, A. L., *et al.* STEM plasmon spectroscopy of free standing graphene. *Phys. Status Solidi Appl. Mater. Sci.* **205**, 2265–2269 (2008).

181. Kinyanjui, M. K., Kramberger, C., Pichler, T., Meyer, J. C., Wachsmuth, P., Benner, G. & Kaiser, U. Direct probe of linearly dispersing 2D interband plasmons in a free-standing graphene monolayer. *Epl* **97**, (2012).

182. Hill, H. M., Rigosi, A. F., Raja, A., Chernikov, A., Roquelet, C. & Heinz, T. F. Exciton broadening in WS_2/graphene heterostructures. *Phys. Rev. B* **96**, 1–7 (2017).

183. Zhao, S., Dong, B., Wang, H., Wang, H., Zhang, Y., Han, Z. V. & Zhang, H. In-plane anisotropic electronics based on low-symmetry 2D materials: Progress and prospects. *Nanoscale Adv.* **2**, 109–139 (2020).

184. Yan, R., Khalsa, G., Schaefer, B. T., Jarjour, A., Rouvimov, S., Nowack, K. C.,

et al. Thickness dependence of superconductivity in ultrathin NbS$_2$. *Appl. Phys. Express* **12**, (2019).

185. Heil, C., Poncé, S., Lambert, H., Schlipf, M., Margine, E. R. & Giustino, F. Origin of Superconductivity and Latent Charge Density Wave in NbS$_2$. *Phys. Rev. Lett.* **119**, 1–6 (2017).